Charles University in Prague
Faculty of Mathematics and Physics

MASTER'S THESIS

Bc. Lukáš Ondič

Time-resolved measurement of optical gain in silicon based nanostructures

Department of Chemical Physics and Optics

Supervisor: Prof. RNDr. Ivan Pelant, DrSc.
Consultant: RNDr. Kateřina Dohnalová, Ph.D.
Institute of Physics, Academy of Sciences of the Czech Republic

Study programme: Physics, Optics and Optoelectronics

2009

Acknowledgements
First of all I would like to thank to my supervisor prof. RNDr. Ivan Pelant, DrSc. for his perfect guidance and supporting me with his invaluable experiences.

My greatest thanks belong to my consultant RNDr. Kateřina Dohnalová, Ph.D. who helped me a lot with my measurements, supported me with many relevant informations concerning silicon nanocrystals and provided me with great experiences. I would like to thank her for brilliant willingnes to solve every problem either with the experiment or theory.

This work was done at Department of Thin Films at IoP ASCR in Prague, therefore my thanks goes to all staff of the department, who have created a good atmosphere for work.

My special thanks belong to my parents for their support, financial and personal, during whole period of my studies. Last but not least, I would like to express my personal thanks to my partner Bc. Maja Jakabová for her neverending love and help.

This work was supported by the project IAA 101120804 of the Grant agency of the Academy of Science and GAČR grant No.202/07/0818.

I hereby state that I have written this master's thesis by myself using only the cited references. I agree to lend it.

Prague, April 2009 Bc. Lukáš Ondič

Contents

Title: Time-resolved measurement of optical gain in silicon based nanostructures
Author: Bc. Lukáš Ondič
Department: Department of Chemical Physics and Optics
Supervisor: Prof. RNDr. Ivan Pelant, DrSc., Institute of Physics, Academy of Sciences of the Czech Republic
Supervisor's email address: pelant@fzu.cz

Abstract: The aim of this work is to study the optical properties of the material based on oxidized silicon nanocrystals (Si-ncs) embedded at high densities in SiO_2-based matrix. These materials seem to be very promising on the way towards silicon laser. Using our preparation technique - modified electrochemical etching and post-etching in H_2O_2 - we obtain small Si-ncs with the mean core size of 2-3 nm, incorporated at high densities of $\sim 10^{19}$ Si-ncs/cm^3 into an SiO_2-based matrix. In this work, we focused on studying their photoluminiscence (PL) properties and measuring the net optical gain of these samples. Therefore, we investigated their time-resolved and steady-state PL emission spectra which revealed two emission bands - the F-band ($\sim$ 435 nm) with ns decay-time and the S-band ($\sim 600 - 620$ nm) with μs decay-time. Moreover, we observed a "green" emission band ($\sim$ 500 nm) present only during the pulsed excitation and immediately after. We performed time-resolved gain spectroscopy using combination of Variable Stripe Length (VSL) and Shifting Excitation Spot (SES) techniques which allows to study optical gain in materials with relatively low optical gain coefficient such as our samples. We observed stimulation emission (StE) onset for higher excitation densities in different Si-ncs/SiO_2 samples, which denotes the presence of the positive optical gain, from both the F-band and S-band emission components. Finally, we attempted to describe recombination processes in nanosecond and microsecond regimes and a possible origin of optical gain.

Keywords: silicon nanocrystals, optical gain, photoluminiscence

Název práce: Časově rozlišené měření optického zisku křemíkových nanostruktur
Autor: Bc. Lukáš Ondič
Katedra: Katedra chemické fyziky a optiky
Vedoucí diplomové práce: Prof. RNDr. Ivan Pelant, DrSc., Fyzikální ústav AVČR, Praha
e-mail vedoucího: pelant@fzu.cz

Abstrakt: Cílem této diplomové práce je studium optických vlastností materiálu připraveného z křemíkových nanokrystalů (Si-ncs) v SiO_2 matrici. Námi použitá metoda přípravy (elektrochemické leptání a doleptávaní v H_2O_2) umožňuje výrobu Si-ncs se středním průměrem 2-3 nm zabudovaných do matrice SiO_2 ve vysokých koncentracích $\sim 10^{19}$ Si-ncs/cm^3. Zaměřili jsme se na studium jejich fotoluminiscenčních (PL) vlastností a na měření koeficientu optického zisku. Časově rozlíšená PL emisní spektra odhalila existenci dvou emisních komponent - "rychlé" komponenty ($\sim$ 435 nm) s dohasínáním na nanosekundové časové škále a "pomalé" komponenty ($\sim 600 - 620$ nm) s μs časem doznívaní. Navíc jsme pozorovali "zelený" emisní pás ($\sim$ 500 nm), a to jen v krátkém detekčním okně v průbehu pulzní excitace a krátce po ní. Pro časově rozlišené měření optického zisku jsme použili techniku Variable Stripe Length (VSL) v kombinaci s technikou Shifting Excitation Spot (SES), které umožňují studium optického zisku v materiálu s relativně malým koeficientem optického zisku. Naše měření poukazují na vznik stimulované emise pro vyšší excitační intenzity v různých typech vzorků, a to jak z "rychlé" tak i z "pomalé" emisní komponenty. Nakonec jsme navrhli model rekombinačních procesů probíhajících v nanosekundovém a mikrosekundovém režimu, a možný původ optického zisku.

Klíčová slova: křemíkové nanokrystaly, optický zisk, fotoluminiscence

Chapter 1

INTRODUCTION

1.1 Silicon in microelectronics and microphotonics

Silicon is perfect material for electronics. That is mainly due to two reasons, namely, the economical reasons and relatively simple technology of integration. Silicon is the second most abundant element (after oxygen) in the Earth's crust and therefore its cost is relatively low compared to other semiconductors. Silicon has been widely used in electronics after invention of an integrated circuit in 1960s and later it has become an irreplaceable component of microelectronics. A Complementary Metal Oxide Semiconductor (CMOS) is higly developed technology used for the silicon microeletronics integration. Nowadays, it allows to place more than 10^8 components on a single chip that leads to enhanced performance of the integrated chip. The interconnections between the components on the 1 cm^2 single chip recently reached several kilometers in length that causes interconnect propagation delays, overheating and information latency (due to crosstalks) [1] [2]. Moreover the information capacity of the electrical interconnections is limited by the RC constant. These problems are called in summary "interconnection bottleneck". Decreasing the size of the chip and the density of the components will enhance these "interconnection bottleneck" problems.

A solution might lie within the attempt of combining the existing microphotonic and photonic components on a single silicon chip. Silicon microphotonics is the optical equivalent of the microelectronics integrated circuits that utilize silicon-based material for individual components [1]. The idea is simple: to produce an integrated optical chip consisting of optical components such as lasers, modulators, detectors, beam splitters and multiplexers based on silicon whereas light propagating between them is directed through small planar waveguides (optical circuits). However, realization remains an open question mainly due to the absence of the silicon based laser. Therefore, making possible the silicon-based efficient light emitter and laser would lead to a scientific and technological breakthrough in the actual silicon-based photonics.

1.2 Towards silicon laser

First of all, the bulk silicon is a poor source of light due to its indirect band structure character. Its low internal quantum efficiency of $\sim 10^{-6}$ and a fast rate of the non-radiative processes make the possibility of the efficient radiative emission negligible. Therefore, various approaches have been discovered in order to overcome the indirect band-gap limitations of the bulk silicon. We are going to mention some of them.

Observation of photoluminiscence (PL) from porous silicon at room temperature by J. Canham in 1990 [3] inicialized very strong interest in silicon nanostructures as a promissing material for the silicon laser. Out of any doubt, the reason of light emission from silicon lies within the translation symmetry breakage which takes place in the silicon with nanometer dimensions. Later, the PL from the low-dimensional silicon systems at room temperature, covering the whole visible spectrum, has been demonstrated by other research groups; at the same time the wavelength of emitted light shows dependence on both the size of nanocrystals and the surface passivation. Low-dimensional silicon systems that are widely studied in order to find a material suitable for lasing are silicon nanocrystals (Si-ncs) [4], silicon/SiO_2 superlattices, silicon nano-pillars. Moreover, in 2000 Pavesi et al. [4] have reported positive optical gain of ~ 100 cm^{-1} on samples of Si-ncs prepared by Si^+-ion implantation into SiO_2. Also our samples include Si-ncs whereas a special method of embedding Si-ncs into the SiO_2-based matrix is used.

On the other hand, there exist several other promising routes towards silicon laser, such as Erbium doped crystalline silicon [5], Silicon/Germanium quantum cascade structures/superlattices [6] and Silicon intracenter recombinations for THz emission.

The physical mechanism behind the relatively high external quantum effciency in low-dimensional Si is still under debate. It is generally accepted that it is mainly due to quantum confinement of excitons within the nanometer crystalline core. Moreover, the silicon/dielectric interface is also thought to play an active role in both passivation of non-radiative states and formation of radiative states, since the surface/volume ratio significantly increases with spatial confinement.

In conlusion, the silicon-based electrically driven laser diode, where lasing would be achieved via light amplifcation by stimulated emission, has not been successfully built yet and represents one of the challenges of the present research in silicon photonics.

1.3 Aims of this thesis

In this diploma thesis we will focus on studying the possibility of stimulated emission onset in Si-ncs/SiO_2 based materials. The main optical parameter that denotes the stimulated emission onset is a positive net optical gain coefficient. The aim of our preparation method is producing samples with a high optical quality and of a high concentration of Si-ncs embedded in SiO_2-based matrix, leading to enhancement of the StE onset possibility. The net optical gain of prepared samples will be measured by Variable Stripe Length (VSL) and Shifting Excitation Spot (SES) methods under a pulsed nanosecond UV optical excitation. We will also propose a model of involved recombination processes based on our results of the time-resolved measurements of the photoluminiscence.

The diploma thesis is organized as follows. Chapter 2 presents an introductory background of the luminescence in the bulk semiconductors, semiconductor nanocrystals and of the optical gain in semiconductors. First part of chapter 3 covers in detail the preparation technique of our Si-ncs/SiO_2 samples and the second part is devoted to investigation of structural properties of these samples such as the mean core diameter of Si-ncs and surface passivation. Chapter 4 and chapter 5 show our experimental results measured on the Si-ncs/SiO_2 samples. In chapter 4 there are presented the steady-state and time-integrated PL emission spectra. In chapter 5, the VSL and SES methods are described. In the second part of chapter 5, experimental results of the optical gain measurements on our Si-ncs/SiO_2 samples are presented together with the proposed theoretical model of recombination processes. Finally, in chapter 6 we summarize the results and attempt to critically discuss prospects for lasing in an ensemble of Si-ncs embedded in SiO_2 based matrix and present our plans for the future.

Chapter 2

OPTICAL PROPERTIES OF SEMICONDUCTORS

Silicon nanocrystals (Si-ncs) prepared by various methods are being intensively studied for their good optical properties which strongly differ from those of bulk silicon. The use of Si-ncs as an active material for lasing, however, still remain an open question which motivated our work. The most important feature that Si-ncs should exhibit (to be a suitable material for lasing) is the presence of a positive net optical gain coefficient. For the positive net optical gain achievement, stimulated emission (StE) onset and low optical losses are essential. To understand advantages of Si-ncs compared to the bulk silicon, we describe in this chapter the main mechanism of photoluminscence (PL) in both types of semiconductors and we present the main differences in optical properties of the bulk silicon and Si-ncs samples.

2.1 Bulk Semiconductors

Mechanism of PL in bulk semiconductors can be described within the band model of solid state [7]. In this model, electrons and holes are considered to be free quasi-particles whereas the influence of the periodical potential of the crystal is included in their efective masses m_e^* and m_h^*. The highest occupied energy band is called valence band (VB) and the lowest unoccupied conduction band (CB), separated by the energy gap E_g. Scheme of the band diagram of the direct band gap semiconductor is shown in Fig. 2.1(a). Under external excitation by photons with energy $E > E_g$ (nonresonant excitation), electrons in the material can be excited from the valence band to the higher states within the conduction band. Afterwards they quickly relax to lower energy states of the CB, loosing their kinetic energy nonradiatively (due to interaction with the lattice vibrations). Finally, they can recombine either radiatively (emission of photon) after the mean lifetime τ_r or non-radiatively after the mean lifetime τ_{nr}.

The probability of luminescence (radiative recombination) is described by an internal quantum efficiency η_i defined as

$$\eta_i = \frac{1/\tau_r}{1/\tau_r + 1/\tau_{nr}}. \tag{2.1}$$

Material is considered to be an efficient light emitter if the condition $\tau_r \ll \tau_{nr}$ is fulfilled, i.e. if the radiative recombination processes are faster than the nonradiative ones.

Semiconductors can be divided into two main groups according to the position of the VB maxima and the CB minima in k-space. Semiconductors in which the maximum of the VB is located at the same k as the minimum of the CB are called direct band-gap semiconductors (Fig. 2.1(a)). Semiconductors in which the maximum of the VB lies at different k than the minimum of the CB are classified as indirect band-gap semiconductors (Fig. 2.1(b)) (usually the CB minimum is at the edge of Brioulline zone (B.Z.)). Bulk silicon belongs to the group of the indirect band-gap semiconductors.

In optical transitions, momentum and energy conservation rules (among others) must be fulfilled. The radiative recombination of the free electron with the free hole in the direct band-gap semiconductors is a vertical transition, since the resulting photon momentum is negligible. Photon emitted by the radiative transition has an energy

$$h\nu = E_g + \frac{\hbar^2 k_e^2}{2m_e^*} + \frac{\hbar^2 k_h^2}{2m_h^*}\ , \tag{2.2}$$

where $\hbar = h/2\pi$ (h is the Planck constant) and $\hbar\vec{k_e}$ and $\hbar\vec{k_h}$ are the electron and the hole momentum, respectively.

Band-to-band recombination of an e-h pair in indirect semiconductors is accompanied by the emission or absorption of the phonon to fulfill the momentum conservation law. Energy of the emitted photon is

$$h\nu = E_g + \frac{\hbar^2 k_e^2}{2m_e^*} + \frac{\hbar^2 k_h^2}{2m_h^*} \pm \hbar\omega\ , \tag{2.3}$$

where ω stands for a frequency of the phonon. The phonon assisted e-h pair recombination is a simultaneous three particle process of very low probability. Therefore, the non-radiative processes in indirect semiconductors are more probable than the radiative ones ($\tau_r \gg \tau_{nr}$). A more detailed discussion of the non-radiative processes in the bulk silicon will be done in section 2.1.1.

In materials with large E_g in quantum confined structures (such as silicon nanocrystals) or at low temperatures, another important radiative channel appears, which is

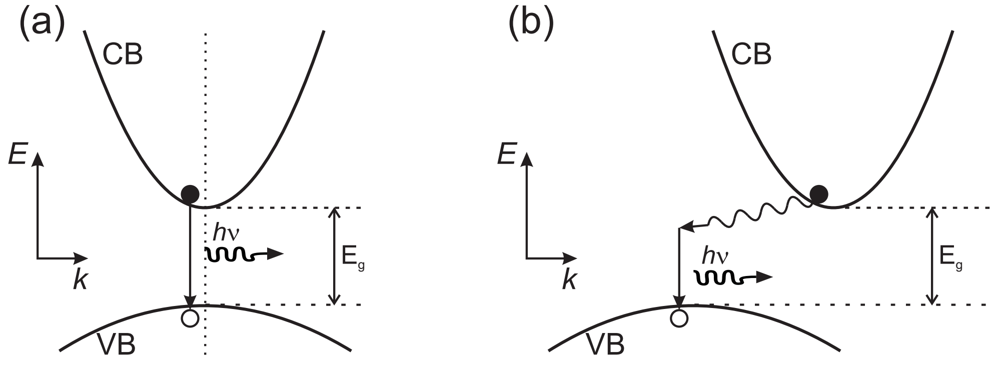

Figure 2.1: *Scheme of the band diagram of the (a) direct band-gap and (b) indirect band-gap semiconductor. VB and CB stands for valence and conduction energy band separated by the energy gap E_g.*

the excitonic recombination. Exciton is a quasi-particle which consists of an electron and hole interacting via attractive Coulomb electrostatic interaction [8]. Several types of excitons are known, however in most semiconductors we have the Wannier type of excitons. Wannier's exciton can be characterized by its large radius (distance between the electron and the hole) which is typically of length equal to several lattice constants. It is a neutral particle that carries energy but not electric charge and behaves as a free particle, if not trapped on defects or impurities. Solving the quantum mechanical problem of the exciton is relatively simple if we use results for a Bohr's model of hydrogen atom, however, two important differences have to be considered. Firstly, contrary to hydrogen, the effective masses of the electron and hole in the semiconductor are comparable and very light. Secondly, electrostatic force between the electron and hole is lowered by the dielectric constant ε of the semiconductor lattice. Both features make exciton less stable, compared to hydrogen atom. The exciton radius r_n can be written as

$$r_n = \frac{\varepsilon}{m_r/m_0} n^2 a_B \ , \tag{2.4}$$

where m_r is reduced mass of the exciton defined by $\frac{1}{m_r} = \frac{1}{m_e^*} + \frac{1}{m_h^*}$; $n = 1, 2, 3, ...$ stands for the main quantum number and $a_B \approx 5.10^{-2}$ nm is the Bohr radius of hydrogen atom. The typical values for the semiconductors are $\varepsilon \approx 10$, $m_r/m_0 \approx 0.1$, i.e. the Wannier's exciton radius r_x is of the order of nanometers ($r_x \equiv r_1 \approx 4.9$ nm in bulk silicon).

In a similar way, binding energy for different exciton quantum states can be evaluated

$$E_n^X = \frac{m_r/m_0}{\varepsilon^2} \frac{E_H}{n^2} \ , \tag{2.5}$$

where $E_H = -13.6$ eV is the binding energy of the electron in hydrogen atom. Excitons in most of the bulk semiconductors are stable at low temperatures only because of their low binding energy (typically of the order of 10 meV). At higher temperatures, on the other hand, the energy of phonons is sufficient to dissociate the exciton to the free electron and free hole.

Overall energy of the free exciton with the momentum $\hbar\vec{K}$ moving through the direct band-gap semiconductor can be written for the ground state ($n = 1$) as

$$E_1 = E_g - E_1^X + \frac{\hbar^2 K^2}{2m_{exc}} \, , \tag{2.6}$$

where $m_{exc} = m_e^* + m_h^*$ is total exciton mass. In the case of an indirect semiconductor, the energy of the phonon $\pm\hbar\omega$ has to be added to the right side of Eq. 2.6. The presence of the excitons in a direct band-gap semiconductor is manifested by the exciton lines in the absorption spectrum at energies $E_g - E_n^X$ below the absorption edge. The luminescence of free excitons, on the other hand, is a more complicated process. In both, direct and indirect band-gap materials, radiative recombination is accompanied by phonon emission, and in direct band-gap semiconductors also polariton effects must be taken into account. The bound-excitonic luminiscence is more probable especially in indirect semiconductors. The special case of bulk and nanocrystalline silicon will be discussed in the following.

2.1.1 Optical properties of bulk crystalline silicon

Silicon is an indirect band-gap semiconductor with the maximum of the valence band in the middle of the Brillouin zone (Γ point) and with the minimum of the conduction band close to the point X along the $\langle 001 \rangle$ direction [7]. The band-gap energy is approximately 1.12 eV at room temperature.

Radiative recombination of the electron-hole pair is a phonon assisted transition and the typical decay time of this process is of the order of miliseconds ($\tau_r \sim$ ms) [9]. The non-radiative processes, on the other hand, play an important role in the optical transitions of the silicon and take place usually in a shorter time period (typically $\sim$ns) after excitation. The internal quantum efficiency of the silicon, according to Eq. 2.1, is of the order of 10^{-6} and therefore the luminiscence from the bulk silicon is very weak. We will list the most important non-radiative processes occuring in bulk silicon.

Electron can be captured on the *defects and surface states* of the lattice and then non-radiatively recombine to the ground state. It depends on the sample quality which can be controlled by the preparation technology and by the surface passivation.

Shockley-Read-Hall recombination can occur in semiconductors with deep localized states in the forbidden energy gap, originating from impurities or defects. The characteristic time of this process is of the order of microseconds.

Auger recombination occurs by a transfer of energy and momentum released by the recombination of the electron-hole pair to a third particle. The third particle can be either the free electron in the CB (eeh process) or another free hole in the VB (ehh process). The e^- and h^+ concentration rate equation under Auger mechanism for an intrinsic semiconductor ($n = p$, where n and p is the electron and hole concentration respectively) can be expressed as

$$\frac{\mathrm{d}n}{\mathrm{d}t} = G - C_A n^3 \,, \tag{2.7}$$

where G is the rate of electron-hole pair generation and C_A is an Auger constant. According to Eq. 2.7, the probability of the Auger recombination is dependent on the third power of the free carrier concentration. Therefore it will be a dominant process in higly excited or dopped semiconductors. The decay time of the Auger recombination τ_A can be defined as

$$\frac{1}{\tau_A} = C_A n^2 \,, \tag{2.8}$$

(in bulk silicon being of the order of hundreds of ps up to several ns). The Auger recombination is influencing adversely the probability of stimulated emission (StE) onset because is depletes the population inversion at high pumping densities.

Another important process, which can lead to the depopulation of the excited states in bulk silicon and prevent the StE onset, is *Free Carrier Absorption (FCA)*, when the photons penetrating into the material can be absorbed by excited electrons in CB, increasing their kinetic energy. Thus the population inversion build-up process is damped by increased optical losses α_{tot}. Also the photon created by the electron-hole radiative recombination inside the material can be reabsorbed by the free carriers resulting in lowering the PL signal output intensity. According to the Drude model, the FCA coefficient depends linearly on the concentration of free carriers and quadratically on the wavelength of absorbed light as $\alpha_{FCA}(\lambda, n) \propto 10^{-18} n \lambda^2$. It has approximately the same order of magnitude in both the direct and indirect band-gap materials.

The coefficient of the overall optical losses is given by $\alpha_{tot}(\lambda) = \alpha_{FCA}(\lambda) + \alpha(\lambda) + K(\lambda)$, where $\alpha(\lambda)$ stands for the band-to-band absorption coefficient defined by the Fermi golden rule and $K(\lambda)$ are the losses caused by the light scattering.

Under relatively low external pumping fluency, the overall optical losses are of the positive value, therefore the light intensity $I(x, \lambda)$ at the wavelength λ is lowered while passing the infinetisimal distance $\mathrm{d}x$ in the material:

$$\alpha_{tot}(\lambda) = \frac{\mathrm{d}I(x,\lambda)}{\mathrm{d}x} \frac{1}{I(x,\lambda)} \,. \tag{2.9}$$

Integrating the previous equation along the optical path d we obtain the Beer-Lambert law

$$I(d, \lambda) = I(0, \lambda) e^{-\alpha_{tot}(\lambda) d} \ . \tag{2.10}$$

Intensity of the light passing through the material in a ground state ($\alpha_{tot} > 0$) is exponentialy decreasing. On the other, if the population inversion is achieved between two energy states (under external pumping), then the StE onset can appear in the material and α becomes negative. Optical gain coefficient is defined in such a case by

$$g(\lambda) = -\alpha(\lambda) \ . \tag{2.11}$$

If a condition $|\alpha_{FCA}(\lambda) + K(\lambda)| < |\alpha(\lambda)| \wedge \alpha(\lambda) < 0$ is fulfilled, than overall optical losses in the material switch to negative values ($\alpha_{tot} < 0$) and light will be amplified while passing through the material. The net gain coefficient is defined as follows

$$G(\lambda) = -\alpha_{tot}(\lambda) \ . \tag{2.12}$$

A necessary (but not sufficient) condition for lasing is therefore the presence of the positive net optical gain in the material. To achieve the positive net optical gain (the StE onset), high pumping and low optical losses are required. StE onset is possible only if the threshold population inversion was established between two energy levels. Thus non-radiative processes that are depleting the population inversion must have longer mean lifetime than is the time needed for StE onset. Semiconductor nanocrystals seems to be very promising material to achieve such optical properties.

2.2 Semiconductor nanocrystals

By decreasing the size of bulk semiconductor we obtain the semiconductor nanocrystal with dimensions in nanometer scale. Nanocrystals have different optical properties from the bulk semiconductors due to the quantum confinement effect, based on the spatial localization of the carriers within the nanocrystal. We can separate the quantum confinement according to the relation between a diameter of the spherical nanocrystal R_x and a free exciton Bohr radius r_x into a strong and weak confinement regime.

In the weak confinement regime is $R_x \gg r_x$ and the electrostatic force between the electron and the hole is significant. The problem can be reduced to solving the Schrödinger equation for an exciton confined in a spherical potential barrier.

In the strong confinement regime is $R_x \ll r_x$ and the electrostatic electron-hole interaction can be neglected, compared to their kinetic energy. The electron and hole can be considered as independent particles with the effective masses and the basic model of such a behaviour is the model of a particle in a quantum dot (QD).

Model of a quantum dot

Kinetic energy of the electron or hole with the effective masses m_e^* or m_h^* in the state nl in a quantum dot is [10]

$$E_{nl} = \frac{2\hbar^2\chi_{nl}^2}{m_{e,h}^* R_x^2} \ , \tag{2.13}$$

where χ_{nl} is the n-th root of the spherical Bessel function of the l-th order. Its value for the lowest energy level ($n = 1, \ l = 0$) is $\chi_{10} = \pi$. If the quantum dot is prepared from the semiconductor with the forbidden energy gap of width E_g, the lowest energy of the optical transition (energy of the forbidden gap of the QD) is

$$E_g^{nc}(R_x) = E_g + \frac{2\hbar^2\pi^2}{R_x^2}\Big(\frac{1}{m_e^*} + \frac{1}{m_h^*}\Big) \ . \tag{2.14}$$

The energy spectrum of the QD resembles atom-like discrete energy spectrum. Furthermore, the energy gap gets larger with decreasing size of the nanocrystal (Eq. 2.14) and therefore the wavelength of the emitted light from nanocrystal can be tuned with its size. Scheme of the quantum dot for two different sizes of nanocrystal is sketched in Fig. 2.2.

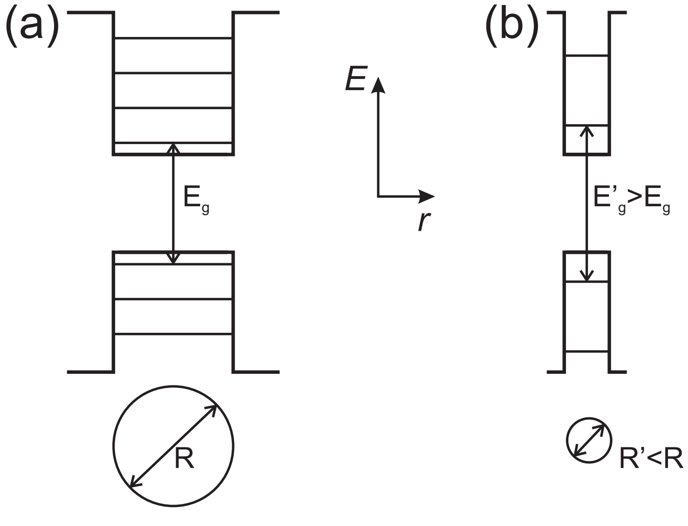

Figure 2.2: *Scheme of the quantum dot model.*

.

2.2.1 Silicon nanocrystals (Si-ncs)

Electronic spectrum of the Si-ncs consists of well separated atom-like energy states whose separation rises with decreasing QD size. Furthermore, according to the Eq. 2.14, as the size of a QD decreases, the band gap of the Si-ncs increases due to the quantum confinement effect. Spectral blue-shift in luminescence is the result of this effect (see Fig. 2.3(a)). The emission spectra in Fig. 2.3(a) are inhomogeneously broadened because they are measured from an ensemble of Si-ncs with broader size distribution. Fig. 2.3(b) shows the dependence of the band gap energy as a function of the Si-ncs size R_{Si-ncs} that can be fitted with a curve given by equation $E_g = 1.16 + 11.8/R^2_{Si-ncs}$ [11].

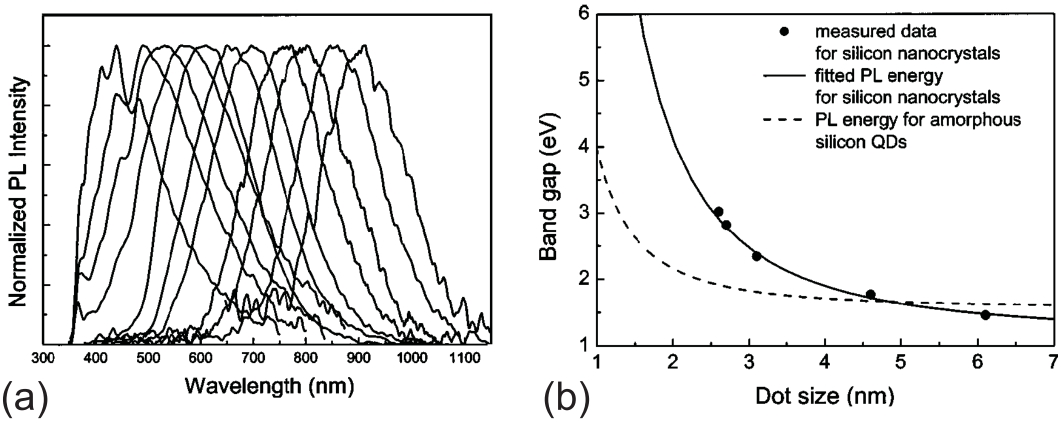

Figure 2.3: *(a) Tuneability of the emission wavelength by varying the Si-ncs average size in the non-oxidized Si-ncs ensemble. (b) The confined band gap energy as a function of the Si-ncs size. Both taken from [11].*

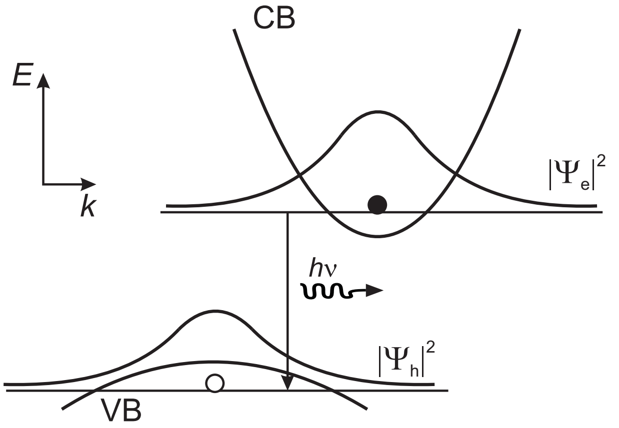

Figure 2.4: *Quantum confinement effect in a semiconductor with indirect band-gap. Quasi-direct transitions are possible.*

Let us now discuss several mechanisms that increase the probability of radiative recombination and intensity of photoluminiscence of Si-ncs, compared to bulk silicon.

The band-to-band absorption/gain coefficient at wavelength ω in a low-dimensional semiconductor structure can be derived from the Fermi golden rule as

$$\alpha(\omega) \sim f_{cv}(\omega) J_{cv}(\omega) \ , \tag{2.15}$$

where $J_{cv}(\omega)$ is the joint density of states and $f_{cv}(\omega)$ stands for the oscillator strength defined as

$$f_{cv} \sim |\langle \Psi_{c,\vec{k}} | \vec{a} \vec{p_{cv}}(\vec{k}) | \Psi_{v,\vec{k}} \rangle|^2 \ , \tag{2.16}$$

where $\Psi_{c,\vec{k}}$ and $\Psi_{v,\vec{k}}$ stand for the electron and hole wavefunctions, respectively, and $\vec{a}\vec{p_{cv}}$ is the electrical dipole moment projection onto the photon polarization direction. According to this, Si-ncs with smaller diameter will have higher ocillator strength in comparison to bigger ones due to higher overlap of confined electron and hole wavefunction. Therefore the probability of the radiative recombination is higher in smaller nanocrystals leading to shorter radiative decay time in smaller Si-ncs.

Furthermore, from Heisenberg's relation of uncertainty

$$\Delta p \Delta r \geqq \hbar/2 \tag{2.17}$$

it follows that the strong confinement of the electron and hole wave function in real space leads to a delocalization of the wave functions in the k-space (Fig. 2.4). Thus the overlap of the wave functions of the electron and the hole in a nanocrystal (made of an indirect band-gap semiconductor) is not negligible and quasi-direct (no-phonon assisted) transitions can proceed. This effect significantly increases the efficiency of luminescence of indirect band-gap nanocrystals, such as the Si-ncs.

2.2.1.1 Surface states in oxidized Si-ncs

It is well known that surface passivation of nanocrystals plays an important role in the luminiscence because of the increased ratio of their surface to volume. According to the type of passivation, the surface states can be diverse. In non-oxidized Si-ncs passivated with hydrogen the emission mainly originates from the core-related excitonic recombination, since no surface states are formed within the band gap [12]. The spectral blue-shift of the PL was observed with decreasing the nanocrystal size in agreement with the predictions of quantum confinement effect.

On the other hand, in samples exposed to air (oxidized Si-ncs) the spectral red-shift of the PL (compared to that in hydrogenated Si-ncs) was observed that is related to the trapping of an electron (or both - electron and hole) by SiO double bonds (Si=O) that produce localized levels within the band-gap of nanocrystals smaller than approximately 3 nm (Fig. 2.5). These excitons are often interpreted as Self-Trapped Excitons (STE), where the trapped electron state is a p-state localized on the Si atom of the SiO double bond and the trapped hole state is a p-state localized on the oxygen atom. Therefore trapping of the e-h pair leads to a spatial separation of the carriers that, firstly, increases the time of the radiative recombination and secondly, possibly decreases the probability of the Auger process [13]. A band digram of the electronic states in oxidized Si-ncs as a function of the cluster size is shown in Fig. 2.5. According to this figure, the dominant recombination processes depend on the nanocrystal size as follows: above approximately 3 nm we have free exciton annihilation, for sizes between approximately 1.5 nm and 3 nm we have radiative recombination involving free holes and electrons localized on the SiO bonds and for sizes below approximately 1.5 nm we have radiative recombination of electrons and holes, both localized on SiO bonds (trapped excitons).

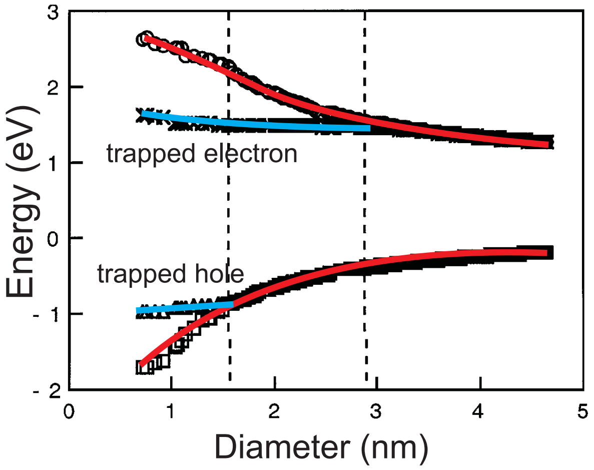

Figure 2.5: *Electronic states in Si-ncs as a function of the cluster size and surface passivation. The red-lines represent the increasing gap energy. The blue-lines are related to the trapped electron state (p-state localized on the Si atom of the SiO double bond) and the trapped hole state (p-state localized on the oxygen atom). As taken from [12].*

SiO (Si-O-Si) normal bonds and SiOH (Si-O-H) bonds can be also formed on the surface of Si-ncs. Si-Si or Si-O-Si bonds on the surface are likely to weaken or break in many places because of the large stress at the Si-ncs/SiO_2 interface [14]. Another important effect of surface passivation is the elimination of dangling bonds (acting as a non-radiative channel of recombination) which results into a more efficient luminiscence. Since the SiO double bond does not lead to large surface deformation, it is more likely to be formed and stabilize the interface [15].

We can conlude that in the oxygen passivated Si-ncs, the main recombination processes, beside the core-exciton recombination, are due to the surface/interface oxygen-related states. Moreover, a four-level system involving surface states was developed [16] that enhances the possibility of the StE onset under low pumping densities in the oxidized Si-ncs. An interesting conclusion concerning the oxygen-related states has been published also by Chen et al in [17], namely, the StE onset in Si-ncs system might be an extrinsic property of the Si-ncs connected rather to the oxygen-related states than to the intrinsic core-exciton recombination, which in other words means that the Si-ncs perhaps must be oxidized in order to observe StE onset.

There exist various different methods of the surface passivation leading to different confinement potentials and the Si-ncs interdot energy barrier. Another effect that may occur due to the low Si-ncs surface potential is a "hopping effect". It is a diffusion of excitons (confined carriers) from one nanocrystal to another that causes an increase of the times of the radiative and non-radiative recombination [18] and might be one of the origins of the stretched exponential behaviour of the S-band luminiscence decay.

2.2.1.2 Non-radiative processes in Si-ncs

A very efficient non-radiative channel for electron-hole recombination in the Si-ncs is the Auger effect. One would expect that the Auger effect efficiency should be even higher in the Si-ncs (in comparison to the efficiency in the bulk silicon) due to the spatial localization of the carriers. On the other hand, the atomic-like structure of energy levels in the Si-ncs should hinder the Auger processes because of the reduced availability of the final states satisfying energy conservation rule [19]. As a result, Auger recombination can occur efficiently only with the participation of a phonon (as a four-particle process) or with the involvement of the final state from the continuum of states outside the QD (Auger ionization). The decay time of the Auger mechanism in the small Si-ncs was established by Delerue et al. to be $\tau_A \sim 1$ ns [20].

The bulk semiconductor approach can be used for a simple model of the Auger effect in the Si-ncs. Within this model [19], the decay time of the Auger recombination is dependent on the size of the nanocrystal as $\tau_A \sim R^3_{Si-ncs}$. It means that the smaller the nanocrystal, the higher the probability of the Auger recombination will be. However, the difference from the bulk silicon approach is that in the regime of a few e-h pairs per dot (N) the recombination occurs as a sequence of quantized steps from the N to N-1,N-2,... and finally to the 1 e-h pair state, every step of the recombination being characterized by a different decay time constant τ_N. It holds that $\tau_N < \tau_{N-1}$ and N depends on the pumping intensity. Another difference from bulk is that the Auger mechanism acts as soon as two e-h pairs are excited inside the nanocrystal [19][21]. If the excitation intensity is higher than one e-h pair per Si-nc (multiple excitation), all excess pairs will be lost in fast Auger recombination, and virtually only the last remaining pair will contribute to the radiative recombination. Therefore we can conclude that from a certain value of the pumping intensity, increasing the pumping will not enhance the core-related emission from the Si-ncs but it will lead to its saturation.

However, in the oxidized Si-ncs system, in which the emission is due to the surface/interface related self-trapped excitonic recombination, the situation is different. In self-trapped excitons (both the electron and the hole are trapped on the Si-ncs/SiO$_2$ interface) the wave-functions of charge carriers are localized on a single covalent bond and the carriers cannot interact efficiently with a third one, in order to recombine through the Auger process [13]. Therefore the probability of the Auger mechanism is probably low even at higher excitation densities.

The second important non-radiative channel of recombination in the Si-ncs is the Free Carrier Absorption (FCA) in confined systems called also the Confined Carriers Absorption (CCA). The FCA absorption coeffiecient depends quadratically on the wavelength as $\alpha_{FCA}{\sim}\lambda^2$ and therefore, in order to reduce optical losses, samples prepared from smaller nanocrystals with spectrally blue-shifted emission are preferred in comparison to the bigger ones. Lower probability of the FCA process leads to the higher probability of the StE onset in such samples because the emitted photon is not reabsorbed by the free carriers. Thus, the most important requirements imposed on the prepared samples will be based on this knowledge.

The carriers trapping on deep Si-ncs surface states due to presence of the "dangling bonds" belong between less important non-radiative processes in oxidized Si-ncs [22]. Dangling bonds correspond to coordination defects in which the silicon atom has only three equivalent covalent bonds. The capture by neutral dangling bonds is much faster than the radiative recombination, particularly at room temperature. Therefore, a high-quality surface passivation is required in order to eliminate competing nonradiative carrier relaxation pathways.

2.2.1.3 Necessary condition for stimulated emission in oxidized Si-ncs

As we have already mentioned, StE onset in the sample will cause an increase of the light intensity passing through the sample and it becomes possible to observe the positive optical gain i.e. the positive optical gain can be measured in the sample. If we consider that all recombination processes take place in the sample after pulsed excitation, a necessary condition for the StE onset based on the dynamics of these processes can be written as follows

$$\tau_{FCA}, \tau_A, \tau_{surf} > \tau_{StE} \Rightarrow \text{stimulated emission} \ , \tag{2.18}$$

This condition says that the StE build-up time τ_{StE} has to be shorter than the characteristic times of all possible non-radiative processes such as Auger recombination (τ_A), FCA losses (τ_{FCA}) and the surface trapping rate into the deep-trap states as dangling bonds (τ_{surf}).

A four-level system has been introduced [23] to model quantitatively the recombination dynamics under gain conditions. According to this model, it is possible to define StE lifetime as

$$\tau_{StE} = \frac{4}{3}\pi\Big(\frac{R_{Si-ncs}}{2}\Big)^3 \frac{1}{\xi\sigma c n_{ph}} \ , \tag{2.19}$$

where R_{Si-ncs} is the Si-ncs diameter, ξ is the Si-ncs volume fraction (the ratio of the Si-ncs to SiO_2 volume), σ is the gain cross-section, n_{ph} is the number of emitted photons and c is the light velocity. According to Eq. 2.19, the probability of the StE onset can be controlled via the size and concentration of nanocrystals and via the pumping density (n_{ph}).

The Auger decay time depends on R_{Si-ncs} and the free carrier concentration n_{FC} (depends on the pumping density) as [23]

$$\tau_A \sim \frac{R^3_{Si-ncs}}{n_{FC}} \; . \tag{2.20}$$

Comparison of Eq. 2.19 and Eq. 2.20 poses a condition on the volume fraction ξ because the dependence on the R_{Si-ncs} is similar in both equations. Moreover, the decrease of τ_A with shrinking R_{Si-ncs} ought to be slower compared to corresponding decrease of τ_{StE} owing to shorter exciton lifetime in smaller Si-ncs. Therefore it follows that samples containing high concentration of small nanocrystals are desirable. On the other hand, based on empirical models [24] and our measurements, dependence of the emission intensity on the Si-ncs concentration is not linear but it shows a maximum for certain concentrations (in our samples at $\sim 10 - 20$ vol.% (Fig. 3.2 in chapter 3)) and it saturates or decreases for higher concentrations (high concentration of Si-ncs allows probably a strong reabsorption of emission by other nanocrystals).

Let us now conclude about the requirements imposed on our samples. The FCA was discussed in the section 2.2.1.2 and the result of the discussion was that small nanocrystals with blue-shifted emission are suitable for the sample preparation. Trapping of electrons into the deep surface states is, due to a good surface passivation, less probable than other non-radiative processes and therefore it can be neglected. Finally, we can propose three conditions imposed on our samples in order to achieve the optical gain.

Those are

- the small size of nanocrystals
- the high concentration of Si-ncs in SiO_2 matrix
- the spectrally blue-shifted emission.

Chapter 3

PREPARATION AND CHARACTERIZATION OF Si-ncs/SiO$_2$ SAMPLES

3.1 Si-ncs/SiO$_2$ sample preparation technique

A method used for fabrication of Si-ncs/SiO$_2$ samples is based on the technique introduced by V. Švrček et al. in [25]. It presents a low cost way of incorporating Si-ncs made by electrochemical etching of monocrystalline p-type Si wafers into a sol-gel derived SiO$_2$-based matrix. Commonly used methods such as Si$^+$-ion implantation or Plasma Enhanced Chemical Vapor Deposition produce samples with relatively low density and/or a large Si-ncs mean core diameter in SiO$_2$ layers compared to our samples. These samples, compared to the direct band-gap active semiconductor-materials such as GaAs, show relatively low optical gain (e.g. one of the highest net modal optical gain was published in [4]). Gain values are sample dependent and affected by gain-like artifacts due to limited possibilities of optical gain measurement technique (the Variable Stripe Length technique). It appears necessary to attempt to meet the theoretical requirements imposed on the Si-ncs/SiO$_2$ samples in order to achieve reproducable optical gain results.

Our method leads to samples that contain small oxidized silicon nanocrystals with mean core diameter of 2-3 nm integrated at high densities (up to 20 vol.%) in an SiO$_2$-based matrix. The volume fraction of Si-ncs in an SiO$_2$-based matrix has to be chosen carefully as a compromise between high emission yield and high optical quality required, for the optical gain measurements. The size of Si-ncs depends on etching parameters and should be of small values as required for optical gain achievement. In the end, we obtain sol-gel SiO$_2$ layers "doped" with Si-ncs which meet the necessary theoretical presumptions for the positive optical gain. We will now discuss in detail the preparation technique of three different types of our Si-ncs/SiO$_2$ samples. The preparation technique is also well described in [26].

3.1.1 Preparation of Si-ncs by electrochemical etching

Silicon nanocrystals were prepared by a method of electrochemical etching of a boron doped (p-type) silicon wafers. The experimental setup is sketched in Fig. 3.1(a).

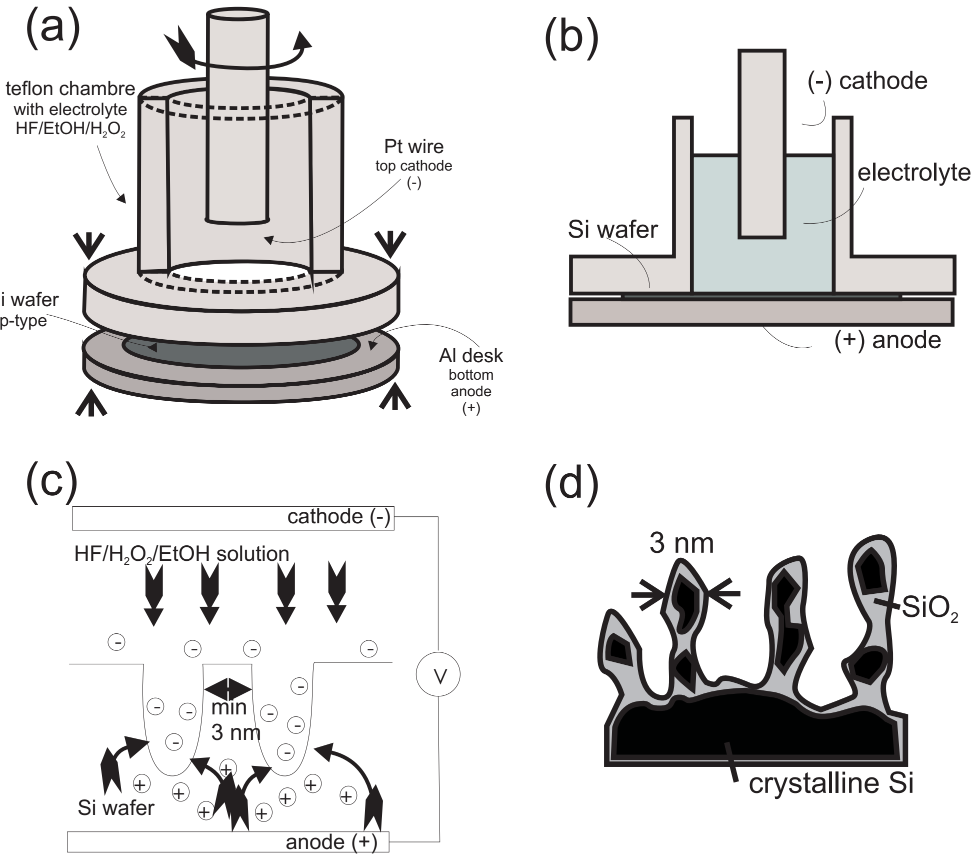

Figure 3.1: *(a)(b) Sketch of the electrochemical etching setup, (c) the etching reaction principle and (d) a sketch of the resulting pore structure of a porous silicon layer.*

We put the wafer on the bottom of a teflon chamber filled with an acidic etching bath. The silicon wafer is connected to the positive anode made from aluminium and on the opposite side the negative Platinum (Pt) cathode is placed. The standard etching solution is prepared from 50% hydro-fluorid acid HF mixed with pure ethanol EtOH (99.96%). After applying an electrical field to the electrodes, the dissolution reaction of the Si wafer by HF acid starts to proceed according to the scheme

$$\begin{aligned} \mathrm{Si} + 2\mathrm{HF} + \mathrm{xh}^+ &\rightarrow \mathrm{SiF}_2 + 2\mathrm{H}^+ + (2-\mathrm{x})\mathrm{e}^- \\ \mathrm{SiF}_2 + 2\mathrm{HF} &\rightarrow \mathrm{SiF}_4 + \mathrm{H}_2 \\ \mathrm{SiF}_4 + 2\mathrm{HF} &\rightarrow \mathrm{H}_2\mathrm{SiF}_6 \end{aligned} \tag{3.1}$$

where e^- and h^+ stand for free electrons and holes, respectively.

Using low current densities (<10 mA/cm^{-2}), the Si wafer surface acquires a porous structure as shown in Fig. 3.1(d). Among these pores, pillars with a mean size of several nanometers containing Si-ncs are created. In order to obtain a homogeneous distribution of pores/pillars over the whole surface, a homogeneous electrical field within the etching chamber should be ensured. This is possible by covering the entire area of the etched wafer with both electrodes. However, the top electrode must be perforated to allow leaking of the H_2 bubbles from the wafer surface (Eq. 3.1). Another approach to get a homogeneous etching consists in fixing a Pt stripe on the rim of the teflon chamber and assuring a continuous stirring of the etch bath.

The porosity of the surface (defined as a ratio of porous volume to the total volume) characterizes the size of Si pillars and therefore the size of the Si-ncs. The diameter of Si pillars is limited from below by ~ 3 nm due to inhibited hole diffusion into the fine pillars (Eq. 3.1). Our purpose was to lower the size limit of the Si-ncs which can be achieved either by adding H_2O_2 (hydrogen peroxide) to the standard etching solution and/or by performing an additional post-etching process in H_2O_2 solution. H_2O_2 works as a catalyzer of the reaction and leads to a production of smaller Si-ncs with surface passivated by -OH groups (contrary to the samples prepared without the H_2O_2, passivated dominantly by the double oxide bonds). The oxidative effect of H_2O_2 is given by the following scheme

$$\begin{aligned} \mathrm{Si} + 2\mathrm{H}_2\mathrm{O}_2 &\rightarrow \mathrm{Si(OH)}_4 \\ 2\mathrm{Si(OH)}_4 &\leftrightarrow \mathrm{Si(OH)}_3\text{-O-}\mathrm{Si(OH)}_3 + \mathrm{H}_2\mathrm{O} \end{aligned} \tag{3.2}$$

where the second equation direction and velocity is driven by the water amount involved in the reaction.

It was not a goal of this thesis to study different conditions in order to improve the optical quality of prepared samples. Therefore, the parameters used during the preparation process were based on knowledge of my collegues that can be found in [26]. In the following, we will recapitulate the used etching parameters in detail.

Etching parameters

Si-ncs layer was prepared from Boron dopped p-type silicon wafers (crystalline orientation ⟨100⟩ and the resistivity of 0.1 Ωcm). As an electrolyte we used the HF acid

(50% in H_2O) diluted in pure EtOH (99.96%) and H_2O_2 of different concentrations. Using this technique we prepared three various types of Si-ncs layer (their names are based on the appearance of the Si-ncs layer under daylight):

- A ”standard” Si-ncs sample was etched in a solution consisting of HF : EtOH $= 1 : 2.5$ (no H_2O_2) at a constant etching current density of 1.6 mA/cm^2 for ~ 2 hours.
- A ”yellow” type of Si-ncs layer was etched in a solution composed of HF : EtOH : H_2O_2 (3% in water) $= 1 : 2.46 : 0.54$ at a constant current density of 2.3 mA/cm^2 for ~ 2 hours. Moreover, the freshly prepared Si-ncs layer underwent a post-etching procedure during which the Si-ncs layer was dipped in H_2O_2 (3%) for 5 minutes.
- A ”white” type of Si-ncs layer was electrochemically prepared by etching in the solution of HF : EtOH : H_2O_2 (30% in water) $= 1 : 2.85 : 0.15$ at 2.3 mA/cm^2 for ~ 2 hours. Immediately after, the Si-ncs layer was post-etched in H_2O_2 (30%) for 15 min. The post-etched layer had to age for a few days in stable ambient conditions in order to develop bright photoluminiscence (PL).

The PL of various Si-ncs layers under UV lamp illumination is shown in Fig. 3.3(a). In this thesis we focus our attention on samples prepared from ”yellow” and ”white” Si-ncs layers. Their fabrication will be discussed now.

3.1.2 Preparation of Si-ncs/SiO$_2$ samples

The Si-ncs layer is scraped off the Si-wafer substrate into an Si-ncs powder. This powder consists of relatively large clusters of mean size of ~ 1 μm of agglomerated Si-ncs that can be partially separated using ~ 1 hour ultrasonic treatment in pure EtOH. Thereafter, the fine Si-ncs powder is dried and its PL under UV lamp irradiation is shown in Fig. 3.3(b).

Finally, the dried Si-ncs powder is embedded into an SiO_2 sol-gel matrix using the following procedure. The weighted amount of the powder (~ 2 mg) is mixed with a Phosphorus doped SiO_2-based sol-gel which is commercialy available as P509 Spin-On-Difusant (SOD P509 made by Filmtronics Inc. corporation). The advantage of the presence of Phosphorus in the solution is twofold: (i) PL peak of the Si-ncs within such matrix spectrally blue-shifts [27] and (ii) the emission yield increases due to the passivation of the non-radiative centers such as dangling bonds on the Si-ncs surface [28]. We have also found out that the presence of Phosphorus considerably facilitates the formation of good optical quality self-supporting, transparent samples.

Then the liquid mixture of Si-ncs and SOD P509 is poured into a spectroscopic quartz cuvette (3.5 cm(height) x 1.0 cm x 1.0 cm) with polished faces and bottom, and undergoes a further ultrasonic treatment for $\sim 30 - 60$ minutes to avoid larger agglomeration of the Si-ncs. The solution starts to solidify after $\sim$ 60 minutes in air and therefore longer ultrasonic treatment might cause a damage to the forming solid state matrix (cracks). The Si-ncs powder slowly sediment by itself at the bottom of the cuvette where it forms the Si-ncs rich layer. To further increase the density of Si-ncs within the layer, we apply an additional centrifuge treatment for few minutes at 3000 revs per minute. As the last step, the samples are left to solidify for few days in air under ambient conditions. Finally, we obtain a layer of densely packed Si-ncs embedded in the SiO$_2$-based matrix close to the cuvette bottom (Fig. 3.3(c)).

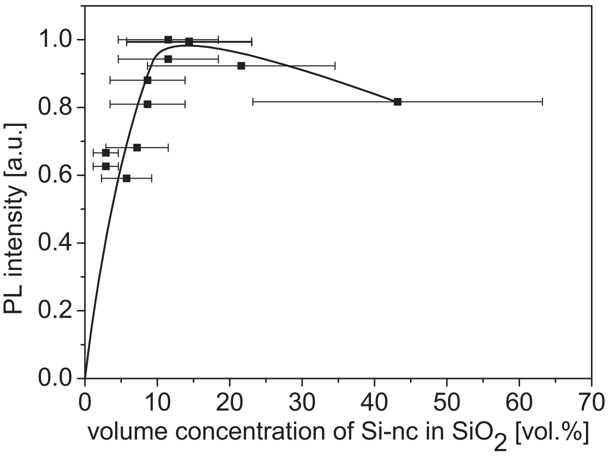

Figure 3.2: *The dependence of the sample PL intensity on the Si-ncs volume concentration in the SiO$_2$ matrix. Taken from [26].*

According to [26], if we define the volume fraction of Si-ncs in the SiO$_2$ matrix as a ratio of the total Si-ncs volume and the Si-ncs rich layer volume, volume fraction of Si-ncs/SiO$_2$ sample with the highest PL intensity would be 10-20 vol.% (Fig. 3.2). Further increasing of the Si-ncs volume fraction leads to the Si-ncs aggregation, lowering the sample homogenity and therefore the optical quality. Therefore most of our samples were prepared with regards to this knowledge. We mixed $\sim$ 2 mg of Si-ncs with $\sim$ 0.4 ml of SOD P509 and the thickness of the final Si-ncs-rich layer after complete solidification was about $\sim 50\ \mu$m, as measured by the micro-photoluminescence spectroscopy (Fig. 3.3(d)). Due to the fluctuations in the Si-ncs rich layer thickness, it does not exhibit any waveguiding effects.

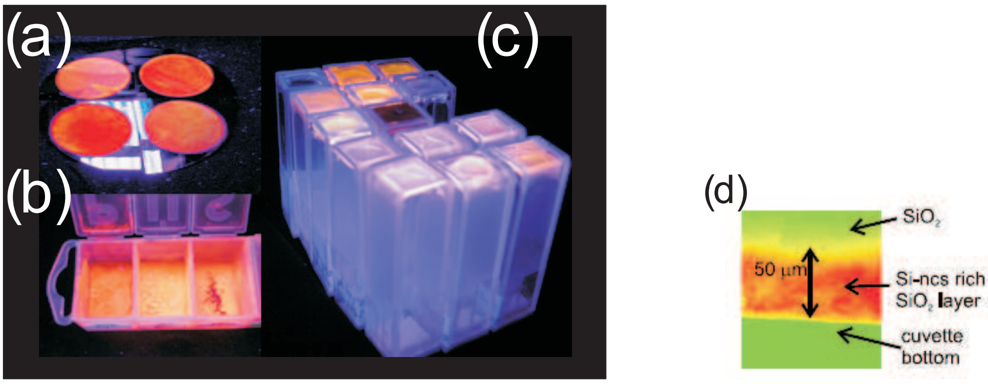

Figure 3.3: *(a) Si-ncs layer on silicon wafer, (b) dried Si-ncs powder and (c) final Si-ncs/SiO$_2$ samples in quartz cuvettes under UV illumination. (d) Micro-PL image of the Si-ncs layer on the bottom of the cuvette. Taken from [26].*

3.2 Si-ncs/SiO$_2$ samples characterization

Let us now present basic structural properties of our samples, as measured with several methods. Influence of the H_2O_2 in the etching process was examined using the Fourier Transform Infrared spectroscopy (FTIR). Fig. 3.4 shows the comparison of FTIR absorption spectra of the "standard" and "yellow" Si-ncs powders. For both types, peaks at 792, 1050 and 1160 cm^{-1} are visible, related to the Si-O-Si vibration modes. On the other hand, in the FTIR absorption spectra of the "yellow" Si-ncs type higher signals at 870 and 945 cm^{-1} appeared, related to the Si-OH bond vibration. A peak at 3310 cm^{-1} could be related to remanent water originating from the reaction of Si and H_2O_2 (Eq. 3.2).

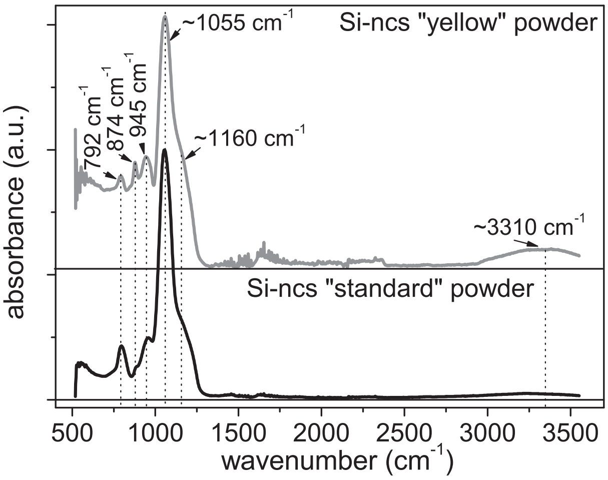

Figure 3.4: *The "standard" and "yellow" Si-ncs/SiO$_2$ sample absorption spectra obtained by FTIR measurement. Taken from [26].*

The average size of the nanocrystals in the Si-ncs "yellow" powder was estimated from the High-Resolution Transmission-Electron-Microscopy (HRTEM) measurement

(JEOL JEM-3010 HRTEM, ÚACH AVČR, Dr. Bakardjieva, see Fig. 3.5(a)). If we assume the size distribution profile to be of a Gaussian shape, the mean core size of Si-ncs will be of ~ 2.69 nm with the FWHM of ~ 0.86 nm. Another scan of this type of Si-ncs can be found in [29] revealing small Si-ncs of sizes between 2-3 nm.

This value is in good agreement with the value estimated from the measurements of Raman spectra. In Fig. 3.5(b) we plotted the Raman spectra of the "standard" and "yellow" Si-ncs/SiO$_2$ sample, compared to that of bulk silicon as a reference. From the peak shift of the "yellow" and "standard" sample compared to the bulk silicon peak, the mean Si-ncs diameter of ~ 2.5 nm and ~ 3.4 nm can be identified for the "yellow" and "standard" Si-ncs/SiO$_2$ sample, respectively. This technique exploits the phonon confinement effects [30]. According to this, etching procedure involving the H$_2$O$_2$ leads to smaller nanocrystals. The size of the "white" Si-ncs was studied in [31] by the Atomic Force Microscopy (AFM). Si-ncs powder was adsorbed on the HOPG (Highly Oriented Pyrolitic Graphite) substrate and the AFM topography scan clearly resolved particles sized between of 1-2 nm.

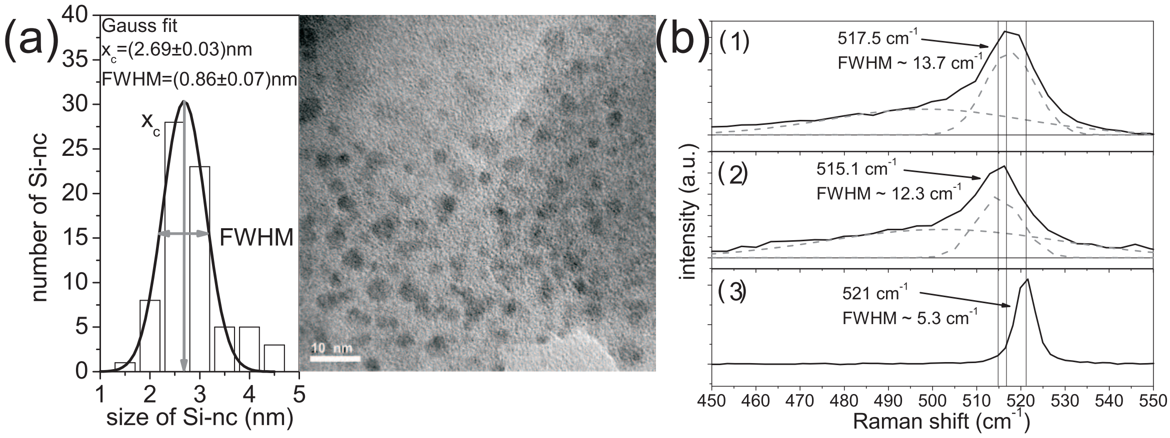

Figure 3.5: *(a) Average size of the "yellow" Si-ncs powder (left) estimated from the HRTEM scan (right). (b) Normalized Raman spectra (full lines) of the (1) "standard" and (2) "yellow" Si-ncs/SiO$_2$ sample and (3) the reference crystalline silicon wafer. Data are fitted with two Gaussian curves (dashed lines) whereas the sharp peak position is (1) at 517.5 cm^{-1} with FWHM of 13.7 cm^{-1} , (2) at 515.1 cm^{-1} with FWHM of 12.3 cm^{-1} and (3) at 521 cm^{-1} with FWHM of 5.3 cm^{-1}. Taken from [26].*

Conclusion

Preparation technique described in this chapter and used for preparation of our samples is relatively simple compared to other methods such as Si$^+$-ion implantation or Plasma Enhanced Chemical Vapor Deposition. Its low price and relatively arbitrary Si-ncs concentration within the SiO$_2$ layer represent additional advantages.

High Si-ncs concentration is desirable in order to prepare samples with high optical gain. However, as we have mentioned above, high concentration may cause Si-ncs agglomeration in the SiO$_2$ based sol-gel matrix. Therefore, the main goal for the future is the optical quality improvement. The mean core diameter of the ”yellow” Si-ncs was estimated by HRTEM and Raman spectroscopy to be of 2-3 nm, the ”white” Si-ncs appears to be even smaller, below 2 nm in diameter. The surface passivation of the H$_2$O$_2$ treated Si-ncs was found by FTIR spectroscopy to be to a certain degree due to a single bonded oxygen such as -OH.

Chapter 4

LIGHT EMISSION FROM Si-ncs/SiO$_2$ SAMPLES

In order to determine the basic optical properties, we studied the light emission from our samples. In particular, we investigated the time-resolved and steady-state photoluminiscence (PL) emission spectra of several types of the Si-ncs/SiO$_2$ samples, prepared from the "yellow" and "white" Si-ncs powders.

4.1 Steady-state PL emission spectra

Essential characterization of our samples can be obtained from the PL emission spectra under continuous wave (CW) excitation. PL was excited at room temperature using a HeCd laser (at 325 nm) and detected by a spectrograph JOBIN YVON coupled to an Andor CCD. PL spectra were corrected for the spectral response of the detection system by calibrated tungsten halogen lamp Oriel. PL emission spectra of the "white" and "yellow" Si-ncs/SiO$_2$ samples and the pure SiO$_2$-based matrix are plotted in Fig. 4.1. For comparison we show in the same figure PL spectra of two reference samples - the "standard" Si-ncs/SiO$_2$ sample (prepared without use of H_2O_2) and the sample prepared by Si$^+$-ion implantation into an infrasil plate (implantation fluence of 6.10^{17} ions/cm^2). Two emission bands can be easily distinguished in both the "white" and "yellow" sample: a blue PL band with a fast decay (the decay will be discussed in detail in the following subsections) of the order of ns (the so-called F-band, abbreviated from the "fast" emission band, peaking at 430 nm) and a yellow-orange PL band with a characteristic decay time of the order of μs (the so-called S-band, abbreviated from the "slow" emission band, peaking above 600 nm). The F-band of the "white" sample is more intense, compared to that of the "yellow" one. Furthermore, the S-band of the "white" sample is spectrally blue-shifted and narrower with respect to the spectra of the "yellow" and other samples. These two different features of the "white" Si-ncs/SiO$_2$ sample PL spectrum can be due to a higher passivation degree of the "white" Si-ncs surface by -OH groups (due to the intense H$_2$O$_2$ etching procedure) and/or due to a smaller Si-ncs core diameter. The "standard" sample does not exhibit a significant F-band contribution. We must notice that the SiO$_2$-based matrix itself exhibits a fast blue emission band at $\sim$ 430 nm, very similar to the F-band in our Si-ncs powders (i.e. with no SiO$_2$-based matrix) as can be seen e.g. in [29] and [31]. Therefore, we assume that the F-band observed in the Si-ncs/SiO$_2$ samples originates from both - the SiO$_2$-based matrix itself and the Si-ncs embedded within the matrix. The PL (S-band) of the Si$^+$-ion implanted infrasil sample peaks at longer wavelengths $\sim$ 780 nm,probably due to a larger mean Si-ncs core diameter and/or due to a different Si-ncs surface passivation.

In the following we will concentrate on the comparison of time-resolved PL emission spectra from the "yellow" and "white" Si-ncs/SiO$_2$ samples only.

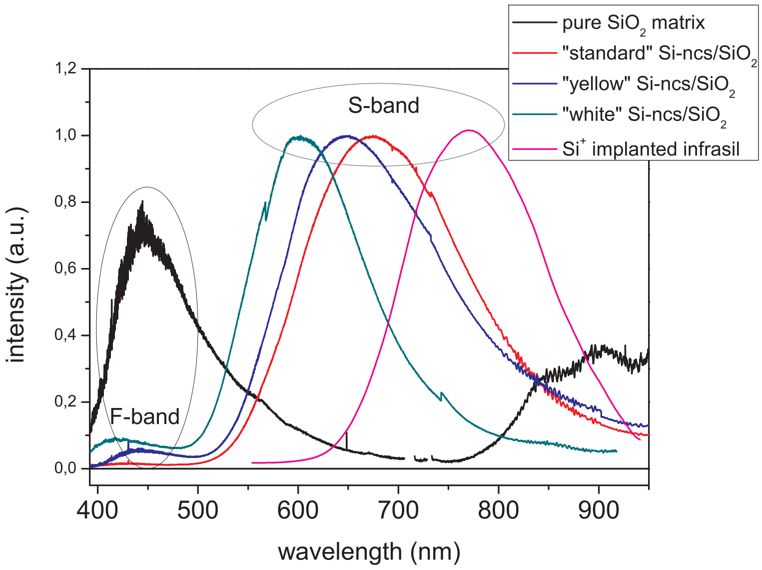

Figure 4.1: *Normalized CW PL emission spectra of the pure SiO$_2$-based matrix, the "white" and "yellow" Si-ncs/SiO$_2$ samples and the two reference samples - the "standard" Si-ncs/SiO$_2$ sample and the Si$^+$-implanted infrasil plate.*

4.2 Time-resolved PL emission spectra

To understand the dynamics of optical processes taking place in our samples, we studied the time-resolved PL emission spectra with a nanosecond resolution. The decay time of the Si-ncs PL under ns resolution reveals two main components - the "fast" one, decreasing in the nanosecond scale (F-band), and the "slow" one, decreasing in the microsecond scale (S-band). These two contributions are spectrally identical with the F-band and the S-band, observed in the CW PL emission spectra. The time-resolved measurements make it possible to study in detail these two components separately. Their origin is still under debate and later on we will propose a possible model of recombination in our Si-ncs/SiO$_2$ samples. In this section, we present a comparison of the time-resolved spectra of the "yellow" and "white" Si-ncs/SiO$_2$ samples, measured with various detection gate delays at room temperature. As an excitation wavelength, a 3rd harmonic of Nd:YAG laser (355 nm) was used. The UV excitation was pulsed with the repetition rate of 10 Hz and pulse duration of 8 ns. The output signal from the sample was collected by an optical fibre coupled to an Andor Shamrock SR163i imaging spectrograph. Signal was detected with an Andor iStar iCCD camera (cooled to -30^{o}C) with the time resolution of 5 ns. PL spectra were corrected for the spectral response of the detection system.

4.2.1 F-band PL emission spectra

In this section we focuse our attention on the time-resolved emission spectra of the F-band, detected using the detection gate width of 5 ns, shifted by the gate step of 1 ns. The CCD detector was pre-triggered in order to measure the signal onset. The gate delay is taken with respect to the pre-triggered time value up to 25 ns.

The time-resolved F-band spectra of the "yellow" Si-ncs/SiO$_2$ sample are presented in Fig. 4.2. The plot shows the detailed PL emission spectra development in time, including the signal onset. The output intensity reaches its maximum value for the gate delay of 10 ns.

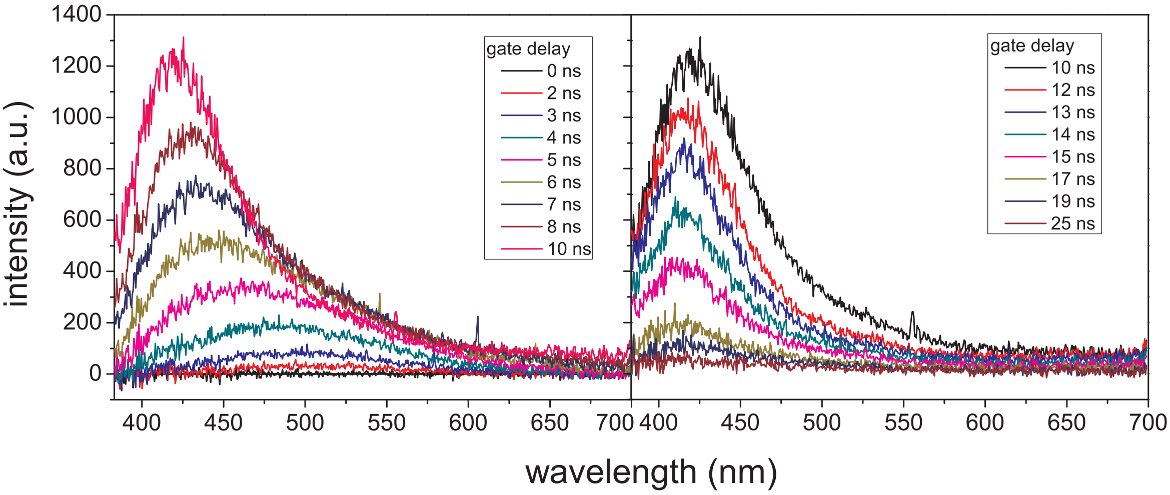

Figure 4.2: *Time-resolved F-band spectra of the "yellow" Si-ncs/SiO$_2$ sample measured with the detection gate width of 5 ns and the gate delay step of 1 ns.*

A similar time-resolved PL emission spectra study was measured on the F-band of the "white" Si-ncs/SiO$_2$ sample. Measured spectra appear to be very similar to

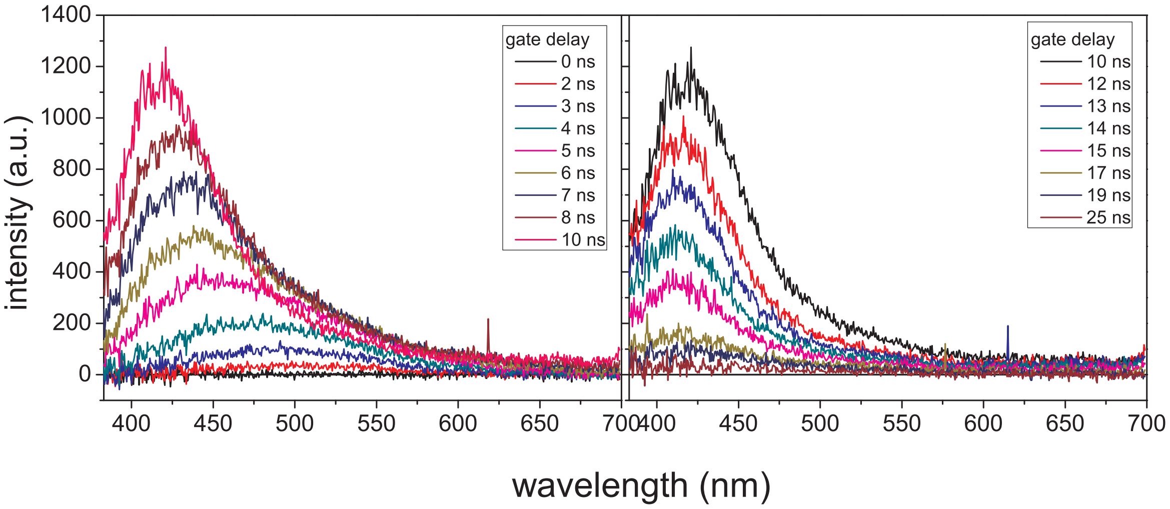

Figure 4.3: *Time-resolved F-band spectra of the "white" Si-ncs/SiO$_2$ sample measured with the detection gate width of 5 ns and the gate delay step of 1 ns.*

the spectra obtained from the "yellow" Si-ncs/SiO$_2$ sample (Fig. 4.3).

The comparison of the 2D map of the normalized F-band spectra of the "yellow" and "white" samples is shown in Fig. 4.4. The peak maximum shifts with increasing time delay towards *shorter* wavelengths. For the gate delay between 0-8 ns the emission peaks at ~ 500 nm and for the gate delay above 10 ns peaks at ~ 430 nm. Such a detailed study of the F-band PL spectra development is necessary in order to specify the detection gate parameters for the F-band optical gain measurements.

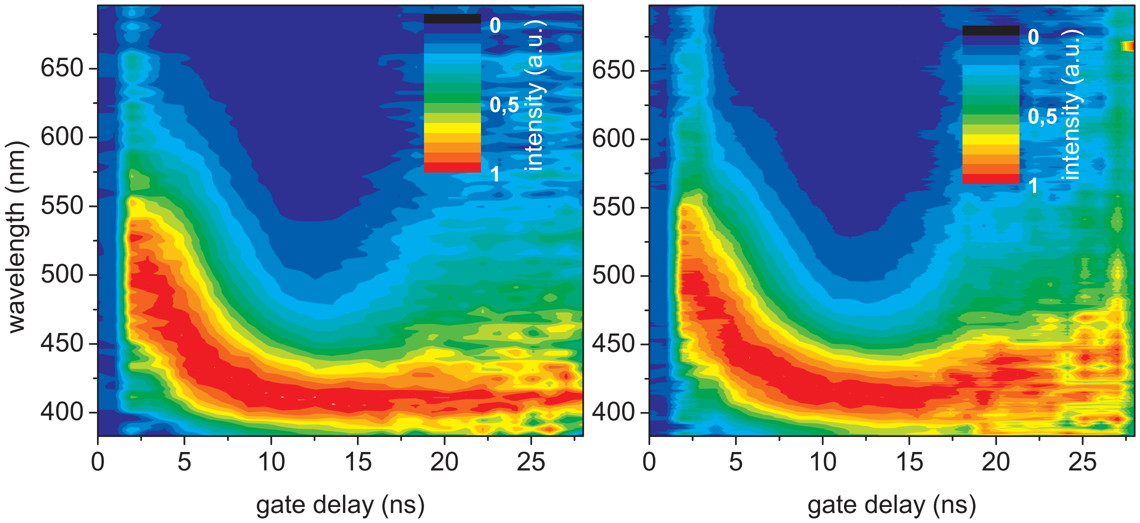

Figure 4.4: *2D map of normalized time-resolved F-band emission spectra of the "yellow" (left panel) and "white" (right panel) Si-ncs/SiO$_2$ samples.*

It seems that the F-band spectral position does not depend on the way of how the Si-ncs are fabricated (etching parameters) and is presumably related to the interface between the core of the Si-ncs and SiO$_2$ matrix or the SiO$_2$ matrix itself [32] (discussion in the previous section). Another interpretation lies within the emission related to the small Si-ncs with the core diameter less than 1 nm [31][33][34].

4.2.2 S-band PL emission spectra

Let us now discuss the results measured on the S-band PL emission component in the "yellow" and "white" Si-ncs/SiO$_2$ samples. Detection parameters, used for the S-band measurement, are as follows: the gate width of 1 μs shifted from the zero delay with respect to pre-triggered time value up to 40 or 50 μs by the step of 1 μs.

Time-resolved PL emission spectra of the "yellow" Si-ncs/SiO$_2$ sample are plotted in Figs. 4.5(a,b). Within the detection window of 0 - 1 μs, coincident with the excitation laser pulse, the F-band at 435 nm dominates, fading away for the longer times (Fig. 4.5(a)). In order to study the S-band contribution separately, we omitted the detection window of 0-1 μs and plotted the S-band time-resolved PL emission spectra separately in Fig. 4.5(b). The emission peaks at 590 nm within the detection window of 1-2 μs and shifts with the gate delay towards longer wavelengths.

The decay time τ and coefficient β at different emission wavelengths in Fig. 4.5(d) were derived from the measurements in Figs. 4.5(a,b), using stretched exponential law

$$I(\lambda, t) = I(\lambda)_0 e^{-(\frac{t}{\tau})^\beta} \ , \tag{4.1}$$

where $0 \leq \beta \leq 1$ (see Fig. 4.5(c)).

We will now describe a method used for fitting the measured data of the output intensity as a function of time in order to obtain the decay time τ and the coefficient β. Let us assume that we have measured the dependence of intensity on time for a certain wavelength $I(\lambda, t)$. By taking a logarithm of Eq. 4.1, we get

$$-\ln\left(\frac{I}{I_0}\right) = \left(\frac{t}{\tau}\right)^\beta . \tag{4.2}$$

If we put $y \equiv -\ln(\frac{I}{I_0})$ and take the the decadical logarithm of Eq. 4.2, we get

$$\log y = \beta \log t - \beta \log \tau \ . \tag{4.3}$$

We derived a linear equation $Y = aX + b$ with slope a, equal to the coefficient β, and the intercept $b = -\beta \log \tau$ from which the decay time can be derived. Using this procedure, the measured data are processed step-by-step by plotting the dependence of $-\ln(\frac{I}{I_0})$ as a function of the delay time t in a log-log scale. Such an analysis increases the accuracy of the coefficient β determination, since we fit the linear function only. This coefficient can be used as a fixed parameter for the further fitting of the decay time τ from the original data using the stretched exponential law (Eq. 4.1), or the decay time τ can be determined directly from the intercept b.

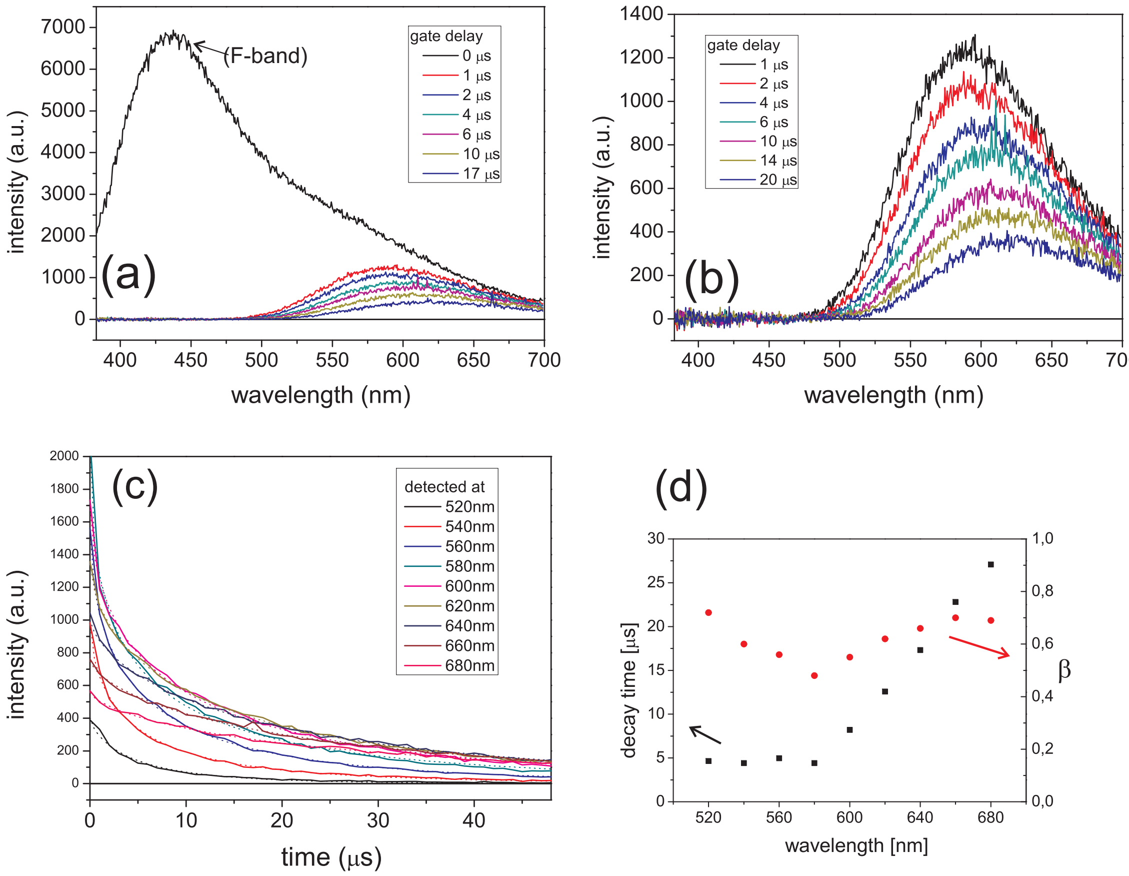

Figure 4.5: *(a) Time-resolved S-band spectra (except the first left top curve) of the "yellow" Si-ncs/SiO$_2$ sample measured with the gate width and step of 1 μs ((b) is detail from (a)). (c) Stretched-exponential PL decay at fixed detection wavelengths. (d) Decay time τ and coefficient β at different emission wavelengths.*

Very similar time-resolved PL emission spectra were obtained for the "white" Si-ncs/SiO$_2$ sample (Fig. 4.6) using the same experimental setup. The PL signal decay can be fitted using the stretched-exponential rule but in this case it is very hard to separate the F-band component from the S-band component in the detection window coincident with the laser pulse. However, our estimates reveal a very similar decay time τ and coefficient β as in the "yellow" Si-ncs/SiO$_2$ sample.

The S-band maximum of the "white" Si-ncs/SiO$_2$ sample shifts with time from $\sim$ 560 nm for the gate delay of 1 μs towards longer wavelenghts (Fig. 4.6(b)). The 2D map of normalized time-resolved PL emission spectra of the S-band in the "yellow" and "white" Si-ncs/SiO$_2$ sample is shown in Fig. 4.7. The spectral red-shift with the delay time is significant in both samples, the S-band of the "white" sample as a whole is spectrally blue-shifted with respect to the "yellow" one. This observation is in the agreement with our observations in the steady-state PL emission spectra.

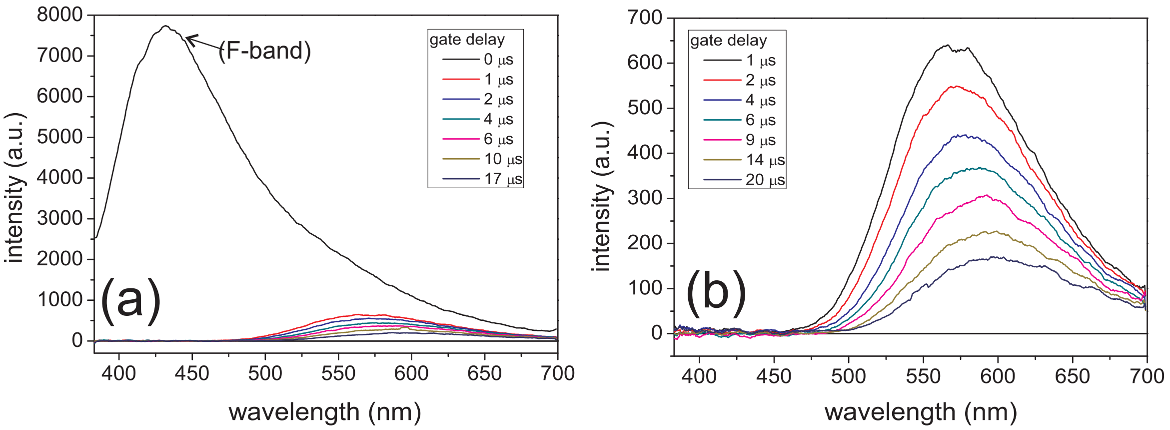

Figure 4.6: *(a) Time-resolved S-band spectra of the "white" Si-ncs/SiO$_2$ sample measured with the gate width and the gate delay step of 1 μs. (b) Detail from (a).*

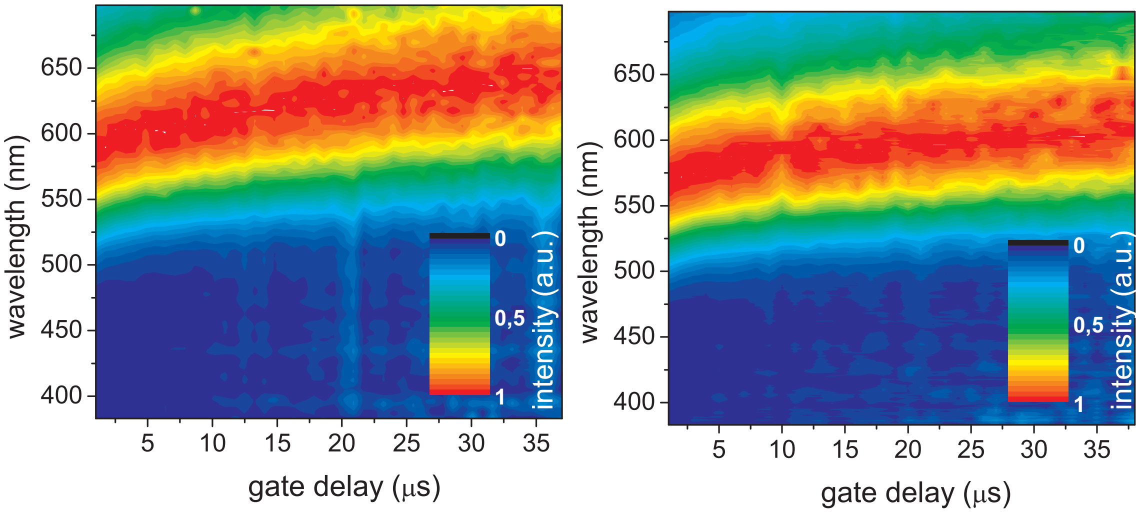

Figure 4.7: *2D map of normalized time-resolved S-band emission spectra of the "yellow" (left panel) and "white" (right panel) Si-ncs/SiO$_2$ samples.*

4.2.3 Comparison of the F-band and S-band components

Finally we present a comparison of the F-band and S-band components in the time-resolved PL emission spectra 2D map for both the "yellow" (Fig. 4.8) and "white" (Fig. 4.9) Si-ncs/SiO$_2$ samples. The F-band component development with increasing delay time (including the signal onset) is displayed on the left panel of the figures and reveals a blue-shift of the peak with the delay time. On the contrary, the right panel with the S-band component exhibits spectral red-shift with increasing delay time, which can be interpreted in terms of reabsorption of light emitted by smaller Si-ncs by the larger ones, emitting at longer wavelengths. Another possible interpretation may be due to a higher oscillator strength in smaller Si-ncs (Eq. 2.16), leading to a shorter radiative decay. As the inhomogeneous broadening of the S-band peak may be partially attributed to the wide Si-ncs size distribution, the smaller nanocrystals

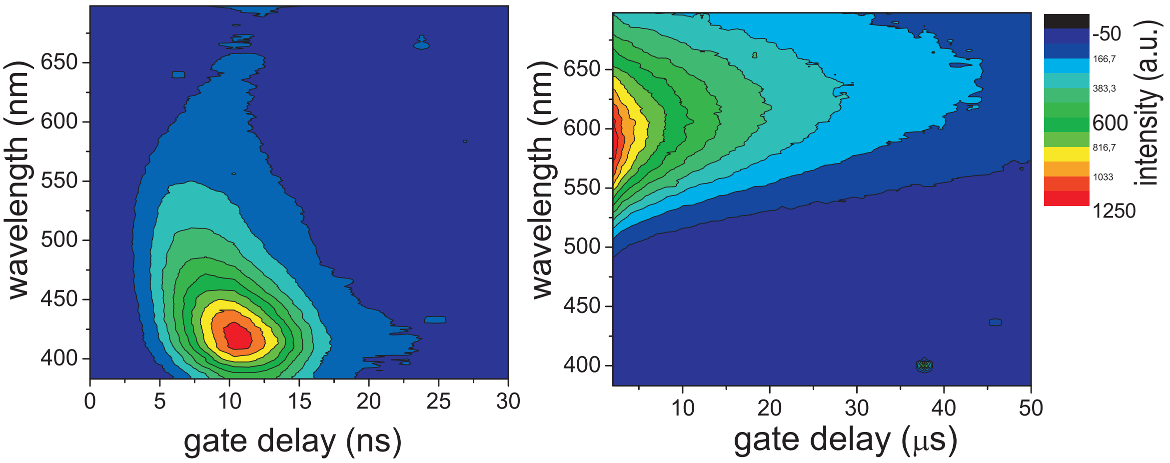

Figure 4.8: *Time-resolved PL spectra of the "yellow" Si-ncs/SiO$_2$ sample. (Left) - the F-band spectra (the gate width of 5 ns and the gate delay step of 1 ns). (Right) - the S-band spectra (the gate width and the gate delay step of 1 μs).*

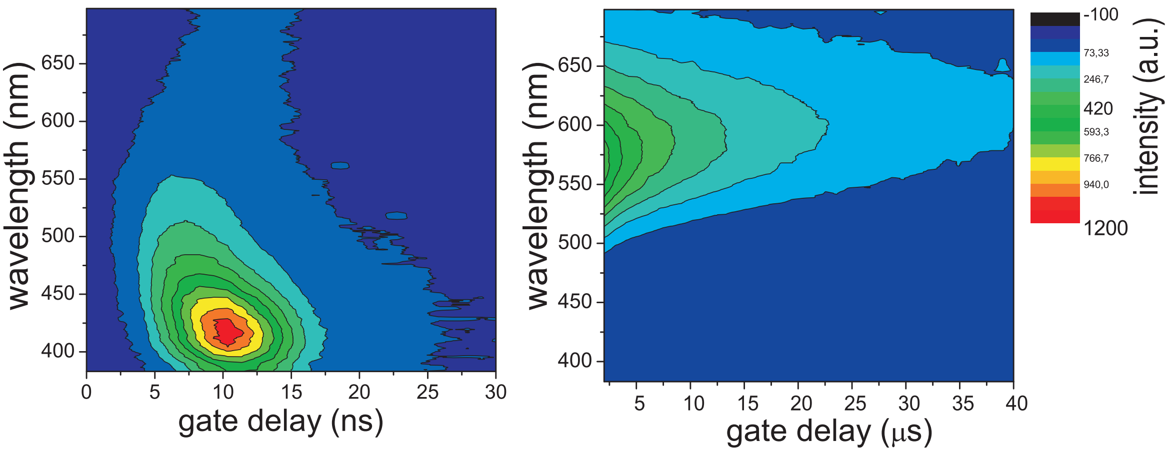

Figure 4.9: *Time-resolved PL spectra of the "white" Si-ncs/SiO$_2$ sample. (Left) - the F-band spectra (the gate width of 5 ns and the gate delay step of 1 ns). (Right) - the S-band spectra (the gate width and the gate delay step of 1 μs).*

emitting with a shorter wavelengths may decay faster than those with the larger core diameter.

Investigation of the time-resolved PL emission spectra of the Si-ncs/SiO$_2$ samples provides an important information about their optical properties. Let us now compare the integrated F-band and S-band components of the two investigated types of samples separately.

The PL emission spectra of the "yellow" Si-ncs/SiO$_2$ sample integrated with the gate width of 10 ns for two different gate delays are shown in Fig. 4.10. PL spectrum measured with the detection gate window of 0 - 10 ns, coincident with the laser pulse (black curve), peaks at 460 - 500 nm ("green"-band in the following). We assume that the energy states inside the Si-ncs (core-related states) are involved in this recombination process. PL spectrum measured with the detection gate window of 10 - 20 ns, i.e. delayed from the excitation pulse by 10 ns (red curve), is located at 400 - 435 nm (F-band). Its origin is usually interpreted as due either to recombinations in some structural defects in the Si-ncs oxide shell [32] and/or due to intrinsic emission from small Si-ncs ($\sim$ 1 nm core diameter)[31][33][34]. Similar behaviour was observed also in the "white" Si-ncs/SiO$_2$ sample.

Comparison of the PL emission spectra of the "yellow" and "white" Si-ncs/SiO$_2$ measured with the detection window of 0-10 ns coincident with excitation pulse ("green"-band) is plotted in Fig. 4.11. The "green" emission from the "white" sample is spectrally blue-shifted compared to the PL emission band of the "yellow" sample. The "white" sample consists of smaller Si-ncs than the "yellow" one due to the different etching parameters used during the samples preparation.

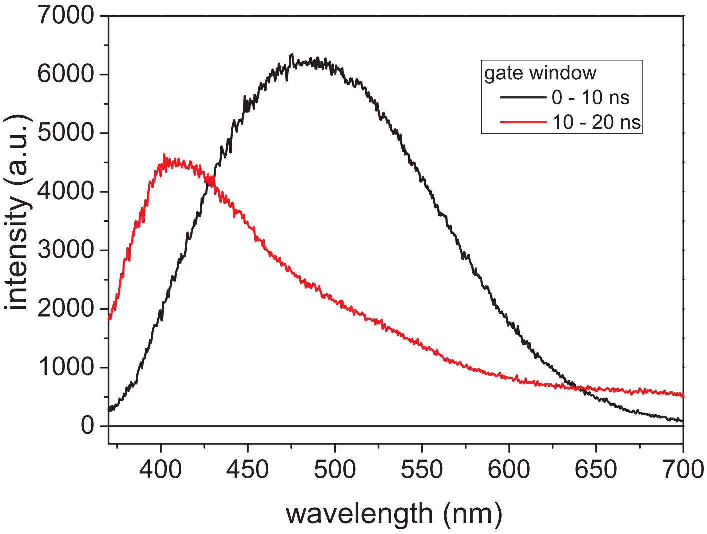

Figure 4.10: *PL spectra of the "yellow" Si-ncs/SiO$_2$ sample integrated over 10 ns gate width with the zero delay (0-10 ns) (black-line) and the delay of 10 ns (10-20 ns) (red-line).*

Let us now discuss the F-band in the "yellow" and "white" type of Si-ncs/SiO$_2$ samples, detected within the first 50 ns after excitation (Fig. 4.12) since the F-band fades away within tens of ns Si-ncs/SiO$_2$. The PL spectra peak at $\sim$ 430 - 470 nm and are similar in both studied samples.

Possibilities of the optical amplification within the F-band, due to its attractive features such as high emission intensity and fast decay, will be investigated in chapter 5, dealing with the optical gain measurements.

The PL emission spectra of the S-band component were measured with a 200 ns gate delay with respect to the excitation pulse (to avoid the F-band component) and gate width of 100 μs. Comparison of the S-band spectra of the "yellow" and "white" Si-ncs/SiO$_2$ samples is shown in Fig. 4.13. The PL emission band of the "white"

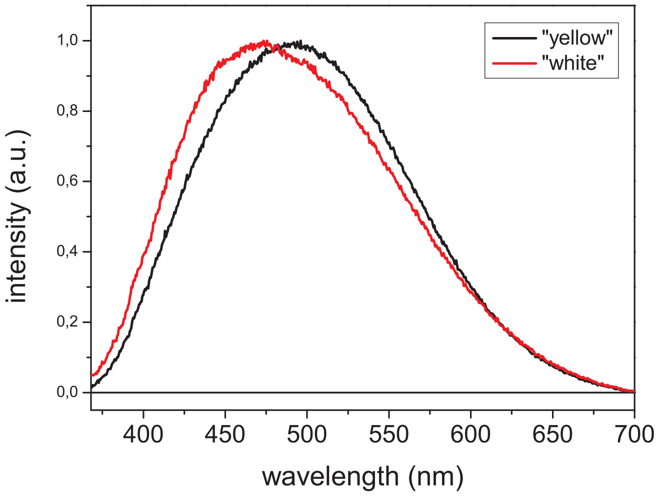

Figure 4.11: *Time-integrated PL spectra of the "yellow" (black-line) and "white" (red-line) Si-ncs/SiO$_2$ samples. Both curves represent signal integrated within the gate width of 10 ns measured in coincidence with the excitation pulse (a "green" emission band).*

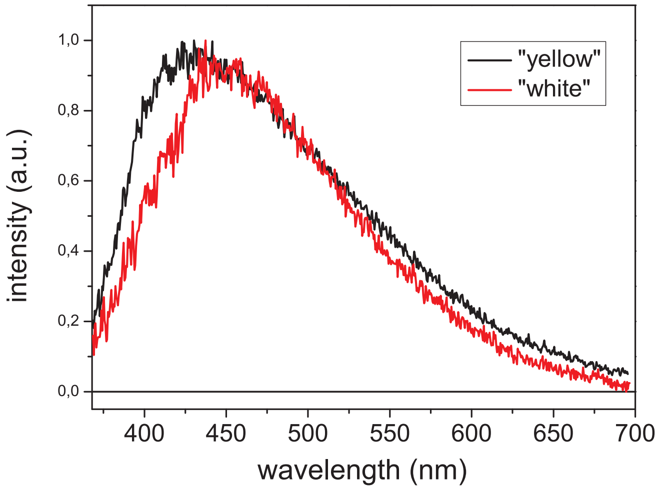

Figure 4.12: *Normalized F-band emission spectra of the "yellow" (black-line) and "white" (red-line) Si-ncs/SiO$_2$ samples. Signal was detected with the gate width of 50 ns, coincident with the laser pulse.*

sample peaks at 580 - 615 nm and is slightly spectrally blue-shifted with respect to the emission band of the "yellow" sample which peaks at 600 - 635 nm. This can be due to the presence of smaller Si-ncs within the "white" sample, compared to the "yellow" one and/or due to a different surface passivation, as we discussed in the previous sections.

Finally, in Fig. 4.14 we present the PL emission spectra of the "yellow" and "white" Si-ncs/SiO$_2$ sample integrated with the gate width of 100 μs with no gate delay. These PL emission spectra appears to be similar to that excited by CW laser (Fig. 4.1). The main difference between the integrated PL spectra of the "yellow" and "white" samples in Fig. 4.14 are (i) the blue-shifted S-band and (ii) stronger

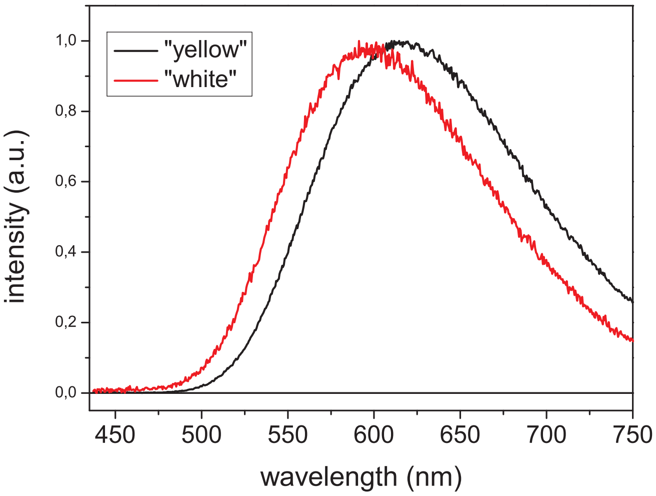

Figure 4.13: *Normalized S-band emission spectra of the "yellow" (black curve) and "white" (red curve) Si-ncs/SiO$_2$ samples. Signal was detected with the gate delay of 200 ns and the gate width of 100 μs.*

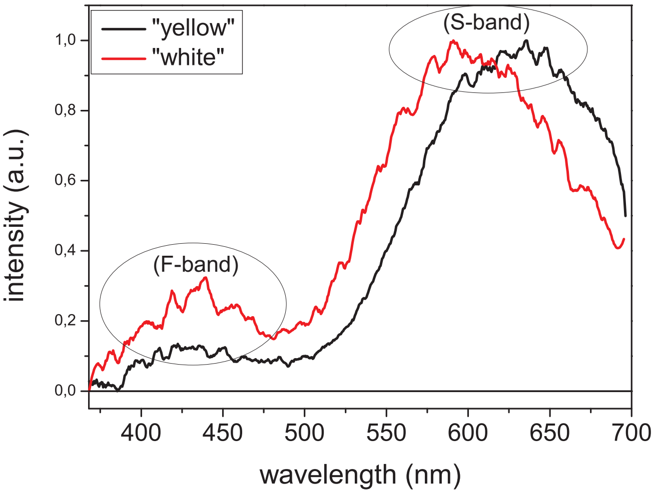

Figure 4.14: *Normalized PL emission spectra of the "yellow" (black-line) and "white" (red-line) Si-ncs/SiO$_2$ samples. Signal was detected with the gate width of 100 μs and no delay with respect to the excitation pulse.*

signal from the F-band in the "white" sample, compared to the "yellow" one. This may be due to a different Si-ncs core size distributions and/or differencies in Si-ncs surface passivation (as follows from the theoretical calculations by Puzder et al. in [35], especially the higher degree of passivation by -OH group may lead to the S-band spectral blue-shift beyond the spectral limit presented by Wolkin et al. [36]).

With respect to our results presented in this chapter we will study the optical gain of the F-band and S-band emission components separately. The results are discussed in the next chapter.

Chapter 5

OPTICAL GAIN IN Si-ncs/SiO$_2$ SAMPLES

Positive value of the optical gain is one of the most relevant prerequisites for an active optoelectronic material. Another important parameter, necessary for the StE onset, is a high optical quality (low losses by light scattering in the sample). In this chapter we will present a method for measuring the optical gain in semiconductors called Variable Stripe Length (VSL) technique, proposed in 1971 by K.L. Shaklee [37]. This technique has several limitations, such as low optical gain coefficient that we expect to have in our samples. That is the reason why the VSL results have to be compared with results measured by a complimentary Shifting Excitation Spot (SES) technique as proposed by Valenta et al. in [38][39].

5.1 Variable Stripe Length (VSL) Technique

The VSL technique is a kind of degenerated "Pump and Probe" method where the "Probe" beam is substituted by a spontaneous emission in the sample. Therefore it can be used only in samples with strong luminiscence at studied wavelength. As a source of the "Pump" beam should be used a laser possessing a rectangular beam cross section in order to assure a homogeneous excitation density distribution over the whole stripe length l. An appropriate laser system from this point of view is either an excimer or N$_2$-laser. It is possible to use also a Gaussian laser beam profile (e.g Nd:YAG as a laser source), however, one has to ensure its homogenity along the excitation stripe length [38] by e.g. utilising the combination of a beam expander and a rectangular slit.

In this method a sample is excited with a homogeneous narrow excitation stripe made of a laser beam focused by a cylindrical lens onto the sample surface. Instead of creating the excitation stripe by a cylindrical lens directly on the sample surface, it is more appropriate to place a set of two additional spherical lens between the cylindrical lens and the sample (a double projection system). Using the double projection system has great advantages if its magnification ratio M is less than unity. In such a case, the accuracy of the stripe length determination increases and the inevitable diffraction effects of the excitation beam on the adjustable slit jaws are minimized [23].

The VSL experimental setup is sketched in Fig. 5.1. The excitation stripe works as an optical pump of the sample and it can build-up a population inversion in the illuminated area. The spontaneous emission from the excited area is emitted randomly in all directions but only the part of it, emitted in the stripe axis direction, can be amplified by stimulated emission. The Amplified Spontaneous Emission (ASE) I_{VSL} is detected from the edge of the sample as a function of the excitation stripe length l (being changed by the adjustable (moving) screen). The detection system is placed along the axis of the excitation stripe and the light is collected either by a spherical lens or an optical fibre and focused onto the spectrograph slit.

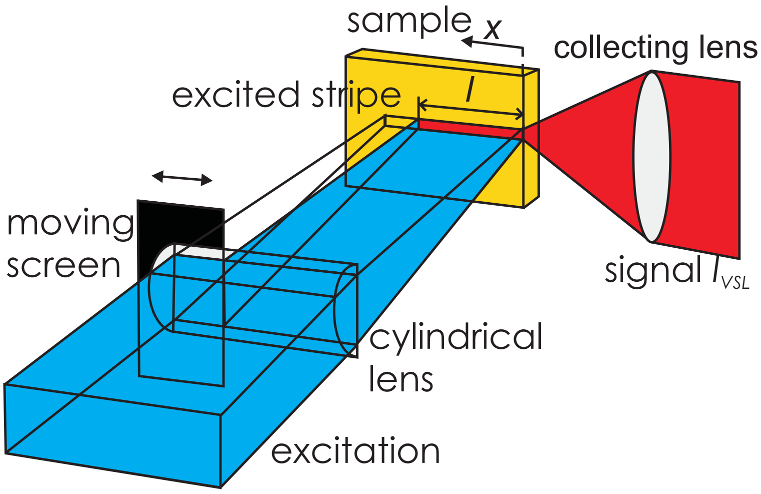

Figure 5.1: *A sketch of the VSL experimental technique (for the sake of simplicity the double projection system is omitted).*

Let us now theoretically describe an one-dimensional (1D) VSL model, used for the description of the VSL signal. In order to meet the 1D requirement we assume that the excitation stripe width w is infinitely small ($w \ll l$). The net gain coefficient $G(\lambda)$ is defined as a relative change of the light intensity $I(x, \lambda)$ at a wavelength λ passing an infinitesimal distance dx

$$G(\lambda) = \frac{1}{I(x,\lambda)} \frac{\mathrm{d}I(x,\lambda)}{\mathrm{d}x} = g(\lambda) - K \;, \tag{5.1}$$

where K stands for the optical losses caused by light scattering and $g(\lambda)$ is a gain coefficient equal to negative band-to-band absorption coefficient $\alpha(\lambda)$. We assume that $g(\lambda)$ does not depend on the position x along the stripe (homogeneous sample) and that the excitation beam profile is homogeneous. The total change of the detected intensity when increasing the stripe length by dx is given as a sum of spontaneous emission $I_{SpE}(\lambda)$ and the amplified spontanous emission (ASE) caused by the StE onset

$$\mathrm{d}I_{VSL}(x,\lambda) = G(\lambda)I_{VSL}(x,\lambda)\mathrm{d}x + I_{SpE}\mathrm{d}x \tag{5.2}$$

where $I_{SpE}(\lambda)$ and the coupling of emission to the detector is constant along the excitation stripe (independent of position x). By solving the previous equation we obtain the classical 1D VSL equation for the measured ASE signal I_{VSL} as a function of the stripe length l

$$I_{VSL}(l,\lambda) = I_{SpE}(\lambda)\frac{e^{G(\lambda)l}-1}{G(\lambda)}\ . \tag{5.3}$$

By fitting the measured ASE signal I_{VSL} with Eq. 5.3 we can evaluate the net gain coefficient $G(\lambda)$ at a specific wavelength. Eq. 5.3 does not describe the situation for longer excitation stripe lengths l, when saturation of the VSL signal occurs, therefore this formula can be used for shorter excitation stripe lengths only. More complex spectrally resolved analysis involves measurements of $I_{VSL}(l,\lambda)$ and $I_{VSL}(2l,\lambda)$ at two stripe lengths l and $2l$. From Eq. 5.3 we can derive an analytic expression for the gain spectrum $G(\lambda)$

$$G(\lambda) = \frac{\ln(\frac{I_{VSL}(2l,\lambda)}{I_{VSL}(l,\lambda)}-1)}{l}\ . \tag{5.4}$$

The use of this model is limited to higher optical gain coefficient, however, in materials with lower optical gain, the VSL signal can be accompanied with several artifacts which can act like a positive optical gain. Therefore the Shifting Excitation Spot (SES) technique is used as an additional measurement to get rid of some of these artifacts. In the following section we will discuss the limitations of the VSL in low optical gain materials, such as in our samples of the Si-ncs embedded in the SiO$_2$-based matrix.

5.1.1 VSL limitations and artifacts in low-gain materials

The low gain limit of the VSL method is given by a condition $Gl \ll 1$. In this case we can simplify Eq. 5.3 into $I_{VSL}(l,\lambda) \approx I_{spE}(\lambda)l$, which means that the detected signal is independent of the gain value. In such a case we are not able to decide whether the StE onset appeared and we can not derive the net gain coefficient solely from the VSL measurements. Furthermore, in low gain materials, it is usually difficult to distinguish several unwanted effects (artifacts) from the real gain, which can lead to misinterpretation of the measured data. To avoid these artifacts we have to ensure the validity of the 1D VSL theoretical model and therefore several conditions must be fulfilled [38].

Firstly, the excitation intensity over the whole VSL excitation stripe length has to be constant. As we have already mentioned, it means that the laser beam profile must be homogeneous. Even if we use such an ideal beam profile, inevitable Fresnel diffraction occurs at the edges of the movable slit and creates interference fringes in the VSL stripe profile [23] (Fig. 5.2). Due to that, in the measured VSL signal, an abrupt increase of the signal appears, which might be interpreted by accident as a positive optical gain and must not be included in further data processing. The stripe width has to be minimized in order to prevent internal reflections within the excited area and fulfill the 1-dimensionality of the stripe, required by the model. The stripe width can be controlled by using double projection system with magnification below one and placing the sample precisely into the focal plane of the laser beam. In our measurements, the usual width of the VSL excitation stripe is below 30 μm which appears to be fully sufficient.

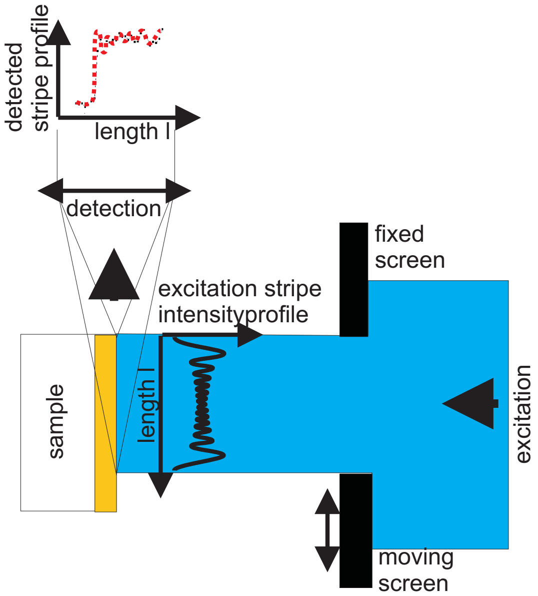

Figure 5.2: *Diffraction effect at the edges of the movable slit.*

Secondly, the conditions imposed on the sample are homogenity and planarity of the Si-ncs -rich layer. Besides that, the sample has to be placed perpendicularly to the pumping beam.

Third very important requirement for the adequate performing of the VSL method is the constant coupling of the light emitted from the sample (ASE) to the detection system, i.e. the coupling efficiency must not depend on the length of the excitation stripe. When the focal plane of the detection lens is not at the edge of the sample but inside the sample, coupling efficiency exhibits a maximum for a certain stripe length, coincident with the position of the focal plane of the detection lens. This may result in a false-gain increase in the measured signal. The effect of the non-constant coupling can be revealed by the SES technique (see the next paragraph). In our experimental setup we use (instead of lens) an optical fibre for the light collection from the edge of the sample, coupled to the spectrograph with the CCD camera. The optical fibre helps us to detect the signal output from the sample edge with a spatial resolution (i.e. we do not detect signal scattered in the sample).

Finally, the waveguiding effects might occur due to the change in refractive index (nonlinear effects) when using high pump densities. These effects are not included in the 1D VSL model and they might also cause a gain-like increase in the detected signal.

5.2 Shifting Exctitation Spot (SES) Technique

Let us now describe the SES technique which is a complementary method to the VSL technique that will help us to reveal the gain-like artifacts mentioned in the previous paragraph. It should be used for low-gain materials characterization in conjunction with the VSL to prove the StE onset in the sample. The SES experimental setup is very similar to the VSL one, only the moving screen is replaced by a narrow moving slit which forms only a small excitation spot on the surface of the sample (Fig. 5.3).

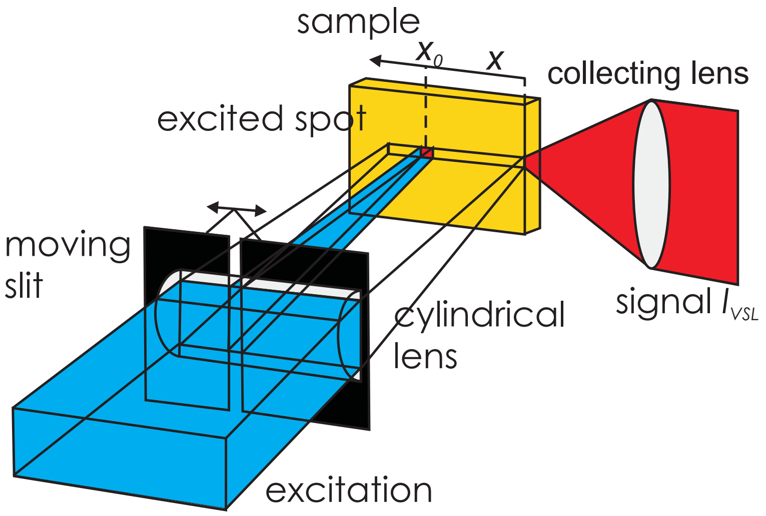

Figure 5.3: *The sketch of the SES experimental setup (for the sake of simplicity the double projection system is omitted).*

The excitation spot shifts along the "x" axis in the same place as the VSL excitation stripe (to avoid the sample inhomogenity influence). The excited area has be to small enough in order to prevent the StE onset. Then light emitted from the excited area will be attenuated when passing through the unexcited part of the sample and the SES signal I_{SES} detected at the edge of the sample follows the Beer-Lambert law

$$I_{SES}(x,\lambda) = I_{SpE}(\lambda)e^{-\alpha_{tot}(\lambda)l} \;, \tag{5.5}$$

where α_{tot} stands for the total optical losses in the material caused by band-to-band absorption and light scattering (as in the VSL) and parameter x is the position of the spot in the sample measured from the sample edge ($x \in \langle 0, l\rangle$, l is the length of the "virtual" stripe). This relation holds only when any artifacts and parasitic effects do not appear in the detected signal.

On the other hand, the fluctuations of the SES signal prove the presence of unwanted artifacts. Important is that the SES signal includes the same artifacts as the VSL signal, except the StE effect. Therefore, comparison of an integrated SES signal over the stripe length l ($\int_0^l I_{SES}(x,\lambda)\mathrm{d}x$) with the detected VSL signal $I_{VSL}(l,\lambda)$ suggests three possibilities of the sample behaviour:

- $I_{VSL}(l,\lambda) = \int_0^l I_{SES}(x,\lambda)\mathrm{d}x$ - no StE is present in the sample.
- $I_{VSL}(l,\lambda) < \int_0^l I_{SES}(x,\lambda)\mathrm{d}x$ - saturation of the VSL signal due to high pumping densities or induced absorption occurence.
- $I_{VSL}(l,\lambda) > \int_0^l I_{SES}(x,\lambda)\mathrm{d}x$ - the evidence of the stimulated emission onset in the sample.

The last condition can be expressed using Eq. 5.3 and Eq. 5.5 as

$$I_{SpE}(\lambda)\frac{e^{G(\lambda)l}-1}{G(\lambda)} > I_{SpE}(\lambda)\frac{1-e^{-\alpha_{tot}(\lambda)l}}{\alpha_{tot}(\lambda)} \;. \tag{5.6}$$

We can define a difference $\Delta(\lambda,l)$ between the VSL and integrated SES (intSES) curve as

$$\Delta(\lambda,l) = I_{SpE}(\lambda)\Big(\frac{e^{G(\lambda)l}-1}{G(\lambda)} - \frac{1-e^{-\alpha_{tot}(\lambda)l}}{\alpha_{tot}(\lambda)}\Big) \;. \tag{5.7}$$

In the end of this section, let us to propose a formula that can be used for the evaluation of the net gain coefficient $G(\lambda)$ in the case of low overall optical losses. Then $\alpha_{tot}(\lambda)l \ll 1$ and the intSES curve is a linear function of the stripe length ($intSES = I_{SpE}(\lambda)\frac{1-e^{-\alpha_{tot}(\lambda)l}}{\alpha_{tot}(\lambda)} \approx I_{SpE}l$). Moreover, we assume that we are evaluating the net gain coefficient for long excitation stripe and high excitation density, i.e. $Gl \gg 1 \Rightarrow e^{Gl} \gg 1 \Rightarrow e^{Gl}/G \gg l$. Than we can simplify Eq. 5.7 into

$$\Delta(\lambda,l) \approx I_{SpE}(\lambda)\frac{e^{Gl}}{G(\lambda)} \;. \tag{5.8}$$

Therefore, for a given emission wavelength, sufficient stripe length (long enough to ensure the condition $Gl \gg 1$) and the VSL/intSES difference (from the experiment), the net gain coefficient $G(\lambda)$ can be evaluated from a graphic solution of Eq. 5.8. The minimal value of the net optical gain is given as

$$G_m(\lambda) = \frac{\ln(\Delta(\lambda, l)}{l} \; . \tag{5.9}$$

We can conclude that the evaluation of the net gain coefficient could be, in principle, done by several ways:

- By fitting the ASE signal (VSL curve) with Eq. 5.3, but only for relatively short excitation stripes, when the signal is not saturated. However, as we will see in the next part of this chapter, the VSL curve in our samples is rather linear function of the excitation stripe length which is probably due to low optical gain coefficient and/or due to weak waveguiding effects within the Si-ncs layer [40][41]. Therefore in our case we cannot use the simple Eq. 5.3 for the net gain evaluation.
- By using Eq. 5.4, however, in this case an exponential shape of the VSL curve is needed.
- By fitting the VSL/intSES difference with Eq. 5.7. In this case the coefficient of overall optical losses in the material has to be known, especially the light scattering coefficient K.
- By evaluating Eq. 5.9 for a specific stripe length. Optical gain values obtained by this method are only approximate.

5.3 VSL and SES experimental setup and a necessary condition for the optical gain presence in a sample

In the previous section we derived the simple theoretical condition for the StE onset in the sample, given by Eq. 5.6, which compares the signals obtained by the VSL and SES methods. It says that if the positive net gain coefficient has been observed, the VSL curve must be placed above the integrated SES curve or in other words - the VSL/intSES difference given by Eq. 5.7 has to be positive. It is based on the fact that the artifacts and losses by scattering are included in both the VSL and SES signals, while the StE can be present only in the VSL data. Our further experimental results will be processed with respect to this simple rule and 2D maps of the difference between VSL and SES will be examined.

In what follows we describe the VSL and SES experimental setup. The sketch of the experimental setup used throughout the thesis is plotted in Fig. 5.4. As a source of the excitation an UV pulse laser Nd:YAG (355 nm, 8 ns pulse duration, 10 Hz repetition rate) was used, whose narrow beam diameter was broadened by a beam expander. It has a Gaussian beam profile but nearly homogeneous intensity distribution can be achieved within the excitation stripe (example is given in Fig. 5.5). The laser beam profile was measured using OPHIR profilemeter every time before the VSL/SES experiment (to eliminate the laser beam instability effect). Wavelength of the laser beam is suitable for excitation of the Si-ncs/SiO$_2$ samples, because they respond with a high absorption and a strong PL emission. Moreover, the pulsed character of the excitation is necessary for the StE onset since the induced absorption by free carriers disables the population inversion build-up during the excitation pulse incident to the sample.

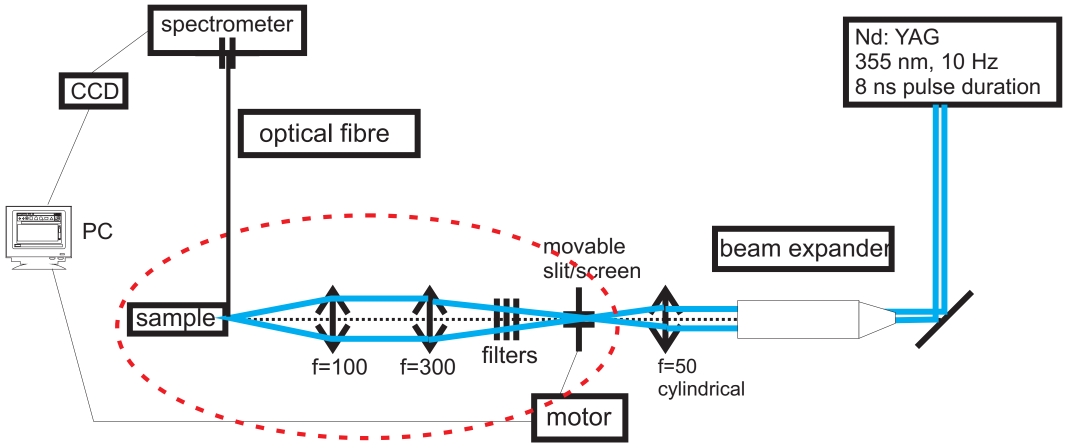

Figure 5.4: *VSL and SES experimental setup.*

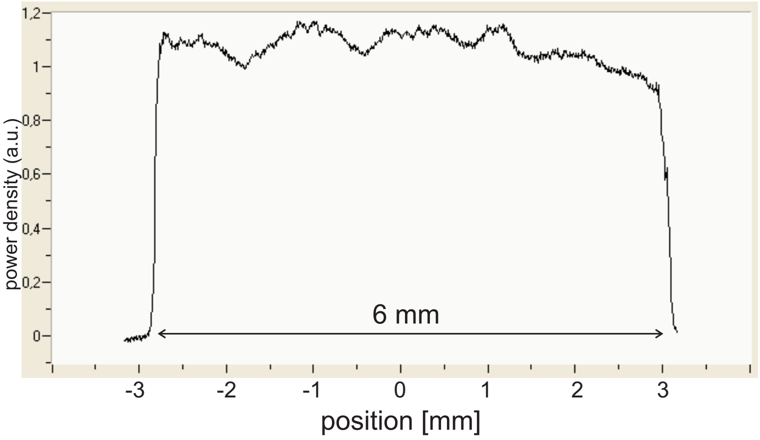

Figure 5.5: *Excitation beam profile.*

The expanded beam is focused with a cylindrical lens (focal length of 50 mm) into the stripe and the focal plane of the lens is located nearby the movable screen (slit) to ensure a perfect cut of the excitation stripe. Double projection system with a magnification of M=0.3, consisting of two spherical quartz lenses with focal lengths of 300 and 100 mm, is used to project the excitation stripe onto the sample surface. As mentioned above, the double projection system minimizes the diffraction effects that originate from the Fresnel diffraction on the movable screen (slit). The VSL/SES signal was collected by an optical fibre located at the edge of the sample, coupled to the detection system composed of an Andor Shamrock SR163i imaging spectrograph, coupled with an Andor iStar iCCD camera (cooled to -30^{o}C, time resolution of 5 ns). All presented spectra were corrected for the spectral response of the detection system and the measurements were done at room temperature.

5.4 Experimental results in different Si-ncs/SiO$_2$ samples

In this section, the experimental results obtained from the VSL and SES measurements are presented. We performed a sufficient number of measurements under different conditions in order to investigate the presence of the optical gain. Time-resolved VSL/SES measurements were realized for each sample with different detection gate window and gate delay (F-band and S-band emission component) in dependence on the increasing pumping density. A method that we used for data processing allowed us to create 2D maps of difference between the VSL and integrated SES (intSES) curves (given by Eq. 5.7) as a function of the excitation stripe length and the emission wavelength.

5.4.1 Gain measurements on the F-band emission component

As we have shown in chapter 4, the PL emission component with the nanosecond decay time at $\sim 430 - 450$ nm is called the F-band ("fast") emission component. In the same chapter, it was also shown that except the F-band component there is a "green" emission band present during and immediately after the excitation (excitation pulse duration of 8 ns, repetition rate of 10 Hz). And for that reason, we decided to perform the VSL/SES measurement on the nanosecond time scale after the excitation to confirm the StE onset based on the condition given by Eq. 5.6. We focused on two detection windows: (i) [0 - 20 ns] (in coincidence with the excitation pulse) where the "green" emission band was observed (Figs. 4.10, 4.11) and (ii) [0 - 50 ns] where the "blue" F-band contribution dominates (Fig. 4.12). The positive VSL/intSES difference itself is not sufficient in order to confirm the presence of optical gain in a certain material. It is also desirable to observe a threshold behaviour of the dependence of the output intensity on the pumping density and narrowing of the measured spectrum with increasing either the length of the stripe and/or the excitation intensity.

5.4.1.1 Detection gate window of 0-20 ns

The time-resolved PL emission spectra of the F-band revealed a relatively strong and broad PL emission band peaked at $\sim$ 500 nm within the first 10 ns (detection gate width of 10 ns coincident with the laser pulse) after excitation (Fig. 4.10). This "green" PL emission peak remains visible also in the next detection window of width of 10 ns, but is weaker, compared to the F-band peaked at $\sim$ 435 nm. Therefore, we decided to perform the optical gain measurement separately within two detection

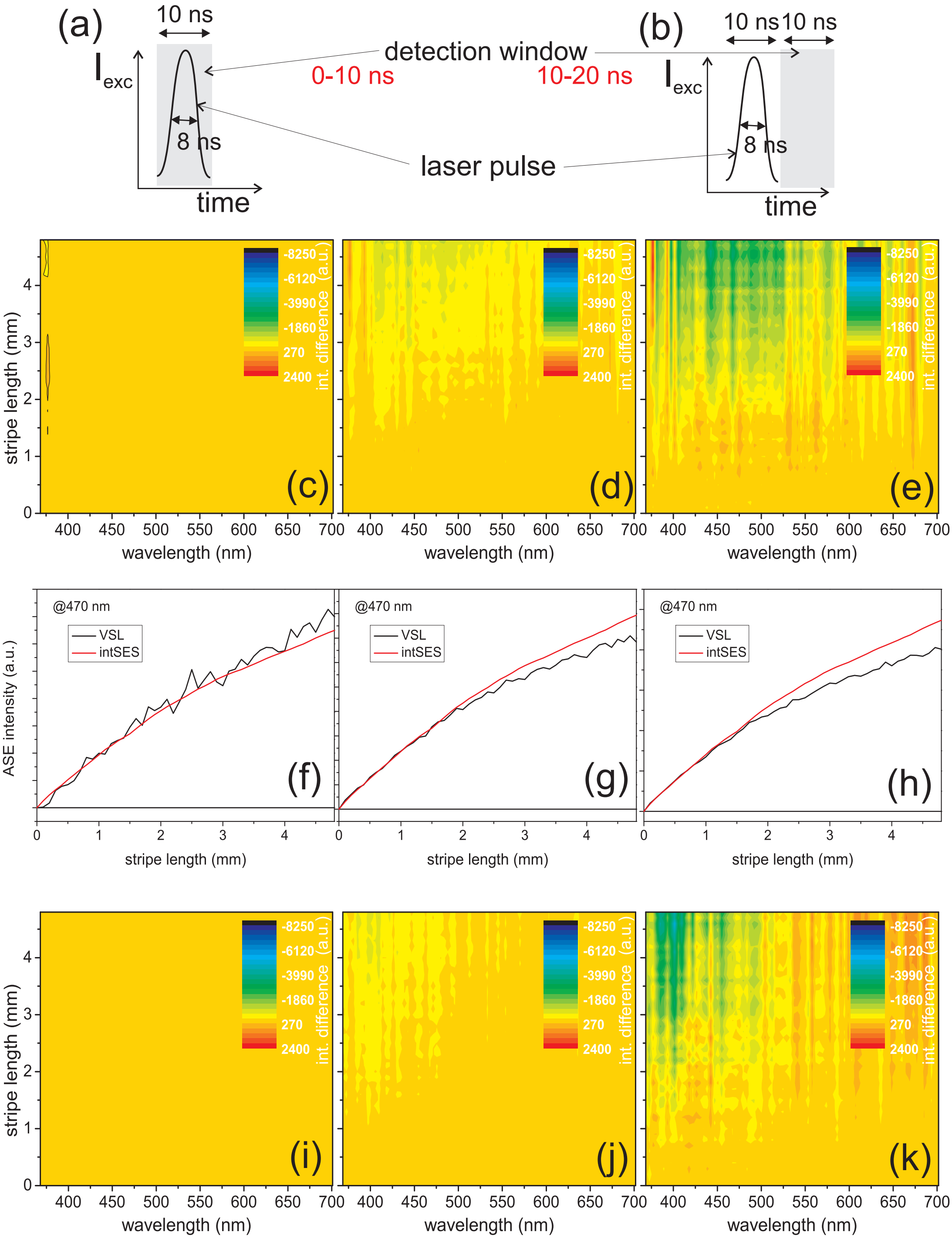

Figure 5.6: *Schematic sketch of the detection gate (of width of 10 ns) position, compared to the excitation laser pulse (a) coincident with the laser pulse; (b) with the gate delay of 10 ns with respect to the laser pulse. (c-e) Two-dimensional map of the "green" emission band VSL/intSES difference (Eq. 5.7) of the "yellow" Si-ncs/SiO$_2$ sample for excitation densities of (c) 0.02 MW/cm^2, (d) 0.2 MW/cm^2, (e) 2.4 MW/cm^2 detected with the detection parameters displayed in (a). (f-h) The VSL (black line) and integrated SES (red line) curves, taken from graphs (c-e) at emission wavelength of 470 nm. (i-k) 2D-map of the VSL/intSES difference (Eq. 5.7) of the "yellow" Si-ncs/SiO$_2$ sample for the same excitation densities as in (c-e) detected with the detection parameters displayed in (b).*

windows, which are for illustration plotted in Fig. 5.6 on panel (a) - a detection gate window of 0-10 ns, coincident with the laser pulse and (b) - a detection gate window of 10-20 ns, delayed from the excitation pulse. A negative difference between the VSL and integrated SES curves was observed for higher excitation densities for both detection windows (Figs. 5.6(c-k)). The intensity difference scale is fixed in all 2D-maps to emphasize that the negative VSL/intSES difference is higher in case of the detection window coincident with the laser pulse (0-10 ns). The VSL and integrated SES extracted from Figs. 5.6(c-e) at the emission wavelength of 470 nm are plotted separately in Figs. 5.6(f-h). Results presented in Fig. 5.6 were measured in the "yellow" Si-ncs/SiO$_2$ sample, however, the results from the "white" Si-ncs/SiO$_2$ sample are very similar.

This phenomenon can be explained in terms of the induced transient nonlinear absorption. The positive nonlinear absorption change $\Delta\alpha(I_{exc})$ was reported by S. Vijayalakshmi et al. in the [42] who measured the $\Delta\alpha(10\mathrm{MW/cm}^2) \approx 500$ cm^{-1} for the 3 nm Si-ncs in SiO$_2$ matrix excited by the laser with wavelength of 355 nm and pulse duration of $\tau = 10$ ns (note the very similar experimental conditions to ours).

Model of recombination processes in the detection window of 0-10 ns

In this subsection we will propose a model of recombination processes in Si-ncs, which are dominant during the excitation and immediately after. Carriers are excited by the laser pulse into higher virtual energy states and then thermalize (∼fs-ps) to lower energy levels that are schematically plotted in Fig. 5.7. These levels include the Si-ncs core related states, structural defects states (within the interface layer) and small Si-cluster states. According to the PL emission spectra (Fig. 4.10 (black line)) measured with the detection window of 0-10 ns (coincident with the laser pulse), we propose that the dominant radiative recombination process within the first 10 ns is the direct recombination in the core of the Si-ncs (Fig. 5.7 (green line)). The lowest excited energy states are repopulated by the relatively long excitation pulse, which increases the probability of the radiative recombination from these core-related states, even though the trapping rate to the surface/interface states is of the order of $\sim$ 400 fs [43]. The emitted "green" light is strongly reabsorbed by the other Si-ncs in the SiO$_2$ matrix due to the induced nonlinear absorption when the sample is excited by the VSL excitation stripe and therefore the StE can not occur between the core-related energy states. A weak F-band can be also seen in the spectra (Figs. 5.6(d,e)). Its relatively weak intensity is probably due to slower dynamics of the F-band, compared to the "green" one. As we have already mentioned, the F-band is usually described as the radiative recombination in structural defects of

Si-ncs shell or small Si-clusters (Fig. 5.7 (blue line)).

Within the detection window of 10-20 ns (with respect to the excitation pulse), most of the carriers that were located at the core-related states are now trapped into the surface/interface states. Therefore the F-band overgrows the ”green”-band emission (Fig. 4.10 (red line)). Possible recombination processes are sketched in Fig. 5.8; the dominant process is the F-band emission.

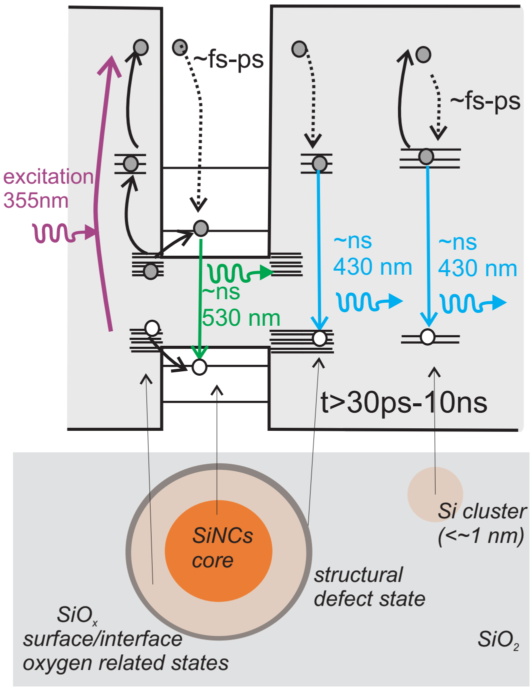

Figure 5.7: *Recombination model of radiative processes dominant in the detection window of 0 - 10 ns, coincident with the laser pulse.*

5.4.1.2 Detection gate window of 0-50 ns

In this section we focus our attention on the VSL/SES measurements with the detection gate width of 50 ns, coincident with the laser pulse (see Fig. 5.9 for better understanding). We observed the positive VSL/intSES difference for both studied Si-ncs/SiO$_2$ samples (the ”yellow” and ”white” one), which we will present separately below.

”White” Si-ncs/SiO$_2$ samples

The experimental results of the VSL/SES measurement of the F-band in the ”white” Si-ncs/SiO$_2$ sample are presented on two different samples: ”white A” (2.2 mg of Si-ncs ”white” powder) and ”white B” (2 mg of Si-ncs ”white” powder).

Fig. 5.10 shows the two-dimensional map of the VSL/intSES difference as a function of the excitation stripe length and the emission wavelength, measured in the

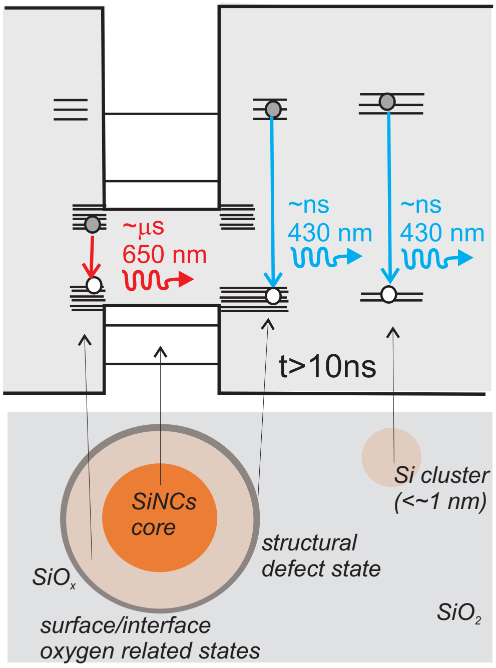

Figure 5.8: *Recombination model of radiative processes (with decay times in the order of ns and µs dominant in the detection window delayed by 10 ns from the excitation pulse (immediately after excitation).*

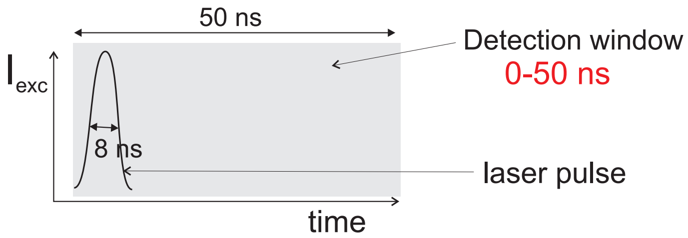

Figure 5.9: *Time sketch of used detection paramaters in subsection 5.4.1.2: detection window of 50 ns coincident with the laser pulse.*

"white A" Si-ncs/SiO$_2$ sample for the excitation densities from 25 kW/cm^2 up to 12.2 MW/cm^2. One should note the different scales of the intensity difference. The VSL/intSES difference is around zero for low excitation densities between 25 kW/cm^2 and 54 kW/cm^2 (Figs. 5.10(a-c)) but it becomes positive for excitation densitites above 54 kW/cm^2 and excitation stripe longer than 3 mm. The high positive value (of the order of 10^4-10^5 in relative units) of the VSL/intSES difference was measured for the excitation densities above 2 MW/cm^2 (Fig. 5.10). The difference peaks at $\sim$ 435 nm, close to the F-band peak maximum.

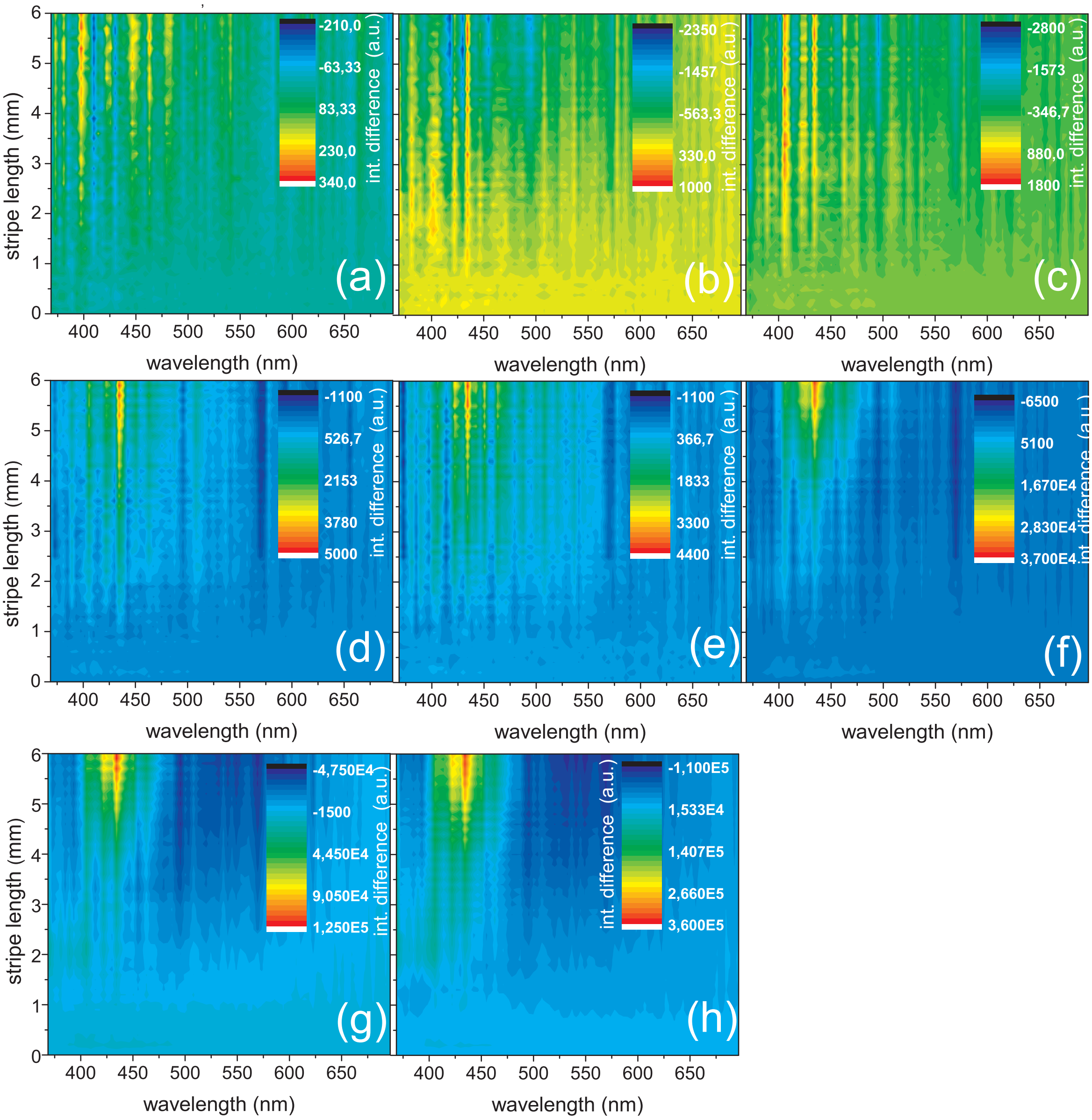

Figure 5.10: *Two-dimensional map of the F-band VSL/intSES difference (Eq. 5.7) of a "white A" Si-ncs/SiO$_2$ sample for excitation densities of (a) 0.02 MW/cm^2, (b) 0.2 MW/cm^2, (c) 0.5 MW/cm^2, (d) 0.8 MW/cm^2, (e) 1.3 MW/cm^2, (f) 2.4 MW/cm^2, (g) 6.7 MW/cm^2, (h) 12.2 MW/cm^2. Note the different intensity scales.*

As an illustration of the VSL and integrated SES curves behaviour we plot the VSL and intSES curves extracted from Figs. 5.10(a-h) at the difference peak maximum ($\sim$ 435 nm) in Fig. 5.11. We can see that for shorter excitation stripe lengths (less than 2 mm) the VSL and intSES curves are similar on all panels. For longer excitation stripes (more than 2 mm), however, the VSL curves either copy the intSES curves (Figs. 5.11(a-b)) or exceed them (Figs. 5.11(d-h)).

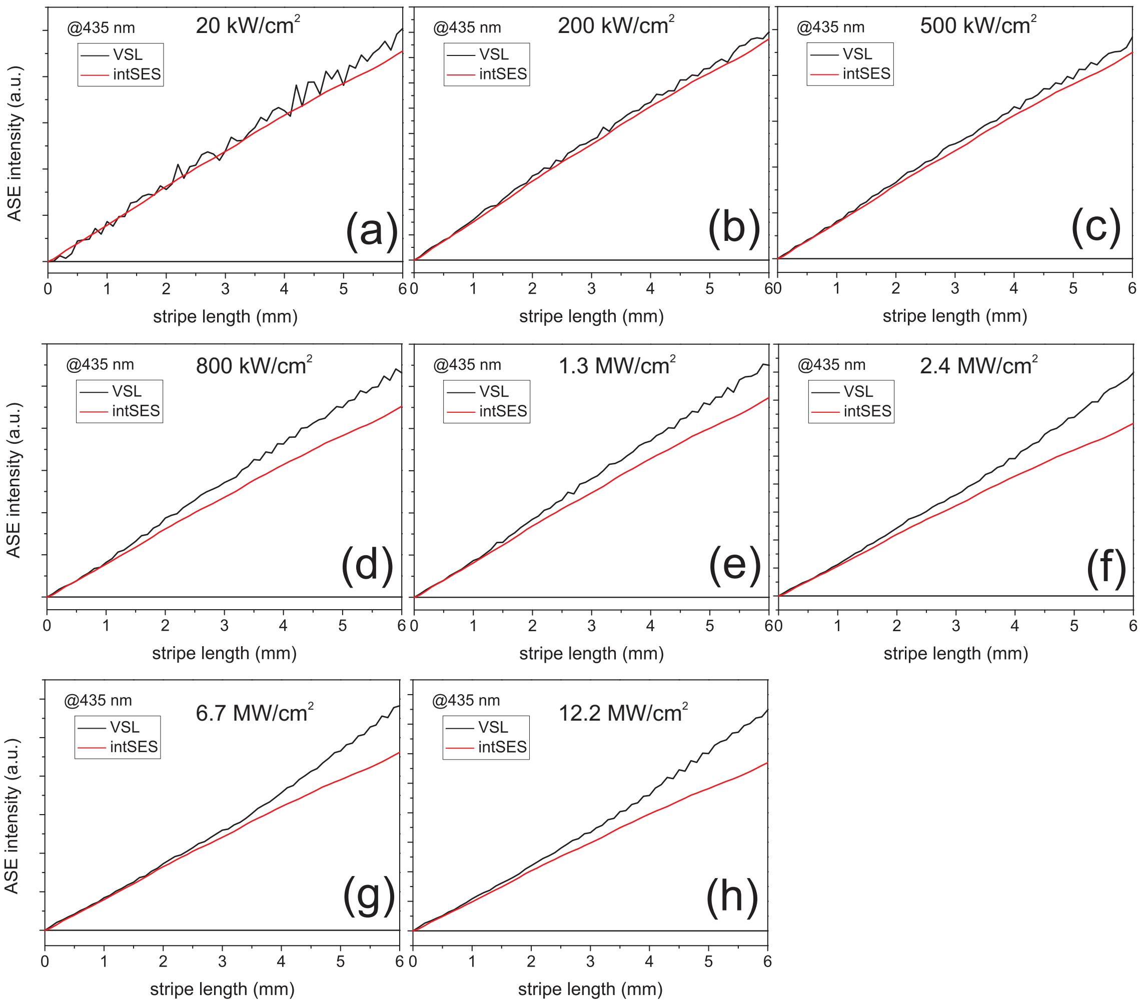

Figure 5.11: *The VSL (black line) and integrated SES (red line) curves, extracted from Figs. 5.10(a-h) at emission wavelength of 435 nm in the "white A" sample for excitation densities of (a) 0.02 MW/cm^2, (b) 0.2 MW/cm^2, (c) 0.5 MW/cm^2, (d) 0.8 MW/cm^2, (e) 1.3 MW/cm^2, (f) 2.4 MW/cm^2, (g) 6.7 MW/cm^2, (h) 12.2 MW/cm^2.*

The difference between VSL and integrated SES spectra is plotted using a fixed intensity scale in Figs. 5.12(a-c) for three different excitation densities. We can clearly see the development of the positive VSL/intSES difference with increasing excitation density. The two-dimensional maps of the ASE spectra (measured for the same three excitation densities) as a function of the stripe length are plotted in Figs. 5.12(d-f) and normalized in Figs. 5.12(g-i). For the lowest excitation intensity, the ASE spectra peak at $\sim$ 430 nm and do not exhibit any spectral changes with the stripe length. On the other hand, the ASE spectra measured at the highest excitation density get considerably narrower with increasing stripe length.

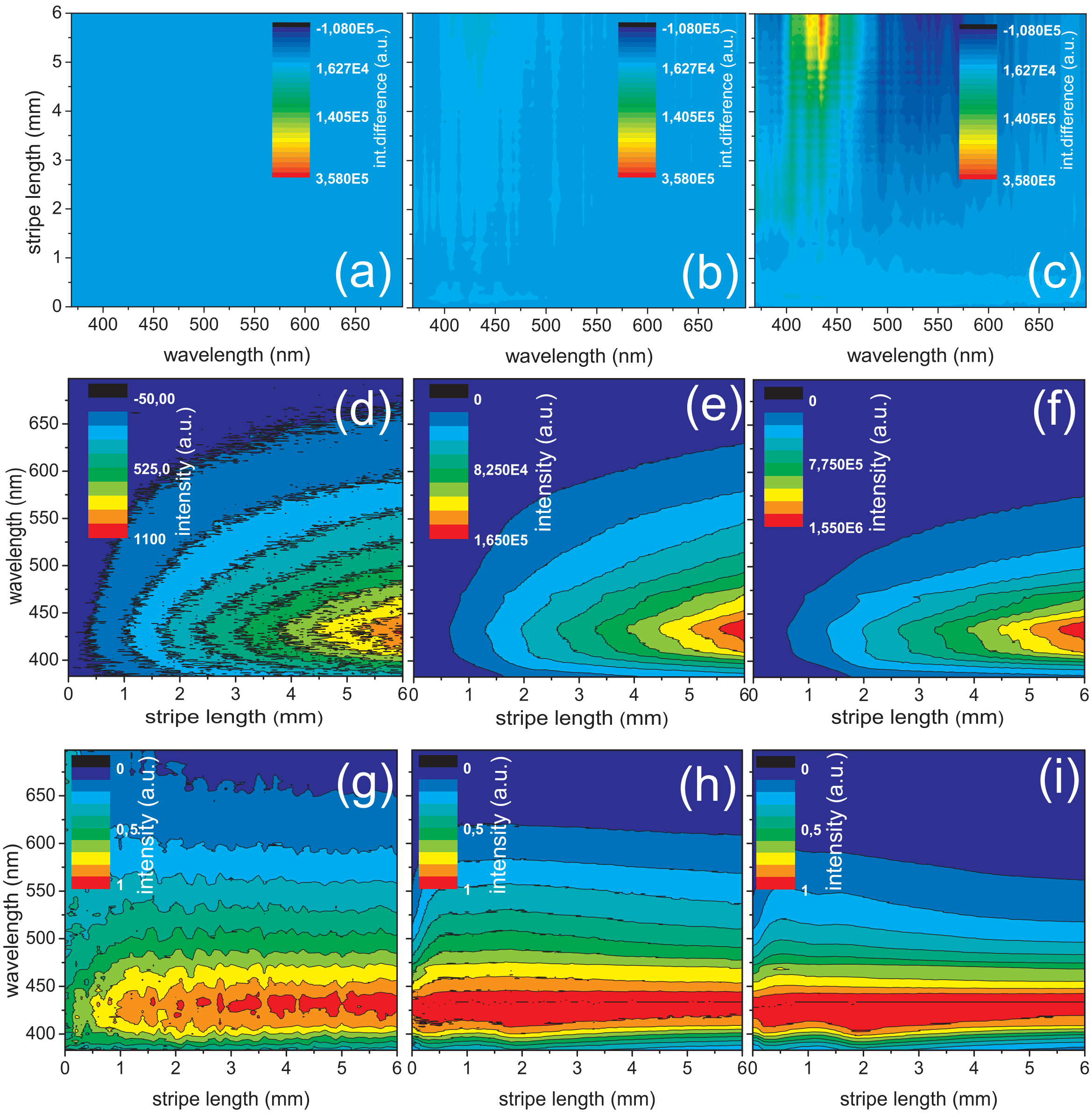

Figure 5.12: *(a-c) Two-dimensional maps of the F-band VSL/intSES difference of the "white A" Si-ncs/SiO$_2$ sample for excitation densities of (a) 0.02 MW/cm^2, (b) 2.4 MW/cm^2, (c) 12.2 MW/cm^2. The intensity scale is fixed in all graphs to show the StE onset with increasing the excitation density. (d-f) ASE spectra (normalized in (g-i)) measured for the same excitation densities.*

The F-band emission spectra (detection window of 0-50 ns) of the "white A" Si-ncs/SiO$_2$ sample for a 6 mm long stripe as a function of the pump density are plotted in Fig. 5.13.

In the inset of Fig. 5.13(b) are plotted the dependencies of the ASE intensity on excitation density in the log-log scale, taken at 435 nm and 467 nm. They show a saturation behaviour for the lower pump densities (≤ 1 MW/cm^2), followed by a superlinear behaviour (superlinear slope of ~ 1.71 at 435 nm and of ~ 1.61 at 467 nm) for higher excitation densities. The superlinear behaviour can be considered as an

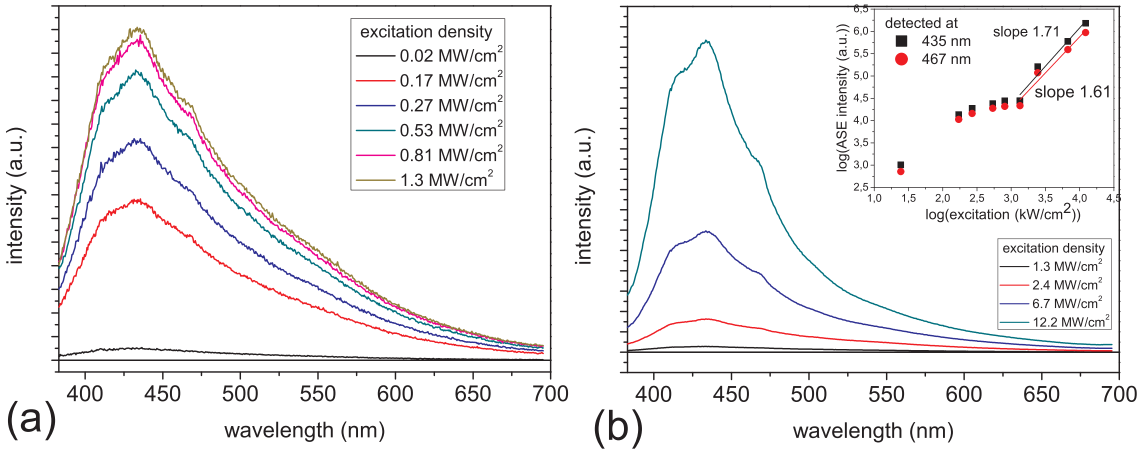

Figure 5.13: *F-band component ASE spectra taken for a 6 mm long stripe in the "white A" Si-ncs/SiO$_2$ sample as a function of the pump density - (a) from 0.02 to 1.3 MW/cm^2; (b) from 1.3 to 12.2 MW/cm^2. Signal was detected with the gate width of 50 ns, coincident with laser pulse. Inset: Dependence of the ASE output intensity on the excitation density in the log-log scale, taken at 435 nm and 467 nm.*

evidence of the StE onset which can develop in the active material for the excitation density exceeding the threshold limit. Interpretation of the saturation and superlinear behaviour will be proposed later in this chapter where we present a tentative model of involved recombination processes. It may be important to note here that a similar behaviour of the output-input intensity dependence was observed by Luterová et al. in [44] in different samples measured by a different setup.

The narrowing of the ASE spectra, the positive VSL/intSES difference and the superlinear ouput-input intensity dependence above a threshold excitation density are good evidence for the StE onset in this "white" Si-ncs/SiO$_2$ sample.

Very similar serie of measurements was done in a different "white" Si-ncs/SiO$_2$ sample (marked as "white B"), which was prepared from 2 mg of Si-ncs powder. A positive VSL/intSES difference as a function of the stripe length and of the emission wavelength is shown in Fig. 5.14 as a two-dimensional map for different excitation densities. We have not excited with the highest density of 12.2 MW/cm^2, as we did in the case of the "white A" Si-ncs/SiO$_2$ sample, because the sample started to burn in the focal plane of the excitation laser pulse.

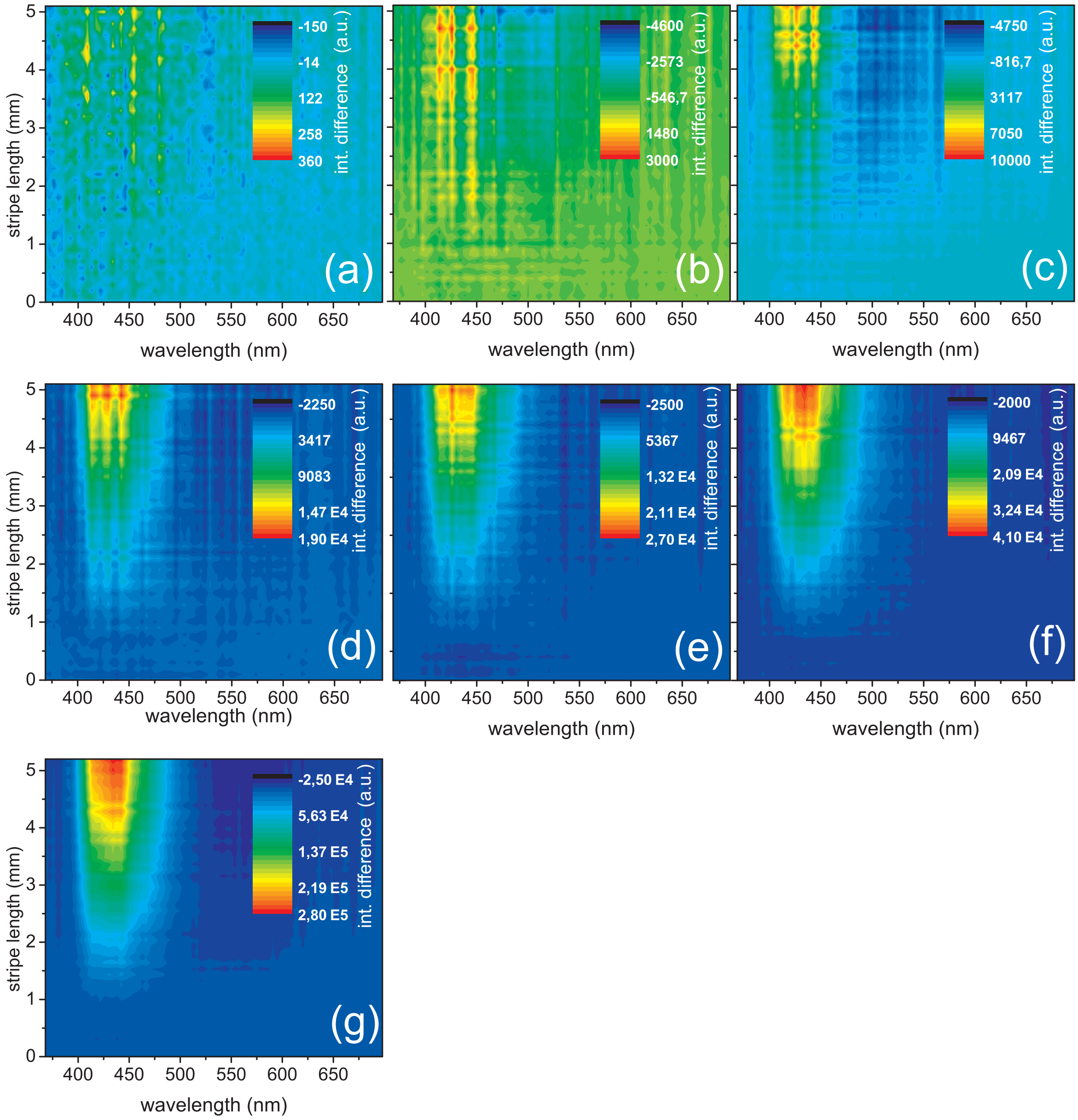

Figure 5.14: *Two-dimensional map of the F-band VSL/intSES difference (Eq. 5.7) of a "white B" Si-ncs/SiO$_2$ sample for excitation densities of (a) 0.02 MW/cm^2, (b) 0.3 MW/cm^2, (c) 0.5 MW/cm^2, (d) 0.8 MW/cm^2, (e) 1.3 MW/cm^2, (f) 2.4 MW/cm^2, (g) 6.7 MW/cm^2. Note the different scales of intensities.*

Comparison of the spectral dependence of the VSL/intSES difference of the "white A" and "white B" Si-ncs/SiO$_2$ samples for the same excitation density of 6.7 MW/cm^2 and for the longest achieved excitation stripe (6 mm for the "white A" and 5.2 mm for the "white B") is plotted in Fig. 5.15(a). We computed also the gain spectrum (Fig. 5.15(b)) from the VSL/intSES difference for the both studied "white" Si-ncs/SiO$_2$ samples using Eq. 5.9. Eq. 5.9 is valid only if the intSES curve is a linear function of the excitation stripe length, which is not exactly fulfilled. Therefore the derived values of the net gain coefficient must be considered only as an approximate estimation. Both graphs show that the "white B" Si-ncs/SiO$_2$ sample had probably better optical properties with a higher net gain coefficient ($\sim$ 24 cm^{-1} at 435 nm) compared with the "white A" one ($\sim$ 20 cm^{-1} at 435 nm), despite the shorter excitation stripe.

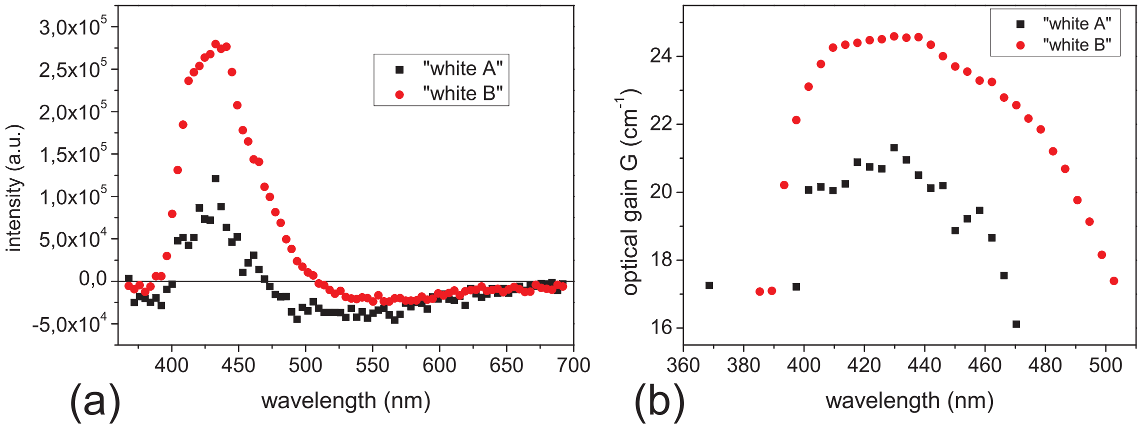

Figure 5.15: *(a) The F-band VSL/intSES difference spectrum and (b) the gain spectrum the of the "white A" and "white B" Si-ncs/SiO$_2$ samples for the excitation density of 6.7 MW/cm^2 and for the longest achieved stripe length of 6 mm ("white A") and 5.2 mm ("white B").*

In Fig. 5.16 we show the VSL and intSES curves separately, extracted at 435 nm from the 2D maps in Fig. 5.14 for similar excitation densities. On the panels (d-g) in Fig. 5.16 it is evident that the VSL and integrated SES curves copy each other for the stripe length shorter than 1 mm, while the VSL curve significantly exceeds the intSES curve for longer stripes. It is a good evidence of the StE onset in the sample.

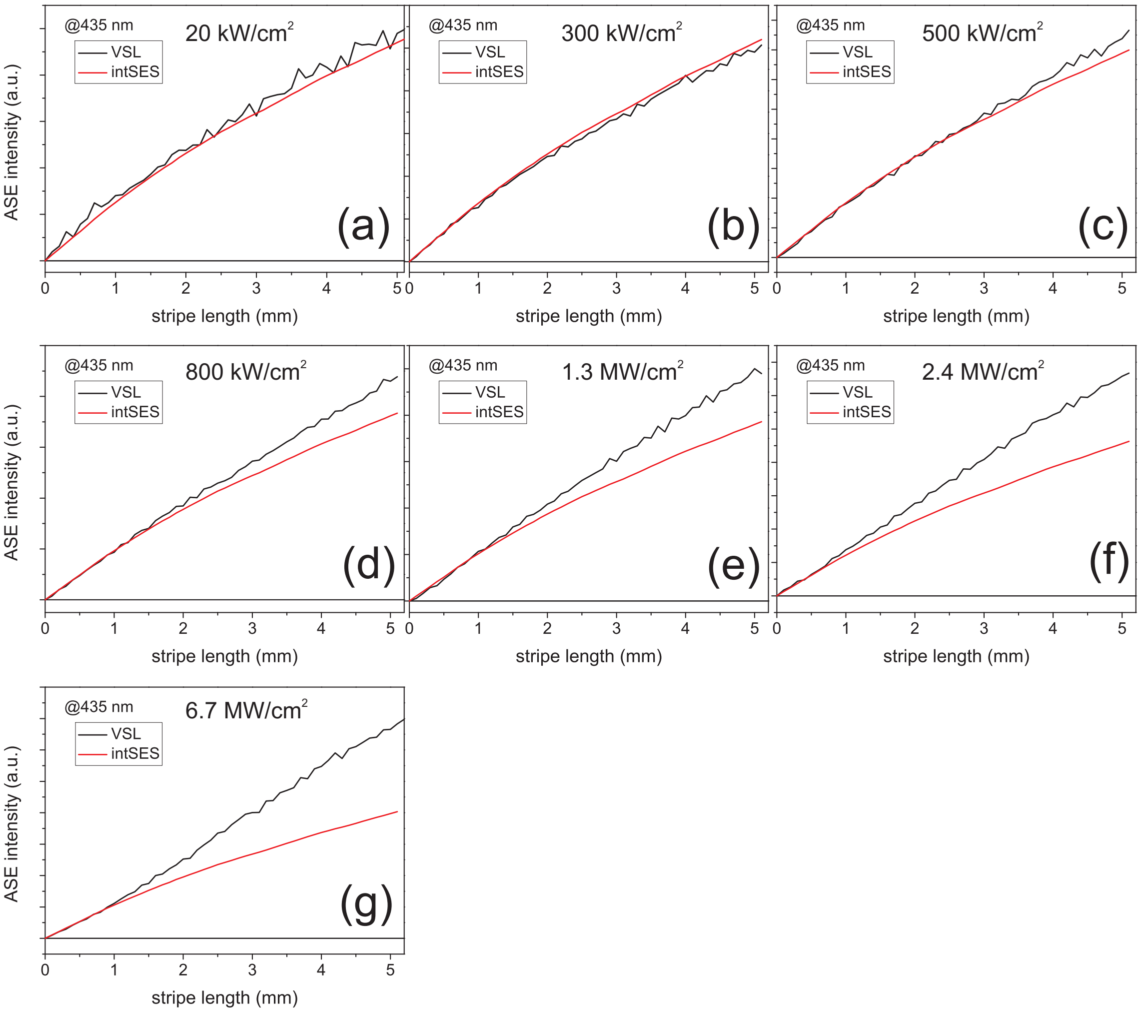

Figure 5.16: *The VSL (black line) and integrated SES (red line) curves, extracted from graphs in Fig. 5.14 at emission wavelength of 435 nm in the "white B" Si-ncs/SiO$_2$ sample for excitation densities of (a) 0.02 MW/cm^2, (b) 0.3 MW/cm^2, (c) 0.5 MW/cm^2, (d) 0.8 MW/cm^2, (e) 1.3 MW/cm^2, (f) 2.4 MW/cm^2, (g) 6.7 MW/cm^2.*

Finally, we present the two-dimensinal maps (with the fixed scale of intensity difference) of the VSL/intSES difference of the "white B" sample for three different excitation densities (Figs. 5.17(a-c)). Further we show the the two-dimensional maps of the ASE spectra (measured for the same three excitation densities) as a function of the stripe length in Figs. 5.17(d-f) and normalized in Figs. 5.17(g-i). We can see a significant narrowing of the spectra with the excitation stripe length for the excitation density of 6.7 MW/cm^2 (Fig. 5.17(i)), being an evidence of the StE onset.

We can conclude that for the both "white" Si-ncs/SiO$_2$ samples the StE onset at the F-band emission component was observed.

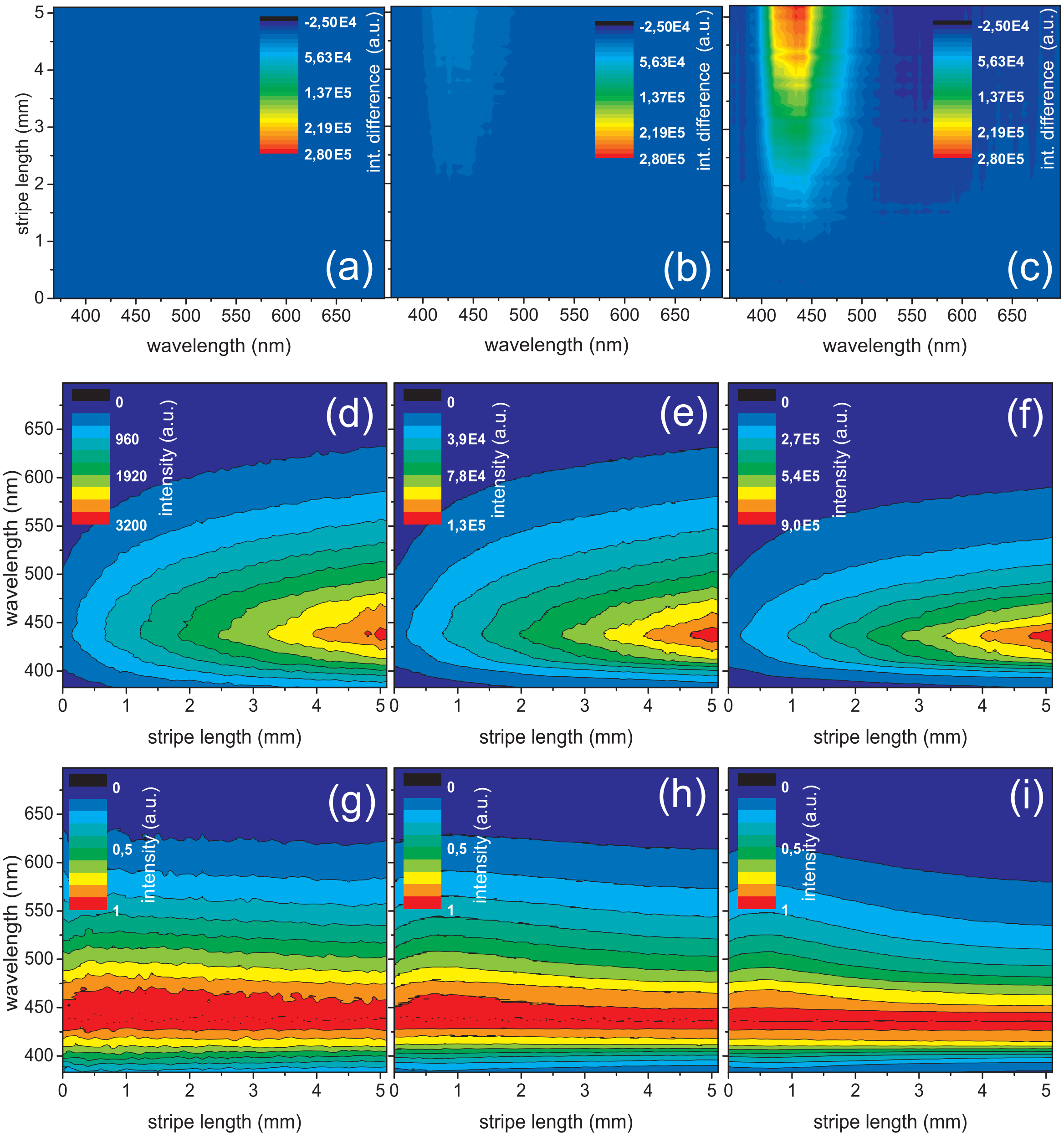

Figure 5.17: *(a-c) Two-dimensional maps of the F-band VSL/intSES difference measured in the "white B" Si-ncs/SiO$_2$ sample for excitation densities of (a) 0.02 MW/cm^2, (b) 1.3 MW/cm^2, (c) 6.7 MW/cm^2. The intensity scale is fixed in all graphs to show the StE onset with increasing excitation density. (d-f) ASE spectra (normalized in (g-i)) for the three excitation densities as in (a-b).*

"Yellow" Si-ncs/SiO$_2$ sample

We studied the possibility of the presence of positive optical gain at the F-band component also in the "yellow" Si-ncs/SiO$_2$ sample. Results of the VSL/SES measurements are summarized in Fig. 5.18. Figs. 5.18(a-c) show two-dimensional maps of the VSL/intSES difference for three different excitation densities whereas in Figs. 5.18(d-f) we plot the extracted VSL and intSES curves at 435 nm.

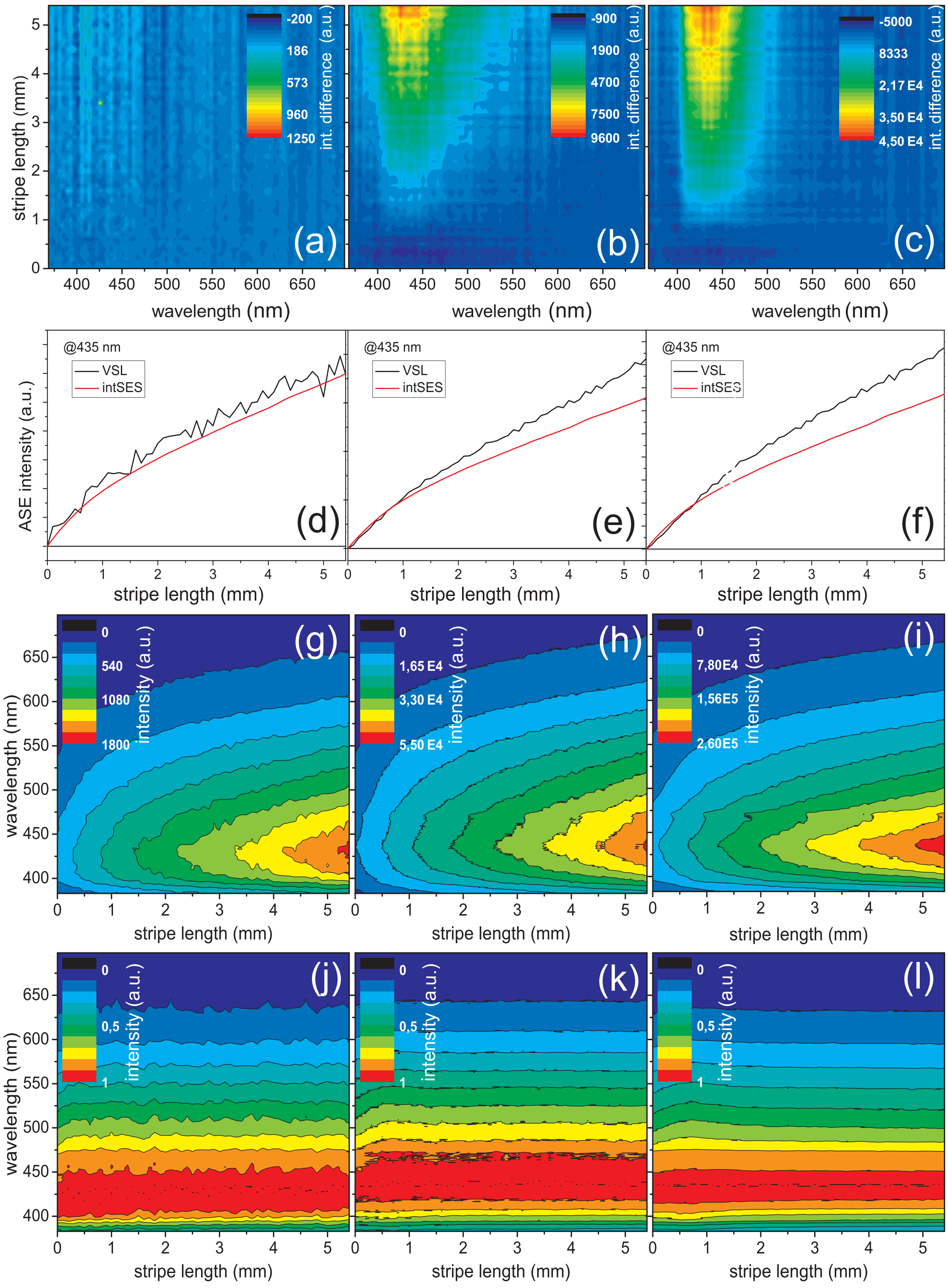

Figure 5.18: *(a-c) Two-dimensional maps of the F-band VSL/intSES difference of the "yellow" Si-ncs/SiO$_2$ sample for excitation densities of (a) 0.02 MW/cm^2, (b) 1.3 MW/cm^2, (c) 6.7 MW/cm^2. Note the different intensity scales. (d-f) The VSL (black line) and integrated SES (red line) curves, exctracted from (a-b) at emission wavelength of 435 nm (ASE intensity peak maximum). (g-i) ASE spectra (normalized in (g-i)) for three excitation densities as in (a-b).*

We observed a positive VSL/intSES difference above a certain value of the stripe length and excitation density, which can be an evidence of the StE onset. Here, we would like to point out that the VSL/intSES difference in the "yellow" sample is by one order of magnitude lower than in case of the "white" sample (for comparison, see for example Fig. 5.14(g) and Fig. 5.18(c)). This is something that we would expect because of the higher intensity of the F-band in the "white" Si-ncs/SiO$_2$ sample compared to the "yellow" one, observed in the time-integrated PL spectra in Fig. 4.14. ASE spectra measured for the excitation densities as in (a-c) are shown in Figs. 5.18(g-i) (normalized in Figs. 5.18(j-l)). Narrowing of the ASE spectra with increasing stripe length and excitation density is less evident than in the "white" sample.

Model of recombination processes in the detection window of 0-50 ns

Radiative recombination processes which are in progress within the detection window of 0-50 ns are shown in Fig. 5.8. Based on the results of the PL emission measurements in section 4.2, we propose that the dominant process is the radiative recombination at 435 nm which can be explained as either recombinations in some structural defects in the Si-ncs oxide shell [32] and/or as an intrinsic core-related emission from small Si-ncs ($\sim$ 1 nm core diameter)[31][33][34]. The oxygen related Si-ncs surface/interface states are more intensively involved in the S-band emission with the μs decay time. Now they act more as a storage level of the excited carriers (metastable states) which leads to depopulation of the ground state. This explanation is well-founded by the saturation behaviour of the output-input intensity dependence which may be interpreted in terms of a selective saturation of the absorption as observed in the porous silicon [45]. If we assume that the F-band and the S-band share the common ground state then filling of the metastable state may lead to the inversion of the population followed by stimulated emission at the F-band. The condition of the shared ground state can be achieved by the states that are connected or close enough to the Si-ncs surface, where the metastable states are located. Then only the defects close and/or connected to the Si-ncs surface become active in the StE onset. On the other hand, defect states being located far from the Si-ncs, i.e. having separated ground state, may not be possibly able to reach the population inversion condition. The close interaction with the Si-ncs could in this model enable switching the matrix defects from the "StE inactive" to "StE active" ones by sharing the ground state which is depopulated via the metastable Si-ncs surface states.

However, the origin of the F-band StE onset might be also related to the emission from the ultrasmall Si-ncs, where the metastable state S-band emission was also observed [31]. In such a case, the radiative recombination takes place between the excited and the ground core-related states and the metastable state may be the surface/interface oxygen-related state of the small Si-ncs.

We may conclude that the presence of the metastable state, leading to the S-band emission component which decays in μs scale, may be critical for the StE onset achievement. The StE onset from the F-band may originate in both - the defect related states and/or the small Si clusters core-related states, however, the presence of the oxygen-related states is required. This is in good agreement with Chen et al. [17] claiming that the optical gain may be critically dependent on the oxide presence in the sample. However, we assume, contrary to Chen at al., that the optical gain may originate from both - the core-related (intrinsic) and surface related (extrinsic) states and that it is only the shared ground state with the oxygen related state, which is required.

5.4.2 Gain measurements on the S-band emission component

Positive optical gain that has an origin in the S-band emission component peaked at 600 - 800 nm was reported by several research groups [4][46][47] [48]. Therefore we focused also our attention on the S-band emission component of our samples, which we have studied in two detection gate windows - (i) [0.2 - 100 μs], delayed with respect to the excitation pulse in order to study the S-band separately from the F-band and (ii) [0 - 100 μs], coincident with the excitation pulse, including both the F and S-band. We performed series of the VSL/SES measurements, some of them brought positive and some of them "zero" VSL/intSES difference. For the sake of clarity, we will mainly focus on the results with the positive difference but one of the "zero" difference will be presented in the last subsection also.

5.4.2.1 Detection gate window of 0.2 - 100 μs

The gate delay of 200 ns (with respect to the excitation pulse) was set in order to exclude the intense F-band component. The detection gate width of 100 μs was used for the detection (see Fig. 5.19). The "white" and "yellow" Si-ncs/SiO$_2$ samples are presented separately.

"White" Si-ncs/SiO$_2$ samples

In this subsection, the "white B" Si-ncs/SiO$_2$ sample is studied; a place on the sample with a relatively good optical quality was choosen for the measurement with the VSL excitation stripe.

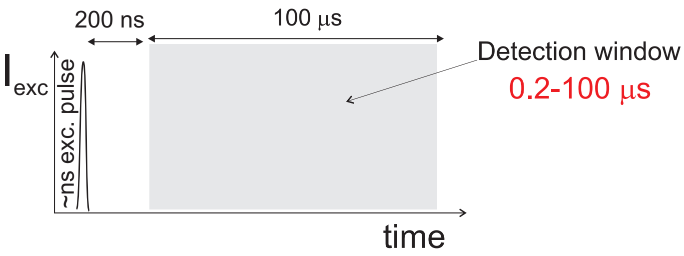

Figure 5.19: *Time sketch of used detection parameters in the subsection 5.4.2.1: detection window of 0.2 - 100 μs.*

Two-dimensional maps of the VSL/intSES difference as a function of the excitation stripe are shown in Fig. 5.20 for excitation densities from 0.02 to 6.7 MW/cm^2. The difference is very low if not zero in (a-b). However, it is interesting to note that a positive difference was reported even for relatively low excitation density of 0.3 MW/cm^2 for the stripe longer than 2 mm. The positive VSL/intSES difference denotes positive optical gain occurrence. The VSL and intSES curves extracted at 600 nm are plotted in Figs. 5.21(a-h). Notice that for the excitation stripe length around 4 mm the VSL and intSES curves show a slight disruption. This might be due to some inhomogenity in the sample - either some scattering center or some matrix imperfections. As we can see, it does not influence the possibility of the StE onset in the sample.

It is interesting to point out a significant blue-shift of the positive VSL/intSES difference with increasing excitation density in Fig. 5.20. Two main features may lead to such a behaviour. Firstly, the absorption edge lowers at lower excitation intensities the gain values. On the other hand, for higher excitation intensities the absorption edge shifts towards shorter wavelengths. Secondly, it is in agreement with generally accepted conception that the Si-ncs emitting in shorter wavelengths would exhibit higher optical gain due to the lower probability of FCA (depleting the population inversion efficiently in larger Si-ncs), and due to a larger oscillator strenght (more efficient PL emission with faster radiative decay).

Another interesting feature comes from a comparison of the PL spectrum, ASE spectrum and the spectral dependence of the VSL/intSES difference of the same "white" Si-ncs/SiO$_2$ sample. The PL spectrum is slightly spectrally blue-shifted with respect to the ASE spectrum, taken for excitation density of 6.7 MW/cm^2 and the stripe length of 5.7 mm (Fig. 5.22(a)). More interesting is the slight red-shift of the spectral dependence of the VSL/intSES difference, compared to the PL spectrum (Fig. 5.22(b)),which might be due to a missing "green" band emission and a low F-band emission in the detection window of 0.2 - 100 μs. Moreover, it might be caused by the missing S-band signal onset below 200 ns after excitation (the detection window

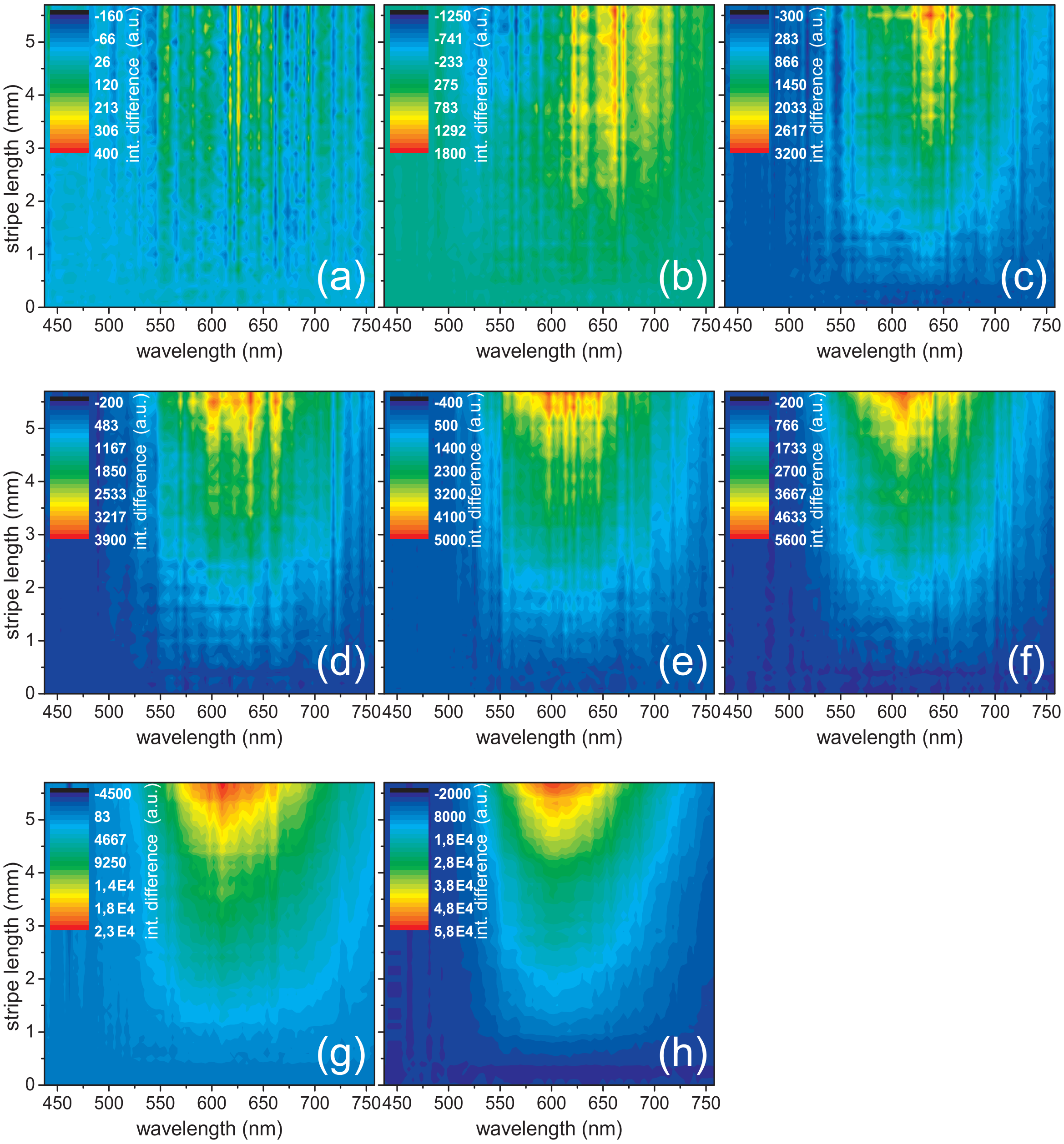

Figure 5.20: *Two-dimensional map of the S-band VSL/intSES difference (Eq. 5.7) of the "white" Si-ncs/SiO$_2$ sample for excitation densities of (a) 0.02 MW/cm^2, (b) 0.2 MW/cm^2, (c) 0.3 MW/cm^2, (d) 0.5 MW/cm^2, (e) 0.8 MW/cm^2, (f) 1.3 MW/cm^2, (g) 2.4 MW/cm^2, (h) 6.7 MW/cm^2. Note the different scales.*

of 0.2 - 100 μs).

Finally, in Figs. 5.23(a-c) we present the two-dimensional maps of the VSL/intSES difference (taken from Fig. 5.20) for three excitation densities. Scale of the intensity difference is fixed in all graphs in order to emphasize the StE onset with increasing pumping intensity. ASE spectra for the excitation densities as in (a-c) are plotted in Figs. 5.23(d-f) and normalized in Figs. 5.23(g-i). Narrowing of the ASE spectra with increasing excitation density and stripe length is not expressive. This may be due to the inhomogeneous broadening of the S-band.

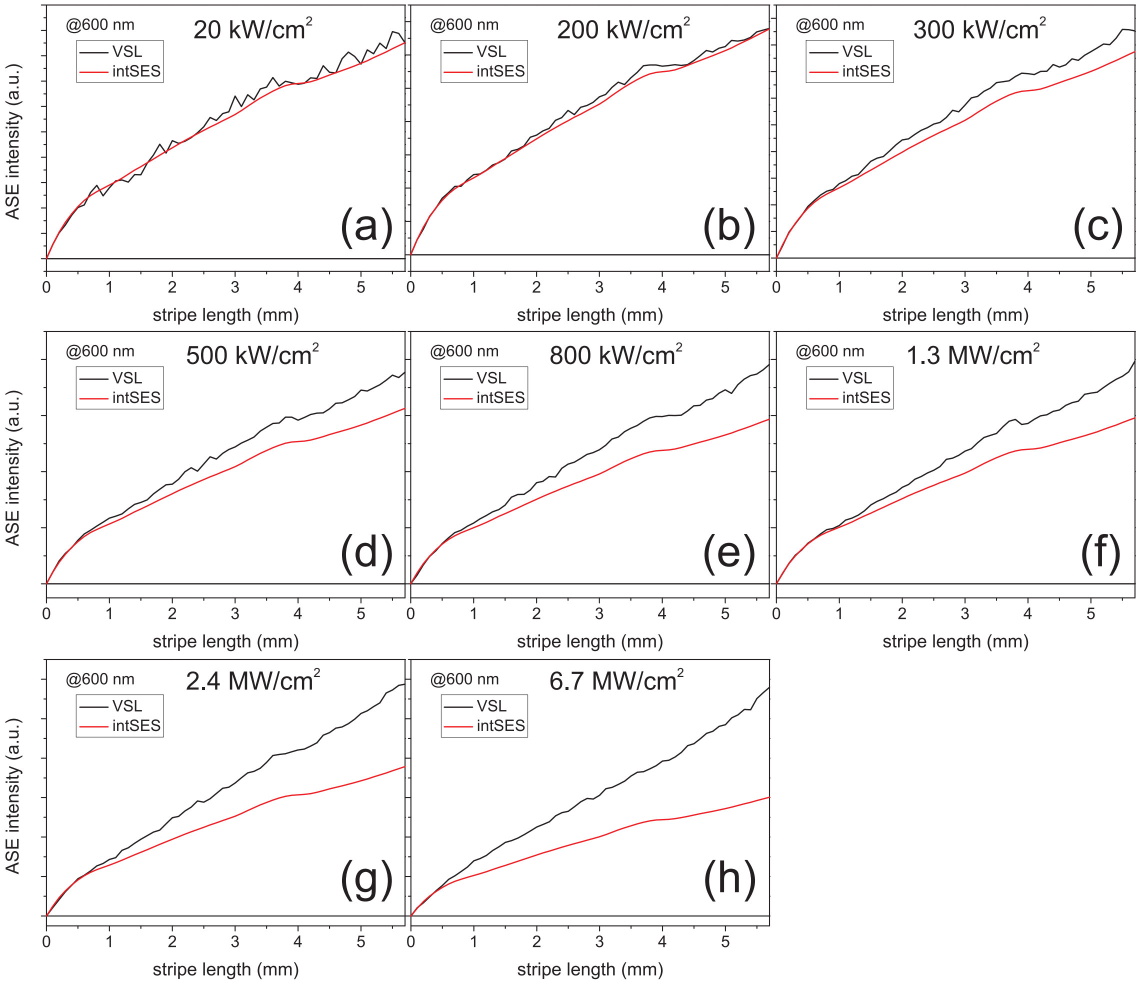

Figure 5.21: *The VSL (black line) and integrated SES (red line) curves, extracted from graphs in Fig. 5.20 at emission wavelength of 600 nm of the "white" Si-ncs/SiO$_2$ sample for excitation densities of (a) 0.02 MW/cm^2, (b) 0.2 MW/cm^2, (c) 0.3 MW/cm^2, (d) 0.5 MW/cm^2, (e) 0.8 MW/cm^2, (f) 1.3 MW/cm^2, (g) 2.4 MW/cm^2, (h) 6.7 MW/cm^2.*

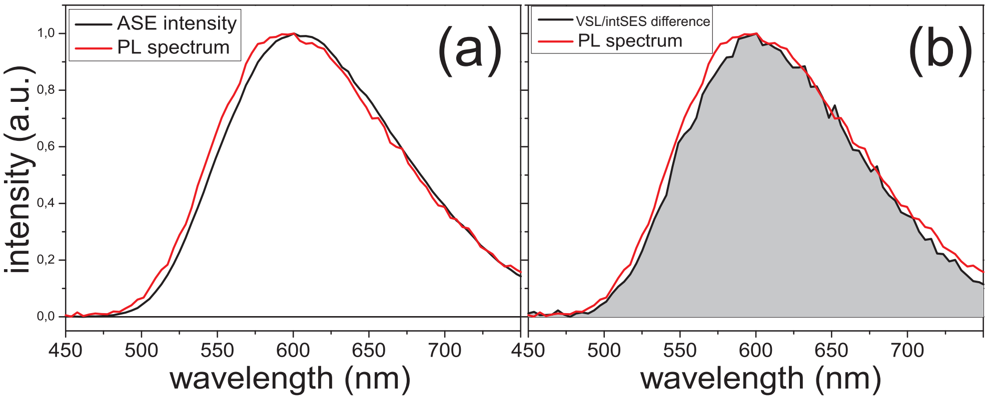

Figure 5.22: *Comparison of the PL and either (a) ASE spectrum or (b) VSL/intSES difference spectrum of the "white" Si-ncs/SiO$_2$ sample taken for excitation density of 6.7 MW/cm^2 and the stripe length of 5.7 mm.*

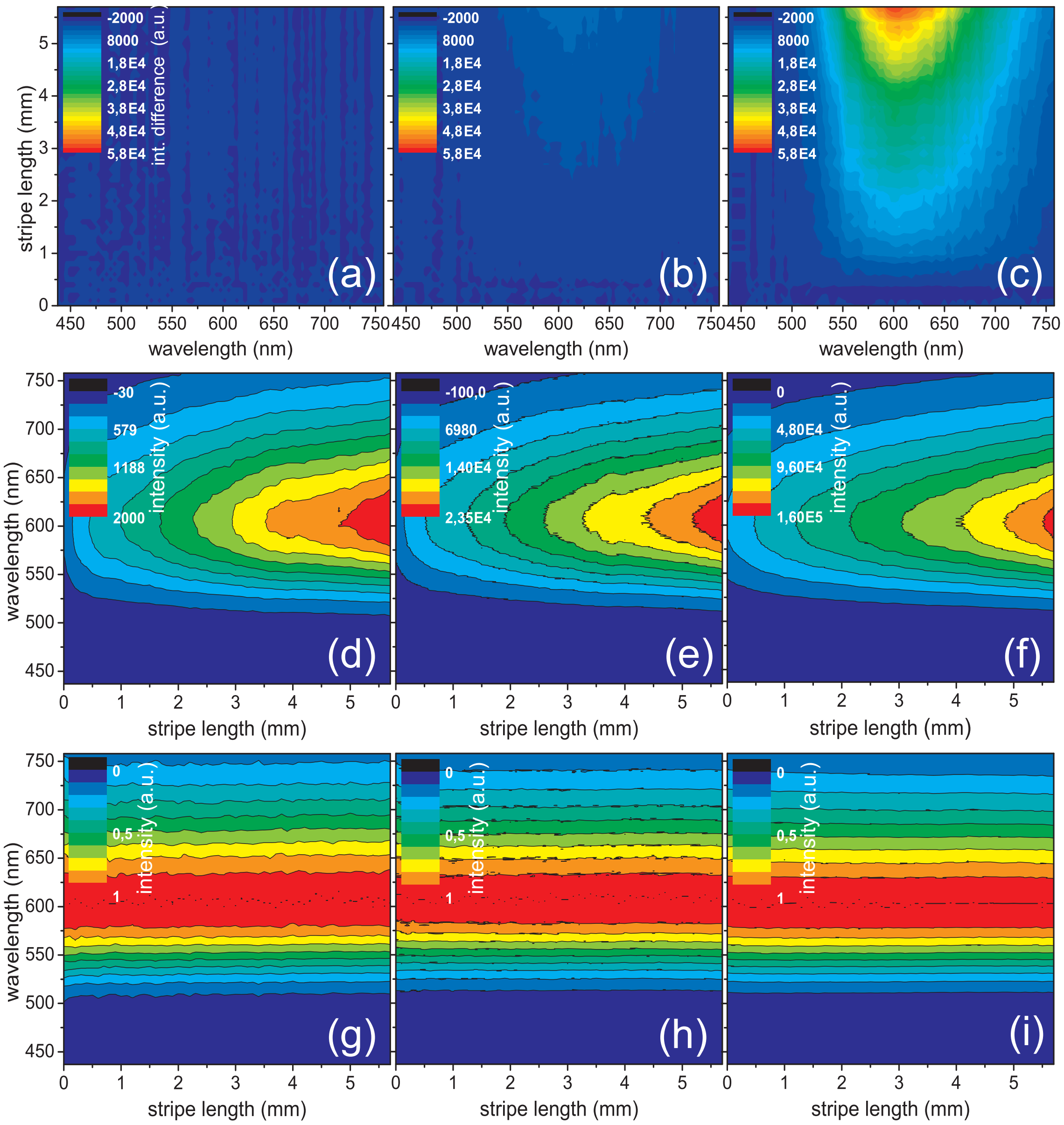

Figure 5.23: *(a-c) Two-dimensional maps of the S-band VSL/intSES difference of the "white" Si-ncs/SiO$_2$ sample for excitation densities of (a) 0.02 MW/cm^2, (b) 1.3 MW/cm^2 and (c) 6.7 MW/cm^2. The scale is fixed in all graphs to show the StE onset with increasing excitation density. (d-f) ASE spectra (normalized in (g-i)) for three excitation densities as in (a-b).*

The time-integrated spectra of the S-band component, presented for the "white" Si-ncs/SiO$_2$ sample in Fig. 5.24(a), were obtained with the 500 ns gate delay with respect to the excitation pulse (to avoid the F-band component) and gate width of 100 μs. In Fig. 5.24(b) we plot the dependence of the output intensity on the excitation density in the log-log scale at an emission wavelength of 600 nm. Similarly to the F-band component, saturation of the output intensity is followed by a threshold onset beyond which the ouput intensity shows superlinear behaviour with the slope of $\sim$ 1.11. Considering the superlinear behaviour and the positive VSL/intSES differ-

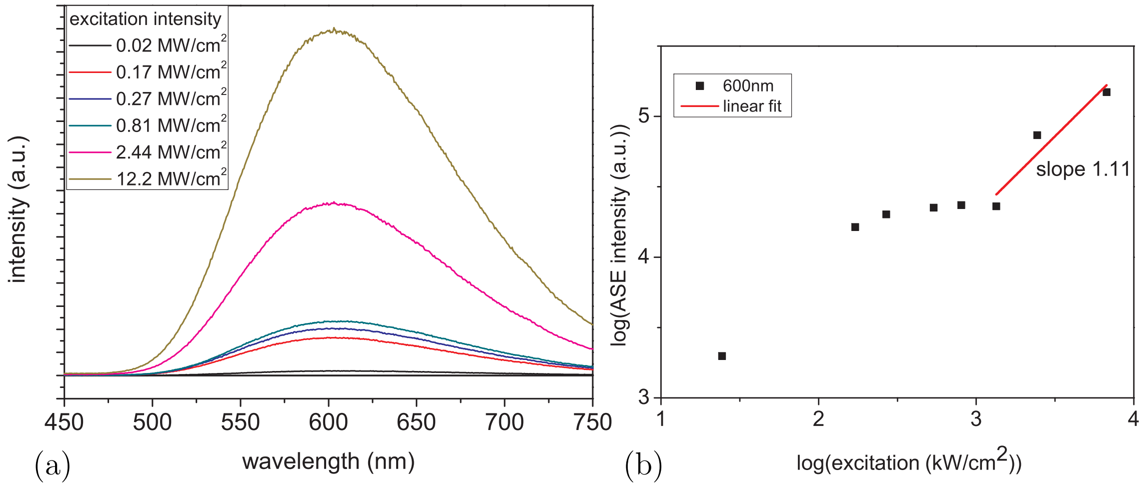

Figure 5.24: *(a) S-band ASE emission spectra of the "white" Si-ncs/SiO$_2$ sample as a function of the excitation density for the stripe length of 5.7 mm. Signal was detected with the gate delay of 500 ns and the gate width of 100 μs. (b) The dependence of the output intensity on the excitation density in the log-log scale at 600 nm.*

ence, we can expect that the positive optical gain might be obtained from the S-band component.

Model of recombination processes in the detection window of 0.2 - 100 μs

We propose that the dominant radiative channel in the detection window of 0.2 - 100 μs originates from the radiative recombination of the carriers from the oxygen-related Si-ncs surface/interface states (Fig. 5.8(red line)). As we have already mentioned, these Si-ncs surface/interface states are involved in the S-band emission and act as the metastable states with μs decay. For high pumping densities and longer VSL stripes, the population inversion between the metastable and ground state can be established which is the necessary (but not sufficient) condition for StE onset. We pressume that probability of the non-radiative Auger recombination (that might deplete the excited energy level) is relatively low because of the spatial separation of carriers trapped in the Si-ncs surface states [13]. Moreover, as we mentioned earlier, the carriers trapping in the surface states in our system appears to be unusually fast, occuring within first ∼ 400 fs after excitation [43].

"Yellow" Si-ncs/SiO$_2$ samples

Experimental results measured in the "yellow" Si-ncs/SiO$_2$ sample are summarized in Fig. 5.25. Panels (a-c) show two-dimensional maps of the VSL/intSES difference for three different excitation densities. Maximal positive difference measured for the excitation density of 6.7 MW/cm^2 in the "yellow" Si-ncs/SiO$_2$ sample is by one order of magnitude higher compared to the difference of the "white" sample excited by a similar intensity (compare Figs. 5.25(c) and 5.23(c)). Figs. 5.25(g-i) display the ASE spectra (normalized in (j-l)) as a function of the excitation stripe length for the same excitation densities as in (a-c).

Comparison of the PL and ASE spectrum is plotted in Fig. 5.26(a). The ASE spectrum was taken with an excitation density of 6.7 MW/cm^2 and the stripe length of 4.9 mm. Spectral dependence of the VSL/intSES difference obtained with the same parameters as the ASE spectrum is plotted in Fig. 5.26(b) in comparison with the PL spectrum and in Fig. 5.26(c) in comparison with the ASE spectrum. The VSL/intSES difference spectrum peaks at $\sim$ 620 nm and is slightly spectrally red-shifted compared to the PL spectrum. We have reported the same phenomenon for the ”white” sample, interpreted as to be due to the missing ”green” and F-band contribution, and due to the missing S-band beginning by the detection gate delay.

In conclusion - we observed positive VSL/intSES difference from the S-band separately that might be a good evidence of the StE onset and positive optical gain in our samples. However, no narrowing of the ASE spectra (or a very small one only) was observed, presumably due to the inhomogeneous S-band broadening and low optical gain coefficient.

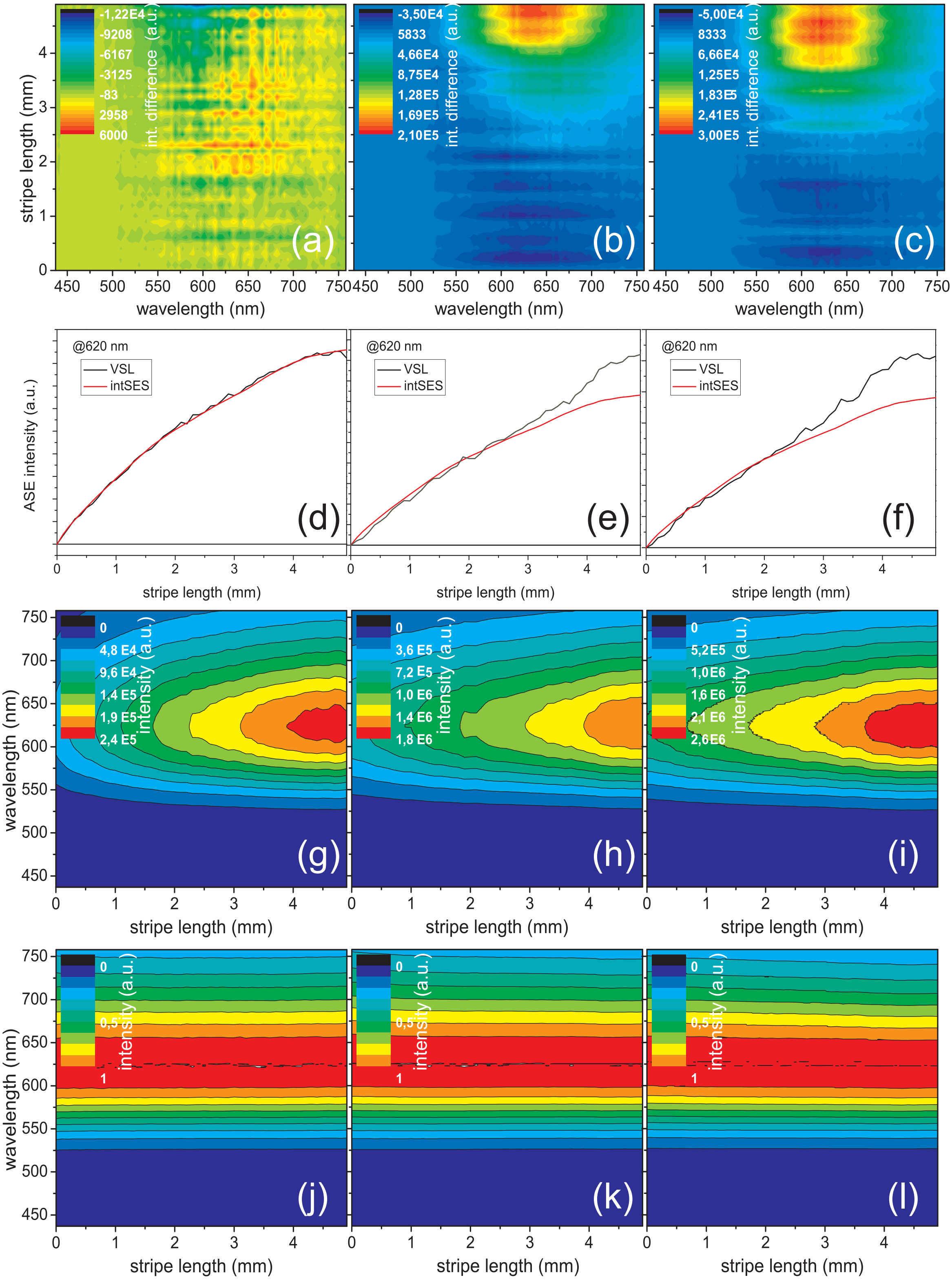

Figure 5.25: *(a-c) Two-dimensional maps of the S-band VSL/intSES difference of the "yellow" Si-ncs/SiO$_2$ sample for excitation densities of (a) 0.3 MW/cm^2, (b) 6.7 MW/cm^2 and (c) 12.2 MW/cm^2. Note the different intensity scales. (d-f) The VSL (black line) and integrated SES (red line) curves, taken from (a-c) at emission wavelength of 620 nm (ASE peak maximum). (g-i)ASE spectra (normalized in (j-l)) for three excitation densities as in (a-b).*

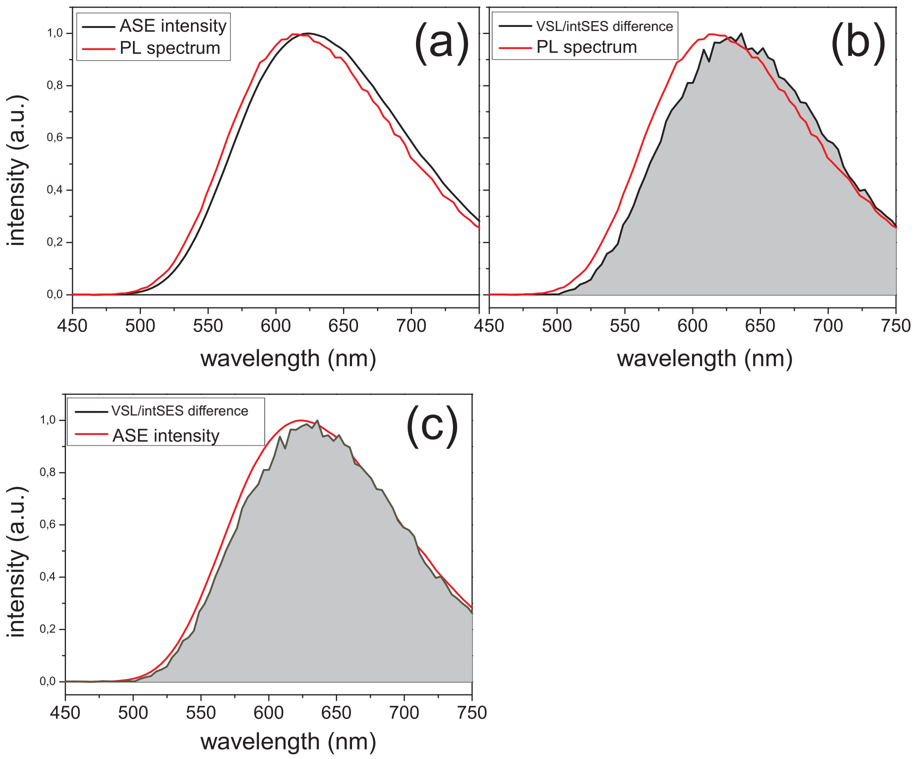

Figure 5.26: *Comparison of (a) the PL and ASE spectrum, (b) the PL and VSL/intSES difference spectrum and (c) the ASE and VSL/intSES difference spectrum in the "yellow" Si-ncs/SiO$_2$ sample. ASE and VSL/intSES difference spectrum was taken for excitation density of 6.7 MW/cm^2 and the stripe length of 4.9 mm.*

5.4.2.2 Detection gate window of 0 - 100 μs

In the last subsection of this chapter, we focuse our attention on the detection window of 0 - 100 μs. It should cover both the F-band and S-band emission together. We performed a huge serie of measurement, however, due to a limited space of this thesis we will present only two of them, done in the "white" and "yellow" Si-ncs/SiO$_2$ samples.

Fig. 5.27(a) shows the two-dimensional map of the VSL/intSES difference in the "white" Si-ncs/SiO$_2$ sample for the excitation density of 1.3 MW/cm^2. VSL and intSES curves extracted at 610 nm are plotted separately in inset. StE was not present in the excited area of the sample because the difference is very low or nearly zero. Probably the excited area was not homogeneous or damaged. Figs. 5.27(b-c) show ASE and normalized ASE spectra for the same excitation density as in (a). Both emission bands (F-band and S-band) are present in this sample, however, no StE onset was achieved for any of them. The dependence of the output intensity on the excitation density in the log-log scale is nearly linear for lower excitation densities and saturates for higher excitation densities (Fig. 5.27(d)). The saturation is not

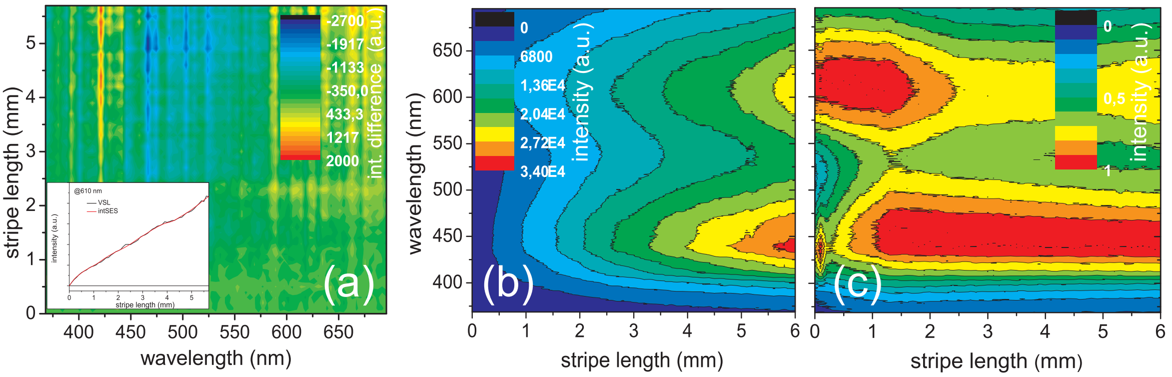

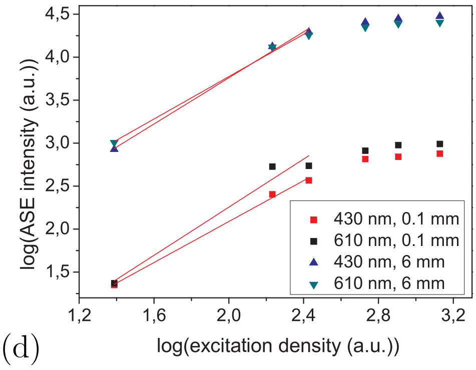

detection wavelength	stripe length	slope
430 nm	0.1 mm	1.19
610 nm	0.1 mm	1.40
430 nm	6 mm	1.34
610 nm	6 mm	1.23

Figure 5.27: *(a) Two-dimenstional map of the F and S-band VSL/intSES difference for the excitation density of 1.3 MW/cm^2 of the "white" Si-ncs/SiO$_2$ sample. (b) ASE spectra (normalized in (c) for the same excitation density as in (a). (d) Dependence of the output intensity on the excitation density in log-log scale for the stripe length of 0.1 and 6 mm, and for emission wavelengths of 430 and 610 nm.*

emission wavelength and/or stripe length dependent and it is present probably due to saturation of absorption and/or the Auger effect.

On the contrary, the VSL/SES measurement realized in the "yellow" Si-ncs/SiO$_2$ sample brought us an evidence of the optical gain on the S-band. Nearly zero VSL/intSES difference is found for low excitation densities (Fig. 5.28(a)) but the difference is clearly positive for longer excitation stripes and higher excitation densities (Figs. 5.28(b-f)), which denotes the StE onset in the sample. The VSL and intSES curves extracted from (a-f) at 620 nm (emission peak) are shown in Figs. 5.28(g-l).

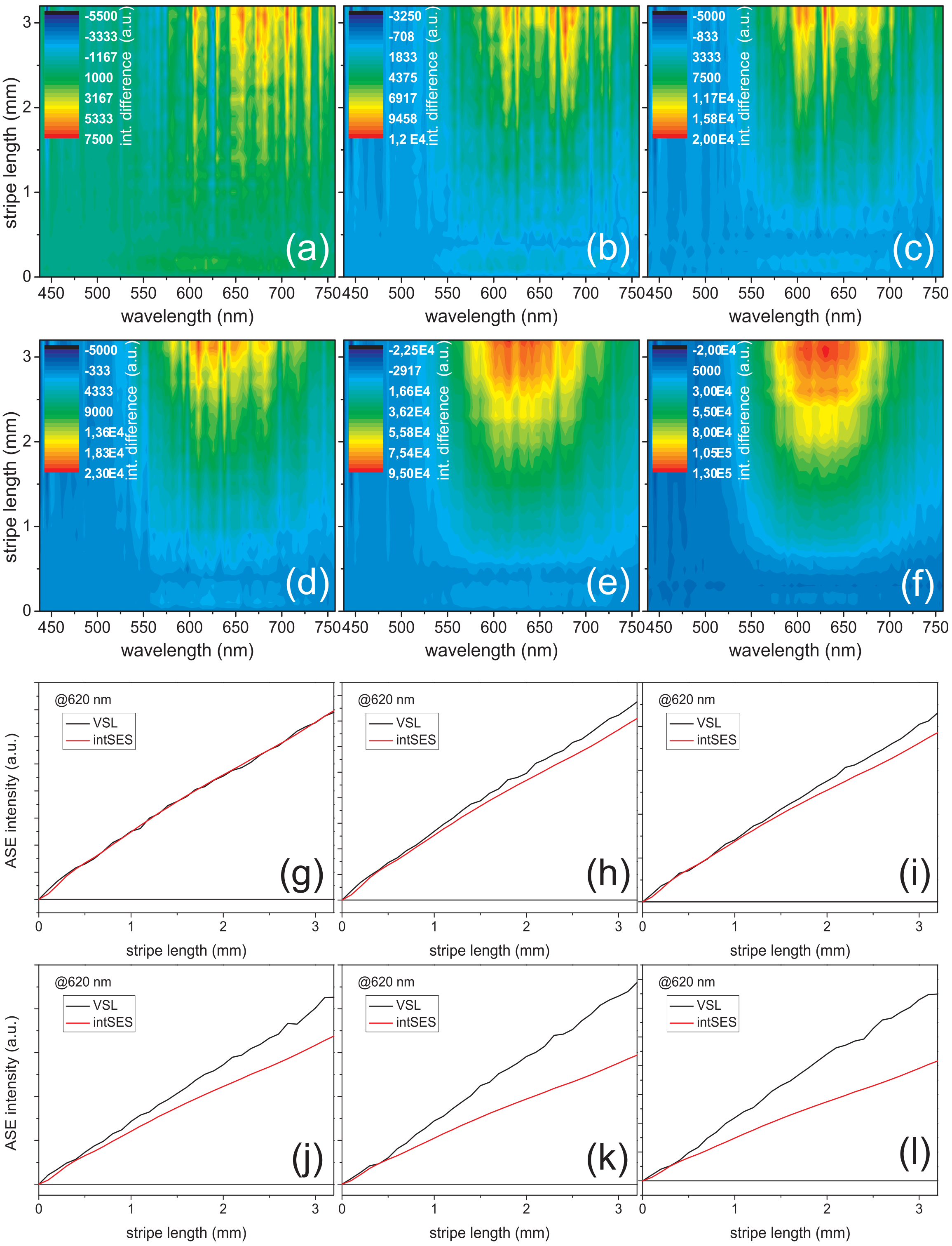

Figure 5.28: *(a-f) Two-dimensional maps of the F and S-band VSL/intSES difference (Eq. 5.7) of the "yellow" Si-ncs/SiO$_2$ sample for excitation densities of (a) 0.5 MW/cm^2, (b) 0.8 MW/cm^2, (c) 1.3 MW/cm^2, (d) 2.4 MW/cm^2, (e) 6.7 MW/cm^2, (f) 12.2 MW/cm^2. (g-l) The VSL (black line) and integrated SES (red line) curves extracted from (a-f) at emission wavelength of 620 nm (ASE spectrum peak maximum). Note the different intensity scales. The gate window of 100 μs with zero gate delay.*

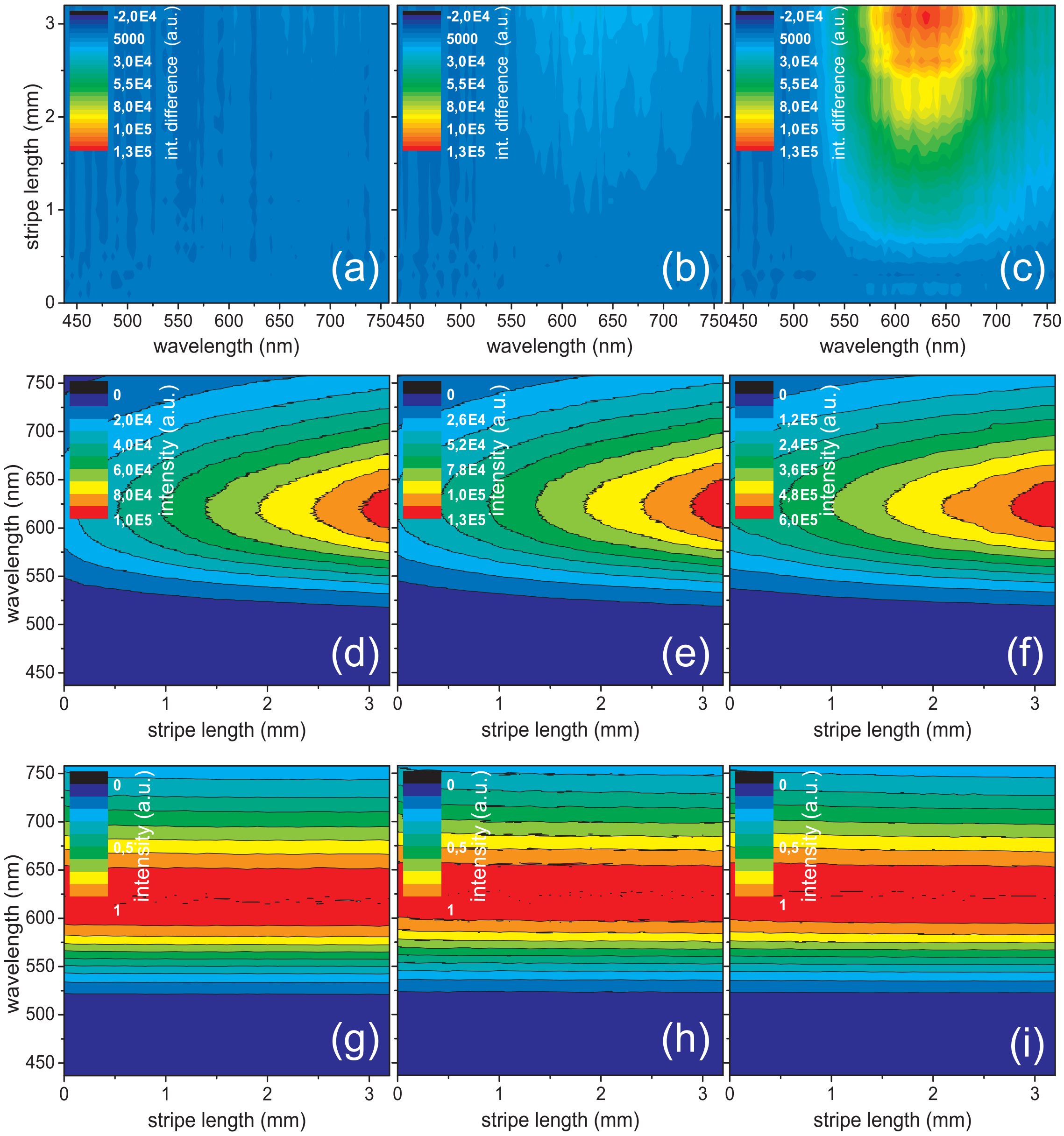

Figure 5.29: *(a-c) Two-dimensional maps of the F and S-band VSL/intSES difference of the "yellow" Si-ncs/SiO$_2$ sample for excitation densities of (a) 0.5 MW/cm^2, (b) 2.4 MW/cm^2 and (c) 12.2 MW/cm^2. The intensity scale is fixed in all graphs to show the StE onset with increasing the excitation density. (d-f) ASE spectra (normalized in (g-i)) for three excitation densities as in (a-c).*

Figs. 5.29(a-c) show two-dimensional maps of the VSL and integrated SES difference of the "yellow" Si-ncs/SiO$_2$ sample for excitation densities of (a) 0.5 MW/cm^2, (b) 2.4 MW/cm^2 and (c) 12.2 MW/cm^2 with a fixed intensity scale in all graphs. ASE spectra for three excitation densities as in (a-c) are plotted in panels (d-f) (normalized in panels (g-i)).

The PL spectrum of this sample is slightly spectrally blue-shifted compared to the ASE spectrum for the excitation density of 6.7 MW/cm^2 and the stripe length of 3.2 mm (Fig. 5.30(a)), similarly to the previously studied gate detection window of 0.2 - 100 μs. On the other hand, the gap between the PL spectrum and the VSL/intSES difference spectrum (taken for the longest achieved stripe and the highest excitation density), reported in the detection window delayed of 200 ns with respect to the laser pulse (Fig. 5.26(b)), vanished here and the VSL/intSES difference spectrum very well correspond with the PL and ASE spectrum (Figs. 5.30(b,c)) of the "yellow" sample. That is probably due to inclusion the F-band and "green" emission band together with the whole S-band emission in this detection window of 0-100 μs.

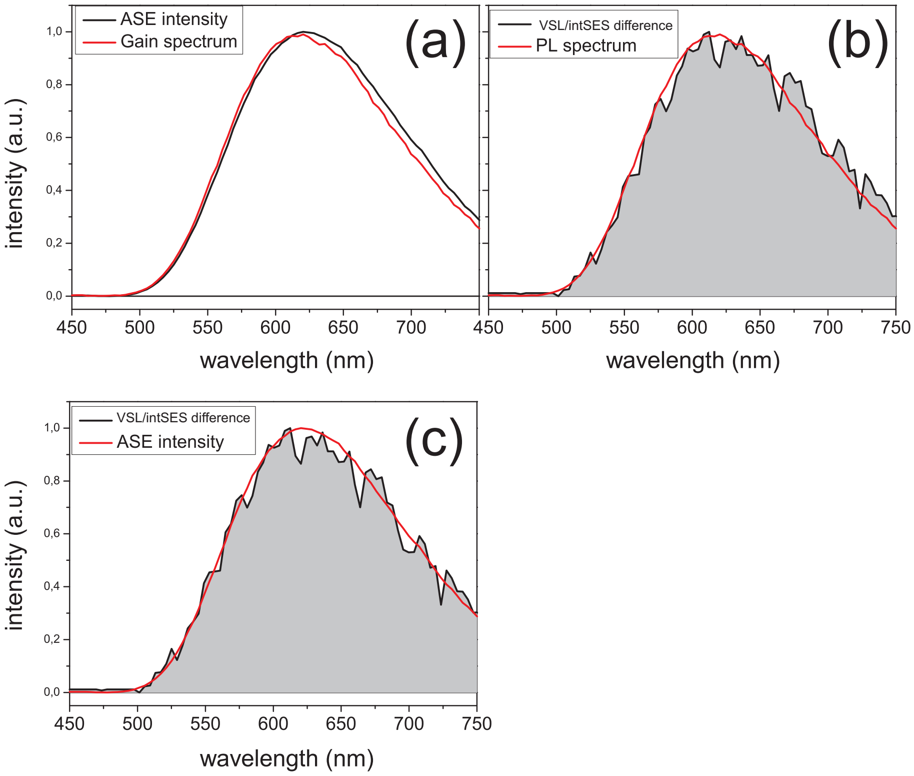

Figure 5.30: *Comparison of (a) the PL and ASE spectrum, (b) the PL and VSL/intSES difference spectrum and (c) the ASE and VSL/intSES difference spectrum in the "yellow" Si-ncs/SiO$_2$ sample. ASE and VSL/intSES difference spectrum was taken for excitation density of 6.7 MW/cm^2 and the stripe length of 3.2 mm.*

Finally, we present the VSL/intSES difference (Fig. 5.31(a)) and gain spectrum (Fig. 5.31) of the "yellow" sample for the excitation density of 6.7 MW/cm^2 and for the longest achieved stripe of length of 3.2 mm. The gain spectrum is evaluated using Eq. 5.9 and is relatively broad. The approximate value of net optical gain at the emission wavelength of 620 nm is ~ 36 cm^{-1} .

Conclusions

In the first part of this chapter, we presented the VSL and SES techniques that we used for optical gain measurements. We mentioned limitations of the VSL method

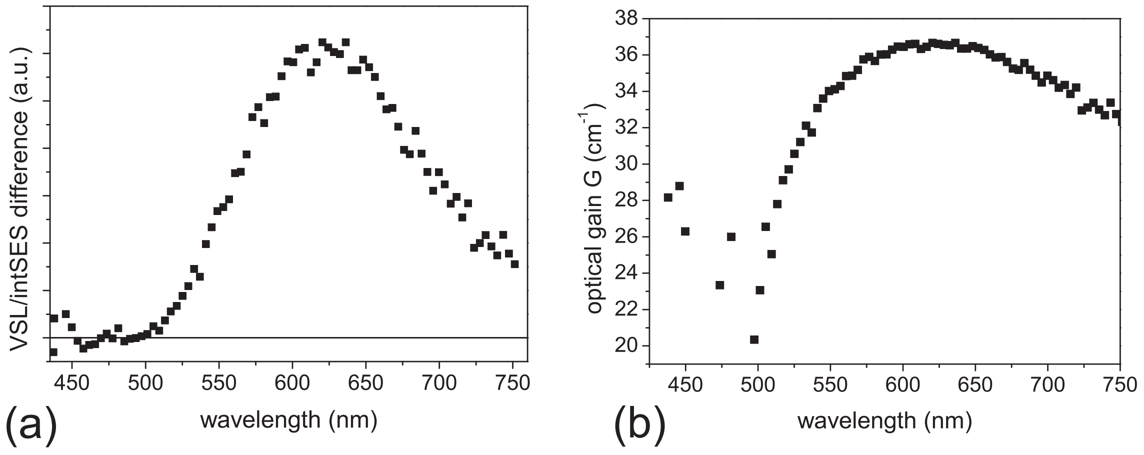

Figure 5.31: *(a) The VSL/intSES difference spectrum and (b) the gain spectrum of the "yellow" Si-ncs/SiO$_2$ sample for the excitation density of 6.7 MW/cm^2 and for the longest achieved stripe of length of 3.2 mm.*

for the low gain materials such as our Si-ncs/SiO$_2$ samples and the necessity of using the complementary SES method to remedy the gain-like artefacts that might occur in the VSL measurements.

In the second part of this chapter, our experimental results obtained by the VSL and SES technique are presented for the "green" emission band, the F and S-band separately. The main characteristics of the measurements that denote the StE onset in the sample, i.e. the positive net optical gain, are the positive VSL/intSES difference, narrowing of the emission spectra with increasing excitation density and stripe length, and superlinear slope of the output-input intensity dependence. All of these properties were reported for the F-band in the both studied Si-ncs/SiO$_2$ samples ("white" and "yellow") when the VSL/intSES difference peaked at ∼ 435 nm. Similarly, the gain measurements on the S-band in the both samples showed the positive VSL/intVSL difference and the output-input intensity superlinear behaviour. Perhaps due to a wide Si-ncs size distribution in our samples, the S-band emission spectra narrowing was negligible. The VSL/intSES difference peaks at ∼ 600 nm in the "white" and at ∼ 620 nm in the "yellow" Si-ncs/SiO$_2$ sample. Moreover, we observed a negative VSL/intSES difference on the "green" emission band, probably due to the induced nonlinear absorption.

We proposed models of the recombination processes and mentioned the mechanism of the StE that might be taking place in our samples.

Chapter 6

CONCLUSIONS

In this work, we studied the possibility of the StE onset in our Si-ncs/SiO_2 samples under UV pulsed laser pumping. Firstly, we prepared these samples on the basis of the preparation method proposed in [26]. This method is relatively simple and low cost and allows us to prepare samples containing small Si-ncs with the mean core size of $\sim 2-3$ nm embedded in the SiO_2-based matrix. The concentration of the Si-ncs seems to be arbitrary but the highest PL emission intensity was obtained for the Si-ncs volume fractions between 10 and 20 vol.%. Samples prepared in this way show relatively high optical quality and spectrally blue-shifted emission, which are very important features for the presence of the positive optical gain.

Secondly, the steady-state PL emission spectra of the ”yellow” and ”blue” Si-ncs/SiO_2 samples revealed two emission bands - F-band and S-band with nanosecond and microsecond decay times, respectively. Further investigation of these two emission components was done by time-resolved measurements in different detection windows. We have reported also a ”green” emission band peaked at $\sim$ 500 nm, which is present in the PL spectra during and immediately after excitation. The origin of the ”green” emission might be in the Si-ncs core-related e-h recombination. The F-band peaks at $\sim$ 435 nm for both types of samples and we propose the origin of the ”blue” emission lies either within the recombinations in some structural defects in the Si-ncs oxide shell [32] and/or within an intrinsic emission from small Si-ncs ($\sim$ 1 nm core diameter)[31][33][34]. The S-band peaks at $\sim$ 600 nm and at $\sim$ 620 nm in the ”white” and ”yellow” Si-ncs/SiO_2 samples, respectively. The difference between the various S-band peaks is probably due to different mean size distribution of the Si-ncs in the samples (”white” contains smaller Si-ncs than ”yellow”). The S-band probably originates in the e-h recombination at the surface/interface related states. Trapping of the carriers into the surface states (located on either Si=O or Si-OH bonds) leads to their spatial separation resulting in suppressed Auger recombination.

Finally, we presented the VSL and complementary SES techniques suitable for the optical gain measurements in low-gain materials. We measured the VSL and intSES difference on the "green", F and S-band contributions, both in the "yellow" and "white" Si-ncs/SiO_2 samples. In the case of the "green" band, we obtained a negative difference for both samples that might be due to the induced transient nonlinear absorption in the excited area [42] which leads to a strong reabsorption of the emitted light inside the sample. On contrary, a positive VSL/intSES difference was obtained in both the F-band and S-band emission components and also for both types of the Si-ncs/SiO_2 samples. The positive difference in conjuction with the ASE spectra narrowing and the output-input intensity superlinear behaviour (both reported in our samples) are a good evidence for the StE onset, i.e. the positive net optical gain, in our samples. A proposed model of recombination processes assumes that the stimulated emission at the F-band might occur in case when the structural defects and/or small Si-cluster (F-band) and the oxygen-related Si-ncs surface states (S-band) share the common ground state. The oxygen-related state act as a storage of electrons, i.e. as a metastable state, which may lead to the inversion of the population followed by the stimulated emission at the F-band. The metastable state has the decay time of the order of μs, therefore it might be responsible for the StE onset at the S-band. Therefore, it seems that the presence of oxygen related states (Si=O and/or Si-OH bonds) is crucial/fundamental for the StE onset on both, the F and S-band emission components.

We have also extracted values of the net optical gain coefficient using Eq. 5.9. We obtained the optical gain of ~ 24 cm^{-1} at 435 nm in the F-band of the "white" Si-ncs/SiO_2 sample and the optical gain of ~ 36 cm^{-1} at 620 nm in the S-band of the "yellow" Si-ncs/SiO_2 sample.

Bibliography

[1] L. C. Kimerling. *Silicon microphotonics.* Appl. Surf. Sci., **159-160**, 8–13 (2000).

[2] D. J. Lockwood, editor. *Light Emission in Silicon - From Physics to Devices*, volume Semiconductors and Semimetals 49. Academic Press USA (1998).

[3] L. T. Canham. *Silicon quantum wire array fabrication by electrochemical and chemical dissolution of wafers.* Appl. Phys. Lett., **57**(10), 1046 (1990).

[4] L. Pavesi, L. Dal Negro, C. Mazzoleni, G. Franzo and F. Priolo. *Optical gain in silicon nanocrystals.* Nature, **408**, 440 (2000).

[5] S. Coffa, G. Franzo and F. Priolo. *High efficiency and fast modulation of Er-doped light emitting Si diodes.* Appl. Phys. Lett., **69**, 2077–2079 (1996).

[6] Pavesi L. and D. J. Lockwood, editors. *Silicon Photonics*, volume Topics in Applied Physics 94. Springer Berlin (2004).

[7] A. I. Anselm. *Úvod do teorie polovodič.* Academia Praha (1967).

[8] I. Pelant and J. Valenta. *Luminiscenční spektroskopie*, volume Objemové krystalické polovodiče. Academia Praha (2006).

[9] S. Ossicini, L. Pavesi and F. Priolo. *Light Emitting Silicon for Microphotonics.* Springer Berlin (2003).

[10] J. Formánek. *Úvod do kvantové teorie I.* Academia Praha (2004).

[11] T.-Y. Kim, N.-M. Park, K.-H. Kim, G. Y. Sunga, Y.-W. Ok, T.-Y. Seong and C.-J. Choi. *Quantum confinement effect of silicon nanocrystals in situ grown in silicon nitride films.* Appl. Phys. Lett., **85**(22), 5355 (2004).

[12] M. V. Wolkin, J. Jorne, P. M. Fauchet, G. Allan and C. Delerue. *Electronic States and Luminescence in Porous Silicon Quantum Dots: The Role of Oxygen.* Phys. Rev. Lett., **82**, 197 (1999).

[13] B. V. Kamenev and A. G. Nassiopoulou. *Self-trapped excitons in silicon nanocrystals with sizes below 1.5 nm in Si/*SiO_2 *multilayers.* J. Appl. Phys., **90**, 5735 (2001).

[14] A. Ourmazd, D. W. Taylor, J. A. Rentschler and J. Bevk. *Si* $\rightarrow$ SiO_2 *transformation: Interfacial structure and mechanism.* Phys. Rev. Lett., **59**, 213–216 (1987).

[15] C. Delerue, G. Allan and M. Lannoo. *Theory of silicon nanocrystals.* In: Towards the first silicon laser; L. Pavesi, S. Gaponenko and L. Dal Negro, editors. NATO Science Series II (2003).

[16] M. H. Nayfeh, N. Rigakis and Z. Yamani. *Photoexcitation of Si-Si surface states in nanocrystallites.* Phys. Rev. B, **56**, 2079 (1997).

[17] H. Chen, J. H. Shin, P. M. Fauchet, J.-Y. Sung, J.-H. Shin and G. Y. Sung. *Ultrafast photoluminescence dynamics of nitride-passivated silicon nanocrystals using the variable stripe length technique.* Appl. Phys. Lett., **91**(173121) (2007).

[18] L. Pavesi and M. Ceschini. *Stretched-exponential decay of the luminescence in porous silicon.* Phys. Rev. B, **48**, 17625 (1993).

[19] V. I. Klimov, A. A. Mikhailovsky, D. W. McBranch, C. A. Leatherdale and M. G. Bawendi. *Quantization of Multiparticle Auger Rates in Semiconductor Quantum Dots.* Science, **287**, 1011 (2000).

[20] C. Delerue, M. Lanoo, G. Allan, E. Martin, I. Mihalcescu, J. C. Vial, R. Romestain, F. Muller and A. Bsiesy. *Auger and Coulomb charging effects in semiconductor nanocrystallites.* Phys. Rev. Lett., **75**, 2228 (1995).

[21] R. M'ghaïeth, H. Maâref, I. Mihalcescu and J. C. Vial. *Auger effect as the origin of the fast-luminescent band of freshly anodized porous silicon.* Phys. Rev. B, **60**, 4450 (1999).

[22] A. A. Seraphin, S.-T. Ngiam and K. D. Kolenbrander. *Surface control of luminescence in silicon nanoparticles.* J. Appl. Phys., **80**(11), 6429 (1996).

[23] L. Dal Negro, M. Cazzanelli, N. Daldosso, Z. Gaburro, L. Pavesi, F. Priolo, D. Pacifci, G. Franzo and F. Iacona. *Stimulated emission in plasma-enhanced chemical vapour deposited silicon nanocrystals.* Physica E, **16**, 297 (2003).

[24] A. J. Dekker. *Fyzika pevných látek.* Academia Praha (1996).

[25] V. Švrček, I. Pelant, J. L. Rehspringer, P. Gilliot, D. Ohlmann, O. Crégut, B. Hönerlage, T. Chvojka, J. Valenta and J. Dian. *Photoluminescence properties of sol-gel derived SiO_2 layers doped with porous silicon.* Mater. Science & Engineering C: Biomimetic and Supramolecular Systems, **19**, 233 (2002).

[26] K. Dohnalová, I.Pelant, K. Kůsová, P. Gilliot, M. Gallart, O. Crégut, J-L. Rehspringer, B. Honerlage, T. Ostatnický and S. Bakardjeva. *Closely packed luminescent silicon nanocrystals in a distributed-feedback laser cavity.* New Journal of Physics, **10**(063014) (2008).

[27] V. Svrček, A. Slaoui, J.-C. Muller, J.-L. Rehspringer, B. Honerlage, R. Tomasiunas and I. Pelant. *Studies of silicon nanocrystals in phosphorus rich SiO_2 matrices.* Physica E, **16**, 420–423 (2003).

[28] M. Fujii, A. Mimura, S. Hayashi, K. Yamamoto, C. Urakawa and Hitoshi Ohta. *Improvement in photoluminescence efficiency of SiO_2 films containing Si nanocrystals by P doping: An electron spin resonance study.* J.Appl.Phys., **87**(4), 1855 (2000).

[29] J. Valenta, A. Fučiková, F. Vácha, F. Adamec, J. Humpolíčková, M. Hof, I. Pelant, K. Kůsová, K. Dohnalová and J. Linnros. *Light-Emission Performance of Silicon Nanocrystals Deduced from Single Quantum Dot Spectroscopy.* Adv. F. Mater., **18**(2666) (2008).

[30] G. Viera, S. Huet and L. Boufendi. *Crystal size and temperature measurements in nanostructured silicon using Raman spectroscopy.* J. Appl. Phys., **90**, 4175 (2001).

[31] J. Valenta et al. *On the origin of the fast photoluminescence band in small silicon nanoparticles.* New J. Physics, **10**, 073022 (2008).

[32] L. Tsybeskov, Ju. V. Vandyshev and P. M. Fauchet. *Blue emission in porous silicon: Oxygen-related photoluminescence.* Phys. Rev. B, **49**, 7821 (1994).

[33] M. H. Nayfeh, N. Barry, J. Therrien, O. Akcakir, E. Gratton and G. Belomoin. *Stimulated blue emission in reconstituted films of ultrasmall silicon nanoparticles.* Appl. Phys. Lett., **78**, 1131 (2001).

[34] V. Švrček, D. Mariotti and M. Kondo. *Ambient-stable blue luminescent silicon nanocrystals prepared by nanosecond-pulsed laser ablation in water.* Optics Express, **17**(2) 520 (2009).

[35] A. Puzder, A. J. Williamson, J. C. Grossman and G. Galli. *Surface Chemistry of Silicon Nanoclusters.* Phys. Rev. Lett., **88**(9) (2002).

[36] M. V. Wolkin, J. Jorne, P. M. Fauchet, G. Allan and C. Delerue. *Electronic States and Luminescence in Porous Silicon Quantum Dots: The Role of Oxygen.* Phys. Rev. Lett, **82**, 197 (1999).

[37] K. L. Shaklee and R. F. Leheny. *Direct determination of optical gain in semiconductor crystals.* Appl. Phys. Lett., **18**(11), 475 (1971).

[38] J. Valenta, K. Luterová, R. Tomasiunas, K. Dohnalová, B. Hönerlage and I. Pelant. *Optical gain measurements with variable stripe length technique.* Towards the first silicon laser, Ed. by L. Pavesi, S. Gaponenko and L. Dal Negro, NATO Science Series II (2003).

[39] J. Valenta, I. Pelant and J. Linnros. *Waveguiding effects in the measurement of optical gain in a layer of Si nanocrystals.* Appl. Phys. Lett., **81**, 1396 (2002).

[40] T. Ostatnický, P. Janda, J. Valenta and I. Pelant. *Optical gain in planar waveguides.* Proc. of SPIE, **6609**(66090F) (2007).

[41] T. Ostatnický, M. Rejman, J. Valenta, K. Herynková and I. Pelant. *Guiding and amplification of light due to silicon nanocrystals embedded in waveguides.* In: Silicon Nanophotonics; L. Khriachtchev, editor, World Scientific, Singapore. pages 267–296 (2009).

[42] S. Vijayalakshmi, H. Grebel, G. Yaglioglu, R. Pino, R. Dorsinville and C. W. White. *Nonlinear optical response of Si nanostructures in a silica matrix.* J. Appl. Phys., **88**(11), 6418 (2000).

[43] F. Trojánek, K. Neudert, P. Malý, K. Dohnalová and I. Pelant. *Ultrafast photoluminescence in silicon nanocrystals measured by femtosecond up-conversion technique.* J. Appl. Phys., **99**, 116108 (2006).

[44] K. Luterová, I. Pelant, I. Mikulskas, R. Tomasiunas, D. Muller, J.-J. Grob, J.-L. Rehspringer and B. Hönerlage. *Stimulated emission in blue-emitting* Si^+*-implanted* SiO_2 *films.* J. Appl. Phys., **91**, 2896 (2002).

[45] I. Mihalcescu, J. C. Vial, A. Bsiesy, F. Muller and R. Romestain. *Saturation and voltage quenching of porous-silicon luminiscence and the importance of the Auger effect.* Phys. Rev. B, **51**(24) (1995).

[46] L. Khriachtchev, M. Rasanen, S. Novikov and J. Sinkkonen. *Optical gain in* Si/SiO_2 *lattice: Experimental evidence with nanosecond pulses.* Appl. Phys. Lett., **79**, 1249 (2001).

[47] P. M. Fauchet, J. Ruan, H. Chen, L. Pavesi, L. Dal Negro, M. Cazzaleni, R. G. Elliman, N. Smith, M. Samoc and B. Luther-Davies. *Optical gain in different silicon nanocrystal systems.* Opt. Mater., **27**, 745 (2005).

[48] K. Luterová, K. Dohnalová, V. Švrček, I. Pelant, J. P. Likforman, O. Crégut, P. Gilliot and B. Hönerlage. *Optical gain in porous silicon grains embedded in sol-gel derived* SiO_2 *matrix under femtosecond excitation.* Appl. Phys. Lett., **84**(17), 3280 (2004).